NTNU – Trondheim
Norwegian University of
Science and Technology

Dynamic Positioning for ROV Operating in Fish Farms

Ron Drozdik

Master of Science in Cybernetics and Robotics
Submission date: February 2015
Supervisor: Jo Arve Alfredsen, ITK
Co-supervisor: Martin Føre, ITK
Per Rundtop, SINTEF

Norwegian University of Science and Technology
Department of Engineering Cybernetics

Abstract

The usages of Remotely Operated Unmanned Underwater Vehicles (ROVs') for inspection of marine structures is today an essential part of the offshore industry. However, in the case of inspection of fish farms, the ROV has to spend continuous time relatively close to the water surface, in exposed seas, while navigating irregular flexible fish nets. The ability for an ROV to effectively navigate within the fish farm cage and guarantee a complete inspection requires new tools, and dynamic positioning (DP) improvements. This thesis will use the simulation tool FHSim to investigate two aspects regarding these issues. First, it will examine, by simulations, the performance of different variations of a nonlinear observer and an extended kalman filter (EKF) with or without a cascaded current observer, in the ROV's operating conditions. Secondly a visualization tool is integrated with the ROV DP system that allows it to traverse the fish net autonomously while also visualizing its position in the cage. The visualization module also identifies net areas that have been inspected by the ROV. All the modified DP modules are assessed in several simulation cases designed to mimic ROV inspection behaviour. It was found that in particular, the nonlinear observer performed better in estimation and wave filtering abilities, while the EKF was superior in dead reckoning. These differences were attributed to the different nature of the two observers, their programmed integration method, and possibly insufficient tuning of the EKF. The autonomous net traversal algorithm was successfully able to make the ROV traverse the cage, however, some trajectory faults were identified. Improvements to overcome these faults were suggested.

Sammendrag

Bruken av fjernopererte ubemannede undervannsfartøy (ROV) til inspeksjon av marine strukturer er i dag en essensiell del av offshore-industrien. Ved inspeksjon av fiskemerder må ROVen tilbringe betydelig tid tett ved havoverflaten der den er spesielt eksponert for havstrømninger og bølger, samtidig som den må kunne navigere langs det irregulære og fleksible fiskenettet. Evnen til en ROV til å kunne navigere effektivt innen fiskemerder og garantere en fullstendig inspeksjon, krever nye redskaper og forbedringer av dens dynamiske posisjonerings (DP) -system. Dette prosjektet vil benytte seg av simuleringsredskapet FHSim for å undersøke to aspekter vedrørende disse utfordringene. Innledningsvis vil ytelsen av ulike variasjoner av en ulineær observer og et extended kalman filter (EKF), med eller uten en "cascaded current observer", undersøkes ved bruk av simulering under ROVens operasjonsforhold. Videre integreres et visualiseringsverktøy med ROVens DP-system som tillater den å traversere fiskemerden autonomt mens den visualiserer sin posisjon. Visualiseringsmodulen identifiserer også områdene av nettet som ROVen har inspisert. Alle modifiserte DP-moduler er vurdert i flere simuleringssituasjoner designet for å etterligne ROVens inspeksjonsmønster. Resultatene viste at den ulineære observeren presterte bedre innen estimering og bølgefiltrering enn EKF, mens EKF presterte bedre i "dead reckoning". Disse ulikhetene skyldes trolig observernes ulike oppbygging, deres programmerte integrasjonsmetoder, og muligens utilstrekkelig finjustering av EKF. Bruk av den autonome nettraverserings-algoritmen tillot ROVen å traversere nettet, skjønt noen problemer med bevegelses-mønsteret ble identifisert. Forbedringer for å overvinne disse problemene ble foreslått.

Acknowledgements

This thesis is the result of my master degree taken from August 2009 through February 2015. The work took place at the Department of Engineering Cybernetics at the Norwegian University of Science and Technology, in collaboration with Sintef Fisheries and Aquaculture.

I wish to thank my main supervisor Jo Arve Alfredsen for giving me the opportunity and support I needed to start the thesis. I especially wish to thank both my co-supervisors Per Rundtop and Martin Føre for their openness, kindness and surprisingly fast responses to questions I have had. Both have provided most of the guidance, feedback and help I needed to successfully accomplish this work. Lastly, but not least, my main support and affection, given at any time during this period is attributed to my love Ragnhild.

Ron Drozdik *Trondheim ,February 1, 2015*

NTNU

Norwegian University of Science and Technology

Faculty of Information Technology, Mathematics and Electrical Engineering

Department of Engineering Cybernetics

MASTER THESIS

Name:	Ron Drozdik
Program:	Engineering Cybernetics
Thesis title:	Dynamic positioning for ROV operating in fish farms

Project description

Within the offshore industry the ROV has replaced divers in many underwater operations. ROV services are also finding increased use in the fish farming industry where they carry out tasks like net cleaning and inspection of sea cages and moorings. Considering the relatively fragile nature of the cage netting and supporting structures the aquaculture ROV needs to operate reliably and should be able to traverse the cage with high accuracy in attitude, position and velocity. Development of a DP system particularly adapted to the requirements imposed by operating an ROV in the fish farming environment is therefore desirable. The ROV will typically be working close to the surface at highly variable sea states and making a DP system that is capable of handling the wave induced motion in a proper manner represents a significant challenge. Finding solutions to this problem will be the main focus of this Master project, which includes the following subtasks:

- Review relevant literature of observer design
- Configuration and introduction to the simulating environment FhSim. Review of existing code.
- Review of the ROV's wave characteristics by simulations. Develop requirements specifications for the wave filter.
- Explore and choose up to two observer designs for implementation
- Implementation, testing, analysis and documentation of observer performance by simulation using a relevant set of scenarios
- Develop and adapt a DP system to ROV operating conditions. Implement functions such as auto-heading (against cage net), speed and direction control. Consider different strategies for thruster wear reduction.
- Test entire system by simulation and demonstrate performance improvements
- Conclusion and writing up report

Project start:	2014-09-08
Project end:	2015-02-01
Host institution:	Department of Engineering Cybernetics, NTNU
Supervisor:	Jo Arve Alfredsen, NTNU DEC
Co-supervisors:	Per Rundtop, SINTEF FH; Martin Føre, SINTEF FH/NTNU DEC

Jo Arve Alfredsen

Trondheim, 2014-01-10

Contents

List of Figures

List of Tables

Nomenclature

AUV	Autonomous Underwater Behicle
DP	Dynamic Position
EKF	Extended Kalman Filter
FFT	Fast Fourier Transform
LW	Low Frequency
NPO	Nonlinear Passive Observer
ROV	Remotely Operated Vehicle
WF	Wave Frequency

1 Introduction

This thesis is about the design of a DP system for a Remotely Operated Unmanned Underwater Vehicle (ROV), to be deployed for inspection of aquaculture sites, more specifically a fish farm for the Atlantic salmon. The foundations of the DP system is already implemented, and this thesis will be a continuation of that work. New additions to the DP system will be added, and tested. The solution will be simulated using FHSim from Sintef Fisheries and Aquaculture. FHSim is a simulation and visualization software used to model the behaviour of marine vessels or structures in the ocean, see (Reite et al., 2014).

1.1 Motivation

Fish farming of the Atlantic salmon is commonly done at sheltered sites but have during the last decade moved more towards exposed locations (pers. comm., Per Rundtop). The farm itself consists of floating cages that are kept at a fixed location in the ocean by mooring lines. The salmon is kept inside the cage which can either be free floating, fixed, square or rounded. A particular common design is the usage of a rounded cage with a flexible thread netting. The benefits of a flexible net is that harvesting the fish can be done by pulling the net up and gathering the fish more densely. A flexible net is also more resilient to strain from the environment, such as strong currents and waves. However, a common weakness of flexible nets is their ability to tear up. Approximately two-thirds of reported escape incidents and number of fish escape are due to holes in the net (Jensen et al., 2010; Jackson et al., 2015). Such holes are caused by biting from predators or fish, abraison, 'collision' with boats, and inappropriate cage handling procedures (Jensen et al., 2010; Jackson et al., 2015). Not only does escape generate economical losses for the farmers, it also contaminates the environment by breeding between farmed and wild fish populations, and the spreading of disease.

In order to limit the number of fish escape incidents, the submerged netting has to be continuously inspected. Currently fish cage net maintenance is commonly done using divers or submersible ROV's (pers. comm., Per Rundtop). Common tasks of divers are dead fish removal, report on fish and cage conditions, and assisting with moving of cages (Frost et al., 1996). However, the usefulness of divers as stock monitors is limited due to their avalability (Frost et al., 1996). The usages of ROV's for fish farm inspection has early been signified by (Balchen, 1991; Frost et al., 1996), and can provide cost benefits over the use of a diver.

The main challenges in the usage of an ROV, as perceived in this thesis, is the difficulty in orienting and manoeuvring it such that one is certain the entire net cage is inspected. This is particularly true for highly irregular nets deformed due to ocean currents (Lader et al., 2008). The ROV is also limited in the type of tasks it can perform. An ROV has more difficulties in the removal of unwanted debris, or performing a net repair.

Fish farms are placed at exposed sea locations to increase the flux of oxygen. This is often included with a high ocean current speed. It is vital for fish farms to be suited in areas exposed to currents so that the fishes' living conditions remain clean and rich in oxygen (Johansson et al., 2007; Edwards and Edelsten, 1976; Wildish et al., 1993). High currents will generate an extra demand for the thrusters of the ROV operating in said conditions. According to (pers. comm., Per Rundtop), the ROV technology has not been adapted for typical aquaculture sites.

The typical ROV operates in deeply submerged conditions of hundreds' to thousands of meters. Wave forces are not commonly present in areas in which an ROV operates, and hence there is a lack of studies about how an ROV would be affected by such forces. The net cage being inspected might also be highly irregular due to deformation from ocean forces (Lader et al., 2008). This

can make it difficult to map areas that have been inspected, and areas left unchecked when using an ROV. Net segments that are not inspected might contain holes, or beginning holes from where farmed fish can escape. More studies and technological advances are needed in this field to optimize the ROV performance in the wave zone and in proximity to flexible net structures.

1.2 Problem Statement

This thesis will continue the work already begun from a previous thesis (Hval, 2012). In Hval (2012), the simulation environment and basic DP systems were developed in FHSim. Further developments have also been added later from Sintef.

A key missing DP functionality, necessary for the ROV to inspect the net close to the surface, includes a wave filter in the observer. There is a lack of documentation in Hval (2012) that assessed the ROV performance under different ocean conditions. Observer characteristics such as dead reckoning, model errors, and wave filtering capabilities are not assessed either.

This thesis will cover three different areas in which the ROV dynamic positioning (DP) system can be improved for net cage inspection:

1. Assess the DP system previously implemented in FHSim.

2. Modify the previously implemented observer by giving it a wave filter, and velocity measurements. Also add a current observer, a discrete extended kalman filter observer. The new DP features will be examined by a number of different simulation tests that are based on the environmental conditions which the ROV is expected to operate in.

3. Add a new simple waypoint algorithm for autonomous net traversal using the visualization component of FHSim to the DP system. Examine the results of the net traversal algorithm.

1.3 Research Method

All modifications done to the DP system in the ROV are programmed, and simulated in FHSim. Different simulation cases will be designed based on the expected ROV operation conditions, and are analysed either qualitatively or quantitatively using data from the simulations.

1.4 Contributions

This thesis will contribute with an assessment of the effects of adding an independent current observer together with a nonlinear luenberger observer, and a discrete extended kalman filter for an ROV. The thesis will also provide a demonstration of the possibility of using FHSim as a visualization tool to improve net inspection using an ROV. Other contributions include added modules and debugging of the FHSim module for the ROV DP system.

1.5 Thesis Structure

Introduction Presents the thesis motivation, research method and problem statement.

Background Theory The section describes necessary background information about ROV modelling, ocean wave modelling, and the simulation environment FHSim.

Materials and Methods This section presents the added discrete extended kalman filter, the nonlinear luenberg observer, and the current estimator for the DP system. The section also details about the implemented autonomous traversal algorithm, and the visualization component in FHSim, and other DP components which have not been modified in the thesis but are a major part of the DP system. The test cases for the ROV are also presented

Results All the results of the tested DP systems are presented and reviewed. Ocean data from Rataran are also presented. The test results of the autonomously travelling ROV are also shown.

Discussions and Conclusion The results are discussed and a conclusion is provided.

2 Background Theory

This section will provide an overview of relevant technical knowledge which form the basis of the designed DP system.

2.1 Basics of the Modern Dynamic Positioning

Dynamic positioning, in its essence, is the ability for an ocean vessel to maintain a fixed position and heading in space, or to perform low speed manoeuvring tasks based on commands from an operator (Fossen, 2011). More modern and innovative DP functionalities include complex manoeuvring tasks, such as autopilot, multiple vessel formations, and waypoint tracking (Fossen, 2011).

The earliest DP systems were only composed of PID controllers and measurement filters (Sargent and Cowgill, 1976; A.J. et al., 1996). However, modern DP systems have a host of other sub-systems that greatly improve the controlling performance.

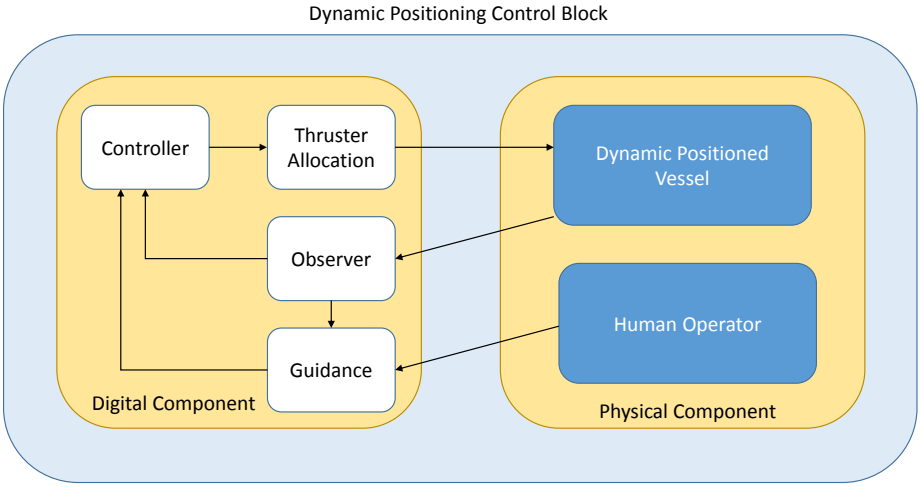

Figure 1: A simple overview of the main control-system components in a modern DP system

The Dynamic Positioning block has at least four main components in it: The controller block, guidance block, observer block and thruster allocation.

2.1.1 Controller

The goal of the controller is to specify the required thrust in the relevant dimensions for the vessel. The desired thrust is a function of the desired position, and possibly desired velocity given from the guidance block.

Most feedback controllers used in DP are extensions or variations of a PID controller, and later also Linear Quadratic Gaussian (LQG) control (Strand, 1999; Sørensen, 2013), however there has been a continual research since the 1990's on the usages of other nonlinear controllers such as fuzzy, backstepping and nonlinear feedback linearization controllers (Sørensen, 2013; Strand, 1999). Nonlinear controllers (as opposed to the linear PID and LQG), use information about the physical model of the vessel to control it.

2.1.2 Thruster Allocation

The purpose of the thrust allocation system is to distribute among the thrusters the desired forces and moments computed by the controller (Ruth, 2008). The thruster allocation block is in its most simple form a routing algorithm that transforms the desired thrust from the north, east, down direction, to the corresponding thrusters of the vessel. For example if the vessel wants to move north, then the thrusters that push the ship northward are applied. The simplest thrust allocation block is a transformation matrix. This greatly simplifies the complexity of the thruster routing to some fairly straightforward numerical calculations. However more complicated methods exist where the routing is determined by an optimization algorithm (Fossen and Johansen, 2006; Ruth, 2008).

2.1.3 Observer

The observer is responsible for the measurement data. Today there exist a large array of sensors to detect relevant navigational data. The more and better measurements that are installed on a vessel the higher control precision can be achieved, for obvious reasons. However, an observer has the ability to greatly improve the measured signals quality, even in the case of signal flaws or disconnections. This makes an observer relatively attractive as it can replace the high cost of a very precise sensor.

The most important features of observers are their ability to filter the measured signals, *and* estimate non-measured values. See figure 2 for a filtered signal. The ability to estimate non-measured values is what made the kalman filter observer in (J.G et al., 1976) such a breakthrough in the early days of DP. For example, a very common usages of observers are the estimation of vessel velocities. That is, the vessel is only equipped with position sensors, and lets the observer use position estimates and a physical model of the vessel to estimate what the velocity is. Observers are also expanded to include estimation of non-vessel variables. The first kalman observer was in (J.G et al., 1976) designed to predict wave, wind *and* current velocities, however, today it is common to only predict wave motions and current forces. More recently, the usage of estimating current velocity instead of current force has been tested, for example (Refsnes, 2007; Aguiar and A.M., 2002).

A third and very attractive feature for some observers, are their ability to predict a signal if there are no measurements available at all. Such predictions are often just valid for short intervals however, but are valuable in case of signal knockouts.

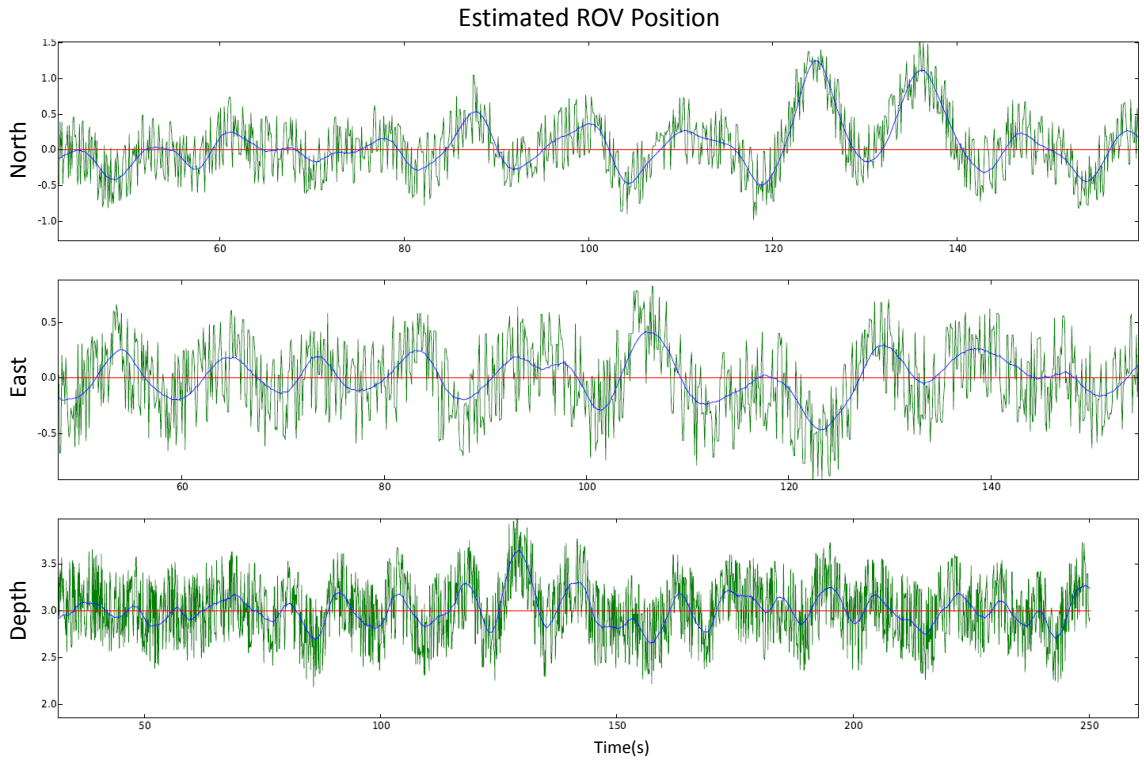

Figure 2: Demonstration of a measured signal before and after passing the observer. Blue signal is from the observer and has filtered away noise, green is the measured value and contains measurement noise.

The prediction of wave motions are used in wave-filtering DP systems. In such control systems, the position of the vessel is separated in two components. One is the motion caused by all forces excluding waves (LF model), and the other is motions caused by waves (WF model). The sum of the two components give the entire motion of the vessel. However for optimal control, only the LF model needs to be controlled. It is in fact very important to filter away oscillatory motions (as presented in the WF model). Such motions cannot usually be compensated by the vessels' thrusters, and it will often waste fuel unnecessarily. It will also increase wear and tear on the thrusters (Sørensen, 2013; Saelid et al., 1983; Tannuri et al., 2003). It is more importantly that thrusters focus on motion that changes the average position of the vessel, which are more predominant in the LF model, although for extreme weather conditions, Sørensen et al. (2002), notes that the wave filter should be turned off. Wave filtering is one of the most important issues to take into account when designing ship control systems (Fossen, 2011).

Figure 3 below shows the effects of a wavefilter in an observer. The noise is filtered away, but so is also the sinusoidal oscillations occurring at about every 10 seconds (see East data). The oscillations are repetitive and don't cause an average change in the vessel position, hence they should be filtered and ignored by the control system.

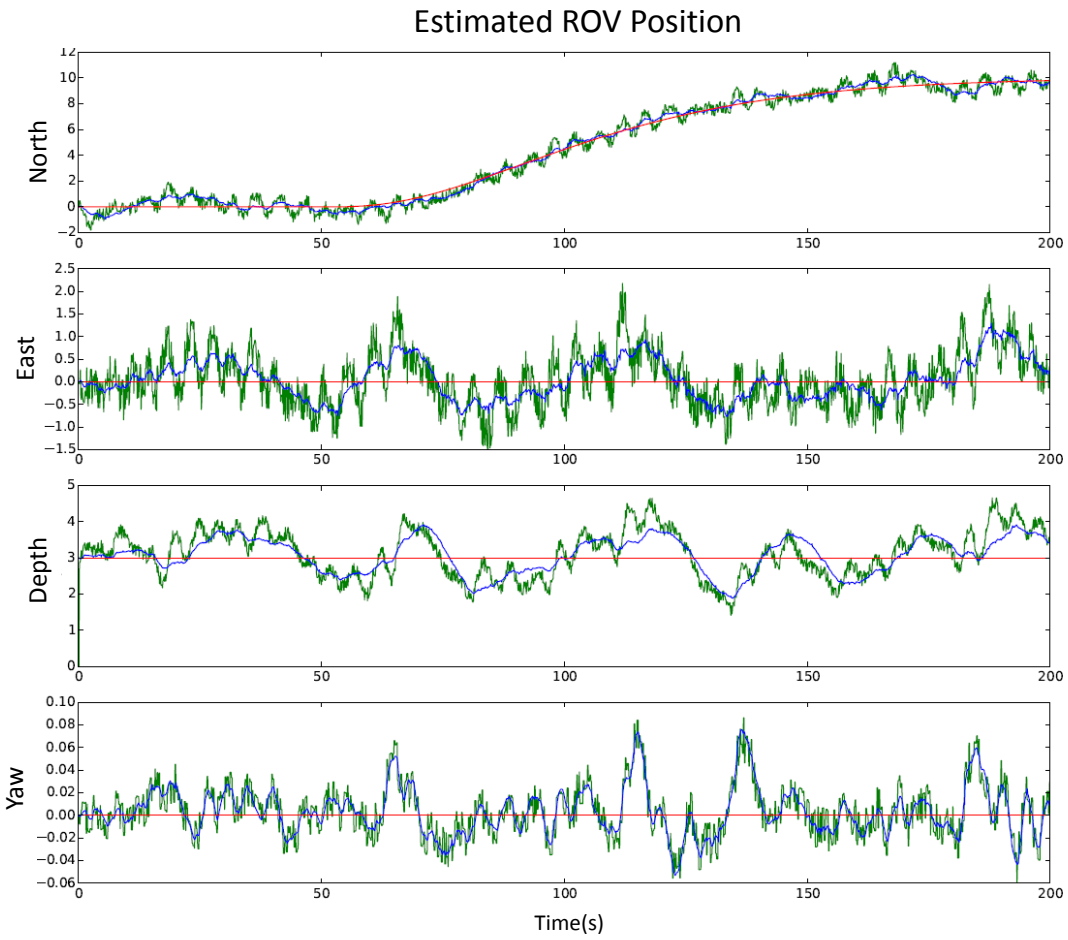

Figure 3: Demonstration of an observer with wave filtering. Blue signal is from observer, green is the measured value. Yaw has no wave filtering applied to it.

2.1.4 Signal Processing

To satisfy safety requirements on DP operated vessels it is common to have redundant measurements in case one of them fails. This is not listed in figure 1, but is an important component for large vessels to satisfy DP safety requirements. The signal processor is responsible of treating the redundant measurements and deciding which one of them represents the most true value. There are several methods of doing this, either by voting techniques, weighing signals, or averaging. For example imagine three sensors are measuring the heading of the ship. If two of the signals are equal to 90 degrees and one signal is 130 degrees. The signal processor, by voting, should decide that the heading of the vessel is equal to 90 degrees since most sensors suggest this value. The signal processor should also disregard unrealistic measurements, such as a vessel having a negative depth (it is hovering in the air) or other faults such as signal spikes. Certain measurement faults can be used to diagnose a probable cause of the error (Filaretov et al., 2012; Falkenberg et al., 2014).

2.1.5 Guidance

The guidance system is the closest control interface of the DP system to the human operator. The human operator chooses a desired position or heading for the vessel, and the guidance will give this position to the controller using a reference model. The reference model is a simple second order model of the ship response to a change in position or heading. It smooths out the

wanted change in position to occur over a time interval, see section 3.5 page 26.

Additional features to the guidance module includes setting restrictions on the vessel speed and acceleration. For more complicated operations such as waypoint movement, trajectory or surface tracking, or formation movement, the guidance algorithm is responsible to generate smooth trajectories for the vessel to follow. The guidance would also be responsible for collision avoidance for the more autonomous crafts.

2.2 Dynamic Positioning for the Unmanned Underwater Vehicles

The earliest practical applications of ROVs' can be dated back to 1958 in which the US Navy used an ROV for controlled underwater recovery and search operations (G.N. and R., 2012). Not until the offshore oil industry bloom, however, was the commercial potential of the ROV recognized (G.N. and R., 2012). The usage of ROVs' could potentially provide a safer and cheaper alternative than divers. Also as the oil industry increasingly operated at extensive depths the usages of ROVs' became a must. ROV technology, however, has not completely replaced the use of divers. The tasks which an ROV can perform underwater is heavily limited compared to what a human diver can do. The technology is continually improving, and the applications of ROVs' are expanding.

Most underwater unmanned vehicles are operated remotely, hence the term ROV (remotely operated vehicle). The DP system is configured to allow, for example, auto heading or auto depth, allowing for easier control for the operator. In (Dukan, 2014), the DP system of an ROV is given an auto surface tracking option, which allows the operator to focus the movement in only two dimensions when close to the ocean floor. More advanced DP systems are tailored for underwater vehicles to operate autonomously, also abbreviated (AUV). In this field a lot of progress has been achieved the last decades (Refsnes, 2007).

2.3 Modelling of Underwater Vehicles

This section will outline the general ideas and mathematical formulations of an underwater vehicle. The formulations are based on (Fossen, 2011), unless stated otherwise. Comparisons will be made to the implemented ROV model in FHSim. There are generally speaking no differences between the modelling of a floating vessel and a submerged vehicle. The same equations apply. However different modelling simplifications are applied on a submerged vessel than a floating vessel, in order to accommodate their typical operating environments.

2.3.1 Control Plant, and Process Plant Models

Marine craft modelling is done under two different circumstances, as is with most modelling concepts. That is, model the system physically as correct as possible using the best mathematical tools available, or simpler; model the system to include its main characteristics in such a way that more complex phenomena can be superimposed linearly if needed.

A comprehensive realistic model is usually distinguished as the Process Plant Model (PPM). The PPM simulates the system, and its interaction with the environment as it would occur in reality (Sørensen, 2013). This is often run in a simulator program using a computer, for example flight simulators used to train air pilots. For realtime simulations a PPM model should be able to perform an entire system simulation quick enough to allow human interaction with it. For a PPM to simulate test scenarios of a system that is pre-programmed (no human interaction), it can run in the timespan of seconds to hours to days. The simplified counterpart of the PPM is called the Control Plant Model (CPM). This is often run within the system that controls the craft. For example the controller of an aircraft or the DP system on a ship. The CPM contains the most important physical properties of the system it controls and should be quick enough (0.1-5 seconds) that it can respond to changes in its input such to satisfy system stability (Sørensen, 2013).

The ROV simulation model in FHSim is a combination of a PPM/CPM model. Some modelling details are very rigorous, while others have been simplified. The DP system is a CPM model.

2.3.2 Geographic Reference Frames

The movement and position of vessels, and any other point in space for that matter, has to be defined in relation to a frame of reference. This is purely for being able to mathematically describe the motion of the point in space. The space might be curved, flat, 2D or 3D.

The geographic reference frames are local frames representing a flat earth. These two frames are relevant for vessels operating in motion ranges that are practically unaffected by the curvature of earth. The **NED** frame, describes the vessel position in terms of the true north, x_n, true east, y_n and down, z_n. It is defined as the tangent plane on the surface of the Earth (Fossen, 2011). A positive down value, indicates a submerged position. The **BODY** frame is purely based on the heading and position of the vessel. Its origin is suitably defined as the centre of the vessel, and its x_b-axis points in the same direction as the ship's heading. Hence as the vessel moves and changes heading, so will the BODY frame copy. The y_b-axis points to the starboard, and the z_b-axis points downward. The BODY frame is used when describing the vessels forward, sideways, and vertical velocity (also called surge , sway and heave respectively). The NED frame is used to describe the vessel's position and heading.

A summary of the notation used for the NED and BODY frame is given in table 1.

Table 1: The notation of (SNAME, 1950) for marine crafts, from (Fossen, 2011)

DOF		Linear and angular velocities	Position and Euler angles
1	motions in the x direction(surge)	u	x
2	motions in the y direction(sway)	v	y
3	motions in the z direction(heave)	w	z
4	rotation about the x axis direction(roll)	p	ϕ
5	rotation about the y axis direction(pitch)	q	θ
6	rotation about the z axis direction(yaw)	r	ψ

2.3.3 Reference Transformations and Kinematics

The mathematical transformation from BODY to NED frame is done by the rotation matrix $\boldsymbol{R}_b^n$. To transform a point from the NED to the BODY frame the matrix is transposed/inverted $(\boldsymbol{R}_b^n)^T = (\boldsymbol{R}_b^n)^{-1} = \boldsymbol{R}_n^b$.

$$\boldsymbol{R}_b^n = \begin{pmatrix} c\psi c\theta & -s\psi c\phi + c\psi s\theta s\phi & s\psi s\phi + c\psi c\phi s\theta \\ s\psi c\theta & c\psi c\phi + s\psi s\theta s\phi & -c\psi s\phi + s\psi c\phi s\theta \\ -s\theta & c\theta c\phi & c\theta c\phi \end{pmatrix}, (c\lambda = cos(\lambda), s\lambda = sin(\lambda)) \tag{1}$$

Throughout this paper the rotation matrix from BODY to NED will be written in two forms: $\boldsymbol{R}_b^n \Leftrightarrow \boldsymbol{R}(\boldsymbol{\Theta})$.

The rotation matrix is limited to use in the three spacial dimensions x,y and z. However an expansion of the matrix allows for a transformation between all 6 dimensional free degrees of motion. This transformation matrix will be written as $\boldsymbol{J}(\boldsymbol{\Theta})$ and:

$$\boldsymbol{J}(\boldsymbol{\Theta}) = \begin{bmatrix} \boldsymbol{R}(\boldsymbol{\Theta}) & \boldsymbol{0}_{3x3} \\ \boldsymbol{0}_{3x3} & \boldsymbol{T}(\boldsymbol{\Theta}) \end{bmatrix} \tag{2}$$

where $\boldsymbol{T}(\boldsymbol{\Theta})$ is the transformation from BODY to NED of the the angular values $\boldsymbol{\Theta} = [\phi, \theta, \psi]^T \in \mathbb{S}^3$, where $\mathbb{S}^3$ denotes a sphere defined by three angles on the interval [0,2π].

$$\boldsymbol{T}(\boldsymbol{\Theta}) = \begin{bmatrix} 1 & s\phi t\theta & c\phi t\theta \\ 0 & c\phi & -s\phi \\ 0 & s\phi/c\theta & c\phi/c\theta \end{bmatrix}, \theta \neq \pm\frac{\pi}{2} \tag{3}$$

The 6 dimensional transformation matrix from BODY to NED is then written:

$$\boldsymbol{J}(\psi) = \begin{bmatrix} \boldsymbol{R}(\psi) & \boldsymbol{0}_{3x3} \\ \boldsymbol{0}_{3x3} & \boldsymbol{I}_{3x3} \end{bmatrix} \tag{4}$$

The position and velocity of the ROV in its 6 dimensions degree of freedom will have the following notation:

$$\boldsymbol{\eta} = \begin{bmatrix} x & y & z & \phi & \theta & \psi \end{bmatrix}^T \in \mathbb{R}^6 \tag{5}$$

$$\boldsymbol{\nu} = \begin{bmatrix} u & v & w & p & q & r \end{bmatrix}^T \in \mathbb{R}^6 \tag{6}$$

Such that $\dot{\boldsymbol{\eta}} = \boldsymbol{J}(\boldsymbol{\Theta})\boldsymbol{\nu}$.

2.3.4 Rigid-Body Forces and Moments

The equations describing the rigid-body forces of the underwater vehicle are expressed as such:

$$\boldsymbol{M}_{RB}\dot{\boldsymbol{\nu}} + \boldsymbol{C}_{RB}(\boldsymbol{\nu})\boldsymbol{\nu} = \boldsymbol{\tau}_{RB} \tag{7}$$

were $\boldsymbol{\tau}_{RB} \in \mathbb{R}^6$ is a generalized vector of external forces and moments impacting the underwater vehicle.

$\boldsymbol{M}_{RB}$ is the rigid-body system inertia matrix, and describes the mass distribution of the underwater vehicle. It has the unique properties of being symmetric and constant: $\boldsymbol{M}_{RB} = \boldsymbol{M}_{RB}^T > 0, \quad \dot{\boldsymbol{M}}_{RB} = \boldsymbol{0}_{6x6}$.

$$\boldsymbol{M}_{RB} = \begin{bmatrix} \boldsymbol{M}_{11} & \boldsymbol{M}_{12} \\ \boldsymbol{M}_{21} & \boldsymbol{M}_{22} \end{bmatrix} \tag{8}$$

$\boldsymbol{C}_{RB}(\boldsymbol{\nu})$ is the coriolis-centripetal matrix and has a large number of different representations. As remarked by (Fossen, 2011) different representations suit different formulations of the vehicle dynamics. The parametrization used in FHSim is:

$$\boldsymbol{C}_{RB}(\boldsymbol{\nu}) = \begin{bmatrix} \boldsymbol{0}_{3x3} & -\boldsymbol{S}(\boldsymbol{M}_{11}\boldsymbol{\nu}_1 + \boldsymbol{M}_{12}\boldsymbol{\nu}_2) \\ -\boldsymbol{S}(\boldsymbol{M}_{11}\boldsymbol{\nu}_1 + \boldsymbol{M}_{12}\boldsymbol{\nu}_2) & -\boldsymbol{S}(\boldsymbol{M}_{21}\boldsymbol{\nu}_1 + \boldsymbol{M}_{22}\boldsymbol{\nu}_2) \end{bmatrix} \tag{9}$$

were $\boldsymbol{\nu}_1 = [u, v, w]^T$ and $\boldsymbol{\nu}_2 = [p, q, r]^T$. And $\boldsymbol{S}(\boldsymbol{\delta})$ is defined accordingly:

$$\boldsymbol{S}(\boldsymbol{\delta}) := \begin{bmatrix} 0 & -\delta_3 & -\delta_2 \\ \delta_3 & 0 & -\delta_1 \\ -\delta_2 & \delta_1 & 0 \end{bmatrix} \tag{10}$$

were $\boldsymbol{\delta} = [\delta_1, \delta_2, \delta_3]^T$.

2.3.5 Hydrostatic Forces

Hydrostatic forces, $\boldsymbol{\tau}_{hyd}$, comprises all forces caused by gravity and buoyancy on the vehicle.

$\boldsymbol{\tau}_{hydstatic} = \mathbf{g}(\boldsymbol{\eta}) + \mathbf{g_0}$

The hydrostatic forces used in FHSim are the general equations of hydrostatic forces on underwater vehicles:

$$\mathbf{g}(\boldsymbol{\eta}) = \begin{bmatrix} & (W-B)sin(\theta) & & \\ - & (W-B)cos(\theta)sin(\phi) & & \\ - & (W-B)cos(\theta)cos(\phi) & & \\ - & (y_gW - y_bB)cos(\theta)cos(\phi) & + & (z_gW - z_bB)cos(\theta)sin(\phi) \\ & (z_gW - z_bB)sin(\theta) & + & (x_gW - x_bB)cos(\theta)cos(\phi) \\ - & (x_gW - x_bB)cos(\theta)sin(\phi) & - & (y_gW - y_bB)sin(\theta) \end{bmatrix} \tag{11}$$

For the control system in which one assume roll and pitch are self stabilizing; $\theta, \phi \approx 0$ the hydrostatic force is simplified to:

$$\mathbf{g}(\boldsymbol{\eta}) = \mathbf{g} = \begin{bmatrix} 0 \\ 0 \\ -(W-B) \\ -(y_g W - y_b B) \\ (x_g W - x_b B) \\ 0 \end{bmatrix} \tag{12}$$

Other considerations of hydrostatic forces include the umbilical of the ROV to the ship it is operating from. The umbilical forces were in this thesis and (Hval, 2012) excluded from the simulation model only because the operating depth of the ROV is limited to the depth of a fish cage. Forces from the umbilical to the ROV are assumed be minute at such depths compared to other forces.

2.3.6 Hydrodynamic Forces and Moments

The hydrodynamic forces of the ROV include all forces generated by the ocean on the ROV. These forces thus include wave, and current forces. This section will be limited to ideas used later for the model in FHSim for the underwater vehicle.

$\boldsymbol{\tau}_{hyddynamic} = \boldsymbol{M}_A \dot{\boldsymbol{\nu}}_r + \boldsymbol{C}_A(\boldsymbol{\nu}_r)\boldsymbol{\nu}_r + \boldsymbol{D}(\boldsymbol{\nu}_r)\boldsymbol{\nu}_r$

$\boldsymbol{\nu}_r$ is the relative velocity of the underwater vehicle compared to the current. If $\boldsymbol{\nu}_c = [v_c, u_c, w_c]^T$ is the ocean currents, then $\boldsymbol{\nu}_r$ is defined as:

$$\boldsymbol{\nu}_r = \begin{bmatrix} u - u_c & v - v_c & w - w_c & p & q & r \end{bmatrix}^T \tag{13}$$

For the case in which the vehicle moves in straight line paths, the acceleration of the current is negligible such that $\dot{\boldsymbol{\nu}}_c \approx 0$ and then the forces are written as such:

$\boldsymbol{\tau}_{hyddynamic} = \boldsymbol{M}_A \dot{\boldsymbol{\nu}} + \boldsymbol{C}_A(\boldsymbol{\nu}_r)\boldsymbol{\nu}_r + \boldsymbol{D}(\boldsymbol{\nu}_r)\boldsymbol{\nu}_r$

The computation of hydrodynamic forces are most commonly done by computer programs (Fossen, 2011). Both $\boldsymbol{M}_A$ and $\boldsymbol{M}_{RB}$ were determined using WAMIT in (Hval, 2012). From this $\boldsymbol{C}_A$ and $\boldsymbol{C}_{RB}$ can be computed. The coriolis-centripetal matrix, $\boldsymbol{C}_A$, can also be parametrized in different forms just as with $\boldsymbol{C}_{RB}$. Currently the calculation of $\boldsymbol{C}_A$ is excluded from the simulation model due to obscuring errors caused by its inclusion.

The damping terms are used to describe viscous effects, and other nonlinear drag phenomena that affect the underwater vehicle. It is difficult to separate the different types of effects causing drag, but it is in (Fossen, 2011) done using a linear and a quadratic term:

$\boldsymbol{D}(\boldsymbol{\nu}_r) = \boldsymbol{D}_L + \boldsymbol{D}_{NL}(\boldsymbol{\nu}_r)$

Usually computer programs are able to compute the damping values (Fossen, 2011), however in some cases the shape of a vehicle make it unsuitable for such calculations (Hval, 2012). For vehicles that have similar characteristics a rather simpler method to determine the hydrodynamic damping matrices can be used. More precisely if a second vehicle has kinematic similarity, geometric similarity and dynamic similarity with the vehicle having unknown damping coefficients, a ratio between the two vehicles can be used to determine the coefficients of the first (Steen, 2007). As noted in (Hval, 2012) this is the method used to calculate the damping coefficients of the modelled ROV. Even though the geometric shape of the Argus Mariner is unlike the template vehicle ROV Minerva, it was concluded in (Hval, 2012) that this would be the current best estimate of the coefficients for FHSim.

2.3.7 Thruster Forces

The thruster forces include all forces caused by the ROV thrusters.

$$\boldsymbol{\tau}_{act} = \sum_{i=1}^{k} \boldsymbol{\tau}_{thr}^{k} \tag{14}$$

$$\boldsymbol{\tau}_{thr}^{k} = sign(n) K_T \rho D^4 n^2 \tag{15}$$

were n is the propeller rotation in RPS, D is the diameter of rotor. K_T is a strictly positive coefficient based on loss effects of the thrust (Sørensen, 2013). The modelled thruster forces is often determined by a combination of empirical methods and analytical due to the complexity of such solutions (Sørensen, 2013). A table (in which a certain RPM of a thruster is associated with a given torque) is used by the controller to issue the required RPM of the propeller. The table of RPM/torque is however very sensitive to loss effects such as velocity fluctuations, ventilation, thruster-thruster interation and flow effects (Sørensen, 2013). Therefore, the accuracy of such a table isn't necessarily high for all operating conditions. The main challenge lies in assessing the thruster loss effects from non-modelled disturbances. The thruster forces in FHSim for the ROV are simulated using values generated from heuristic methods from (Roddy et al., 2006).

2.3.8 Wave Forces

Wave forces are distinguished by two parts, namely first order and second order wave-induced forces. The first order-induced forces are oscillatory with a zero mean. The second order forces are slow drift forces.

$\boldsymbol{\tau}_{wave} = \boldsymbol{\tau}_{wave1} + \boldsymbol{\tau}_{wave2}$

The motion induced by waves are dependent on the waves and the vessel. The induced wave forces were in (Hval, 2012) calculated using WAMIT, but later changed due to simulation inconsistencies and unrealistic values. Wave forces on the underwater vehicle are currently calculated using only Froude-Krylov forces, see section 2.5.2 page 14. This is an approximation since in this case the vehicle is treated as a rectangle, and relevant physical components such as viscosity and diffraction forces are not included in the calculations. The implemented wave force equals:

$$\boldsymbol{\tau}_{wave} = \iint p\boldsymbol{n}\,\mathrm{d}s.$$

were s is the submerged surface of the ROV, $\boldsymbol{n}$ is the unit vector normal to the body surface, and p is the pressure in the undisturbed wave field (pressure on the ROV, assuming it doesn't disturb the waves).

Due to the applied method, there is no separation between first order and second order wave forces for the ROV model in FHSim. The pressure difference is simulated in FHSim based on simulated waves.

2.4 ROV Total Model

The total process plant model used to simulate a submerged underwater ROV moving in a straight path can be defined as follows, (Fossen, 2011):

$$(\boldsymbol{M}_A + \boldsymbol{M}_{RB})\dot{\boldsymbol{\nu}} = -\boldsymbol{C}_{RB}(\boldsymbol{\nu})\boldsymbol{\nu} - \boldsymbol{C}_A(\boldsymbol{\nu}_r)\boldsymbol{\nu}_r - (\boldsymbol{D}_L + \boldsymbol{D}_{NL}(\boldsymbol{\nu}_r))\boldsymbol{\nu}_r - \mathbf{g}(\boldsymbol{\eta}) + \boldsymbol{\tau}_{act} + \boldsymbol{\tau}_{env} \tag{16}$$

Several of the terms in the ROV model have been changed in the FHSim implementation. Such as $\boldsymbol{C}_A(\boldsymbol{\nu}_r) = 0$. Also, in order to include better effects of the wave forces which were simplified

in section 2.3.8, the relative velocity includes impact of waves. $\boldsymbol{\nu}_r = \boldsymbol{\nu} - \boldsymbol{\nu}_p$ were $\boldsymbol{\nu}_p$ is defined as the velocity of the ocean at point $p = [x, y, z]$ were the ROV is located in the environment. This velocity is the sum of velocity caused by waves and current velocity $\boldsymbol{\nu}_p = \boldsymbol{\nu}_c + \boldsymbol{\nu}_w$. The inclusion of the $\boldsymbol{\nu}_w$ term is added, (as a simplification) to include the ignored effects of wave drift forces on the ROV, $\boldsymbol{\tau}_{wave2}$.

The PPM model used in FHSim is hence implemented as:

$$(\boldsymbol{M}_A + \boldsymbol{M}_{RB})\dot{\boldsymbol{\nu}} = -\boldsymbol{C}_{RB}(\boldsymbol{\nu})\boldsymbol{\nu} - (\boldsymbol{D}_L + \boldsymbol{D}_{NL}(\boldsymbol{\nu} - \boldsymbol{\nu}_p))(\boldsymbol{\nu} - \boldsymbol{\nu}_p) - \mathbf{g}(\boldsymbol{\eta}) + \boldsymbol{\tau}_{act} + \boldsymbol{\tau}_{wave} \quad (17)$$

The reader is referred to the appendix for numerical values of all model coefficients for the ROV in FHsim.

2.5 Ocean Wave Modelling

Ocean wave modelling is a very wide research area. This section will limit the discussion to the linear wave theory (Airy theory) that is used to simulate ocean wave for control related systems. More complicated methods that include nonlinear effects of waves, are not used in FHSim as of current date.

Waves are originated from tides and wind sources. The wind generates waves by causing ruffles on the waters' surface, and feeds energy to the motion of the sea (Raichlen, 2012). The types of waves formed is a complex matter, but it is dependent on the depth of the sea, wind velocity, wind fetch and more. There is an upper limit to the growth of waves with regards to wind fetch or wind duration (Raichlen, 2012). When the limit is reached one says that the ocean region is fully developed.

In theory waves are separated as long or short crested (Kurian et al., 2012). Long crested waves are defined as waves propagated from one direction, while shot crested waves are defined as the combination of different long crested waves propagated from different directions (Kurian et al., 2012). In reality one would expect only short crested waves to exist (Kurian et al., 2012), but that doesn't mean that on certain occasions the direction of waves are heavily favoured toward one direction.

2.5.1 Linear Wave Theory

A central part of this task is to assess the performance of the ROV in wave conditions. One method to simulate wave motion is by using linear wave theory (Airy theory) (Faltinsen, 1993). Water is assumed to be irrotational, inviscid and incompressible which makes it possible to use potential theory. This greatly simplifies analytical calculations. The alternative, yet more realistic, is to solve the Navier-Stokes equation with the continuity equation (Fossen, 2011). These problems however don't necessarily have analytical solutions, and may require large computing power to solve, limiting the areas of applications.

For the linear wave theory the ocean is assumed to have a horizontal sea bottom and a free-surface of infinite extent (Faltinsen, 1993). Further it is important that the waves are small relative to the water depth, and their height is relatively small to their length (Raichlen, 2012). The linear wave is defined as a single sinusoid (Raichlen, 2012). The mathematical characteristics of such a wave are included in (Faltinsen, 1993) and their derivations in for example (Newman, 1977).

FHSim uses the linear theory to simulate wave forces and pressure, however the exact method in which calculations are done is not known.

2.5.2 Linear Wave Response on a Marine Vessel

The marine craft wave response is analysed in two parts, see (Faltinsen, 1993) for details.

Wave Excitation Forces and moments on a body when the vessel is restrained from oscillating, but impacted by waves. Hydrodynamic loads are identified as added mass and damping terms, $\boldsymbol{M}_A$,$\boldsymbol{C}_A$, and restoring terms $\mathbf{g}(\boldsymbol{\eta})$.

Wave Reaction forces and moments on the vessel when it is forced to oscillate with a wave excitation frequency, without there being any waves. It includes the Froude-Kriloff and diffraction forces and moments.

The wave reaction forces are represented as τ_{wave}, see section 2.3.8. In the PPM model, as mentioned in section 2.3.8, the diffraction forces have been disregarded for the ROV in FHSim.

2.5.3 Wave Spectra

While the linear wave theory describes the characteristics of sinusoidal waves, it can't describe the irregular wave behaviour in the ocean. For this it is common to assume that the waves in an ocean is the linear sum of many independent regular wave components (Raichlen, 2012). More precisely; the irregular waves found in oceans are treated as the sum of many regular waves with differing frequencies (Faltinsen, 1993):

$$\zeta = \sum_{j=1}^{N} A_j \sin(w_j t - k_j x + \epsilon_j) \tag{18}$$

were ϵ_j is a random phase angle of wave component j. Thus ζ represents the sum of all regular waves in the ocean. This is assuming linear theory of the wave components, and is not suitable for modelling nonlinear wave phenomena, such as *rogue waves*, breaking waves or wave-wave interactions (Gibson et al., 2007; Katsardi and Swan, 2010). The direction of the waves are also determined by whether they are short or long crested. For a long crested wave, equation 18 is descriptive enough, however, to model short crested ways it is suggested to use a 2-D wave spectrum that distributes the wave's energy in different directions (Fossen, 2011).

The types of regular waves present in the ocean are characterized by the frequency spectra of the ocean wave, and certain parameters defining the sea state such as wave amplitudes and frequencies. Common descriptors of the ocean include the average wave period T_1, and the significant wave height H_s. The significant wave height defined as the mean wave height of the one-third highest waves.

The wave spectrum is a set of all frequencies of the regular waves one assumes that are present in the ocean. Different spectra types are used to simulate oceans of different nature, and are functions of the significant wave height, and average wave period.

A common notation for the wave spectrum is $S(w)$. Were w represents the frequency of a wave, and $S(w)$, its magnitude. There are numerous wave spectra available to simulate ocean waves, such as *Modified Pierson Moskowitz Spectrum*, *JONSWAP* and *Torsethaugen* spectrum. The Modified Pierson Moskowitz Spectrum was developed to model fully developed wind-generated seas based on analysis in the North Atlantic Ocean, and the JONSWAP spectrum and Torsethaugen spectrum are designed to model the North Sea. (Fossen, 2011). JONSWAP spectrum describes non-fully developed seas (Fossen, 2011). The JONSWAP spectrum is similar to the Modified Piersen Moskowitz spectrum, except it has a larger peak for the average wave frequency.

The definition of the JONSWAP spectrum is:

$$S(w) = 155\frac{H_s^2}{T_1^4}w^{-5}e^{\left(\frac{-944}{T_1^4}w^{-4}\right)}\gamma^Y \tag{19}$$

$$Y = e^{-\left(\frac{0.191wT_1-1}{\sqrt{2}\sigma}\right)^2} \tag{20}$$

$$\sigma = \begin{cases} 0.07 & \text{for } w \leq 5.24/T_1 \\ 0.09 & \text{for } w > 5.24/T_1 \end{cases} \tag{21}$$

$$\gamma = 3.3 \tag{22}$$

FHSim can simulate both a set of pre-defined regular waves or the JONSWAP spectrum as of the version used in the thesis. The wave direction can also be defined, either by specifying a direction and changing between long or short crested waves.

2.6 FHSim Simulating Environment and Workspace

FHSim is a software framework aimed at simulating especially marine systems in the time domain, using models described by ordinary differential equations (Reite et al., 2014). FHSim has an inbuilt wave and current generator and uses an integrator; either forward euler with discrete time steps, or continuous variable time step integrator, to simulate the implemented system behaviour. Objects in FHSim are programmed as SimObjects with any wanted attribute (Reite et al., 2014). The behaviour of the SimObject in regards to its environment is defined in its integration function. All SimObjects have a number of states $[0...n]$, and a number of input and output ports in which it can communicate with other SimObjects. Unfortunately as of the current version it is not possible to interact with the wave or current through SimObjects. That is, the SimObject cannot change the behaviour of the ocean current or wave by its presence. All outputs of SimObjects are stored in external files.

A major component of FHSim is its visualization component. All objects designed in FHSim can have an ascribed model, which is then visualized. This is particularly useful to analyse complex data, or for example, help debugging a program. In this thesis, the visualization component plays an important role for the ROV net exploration. As the ROV traverses the net, it is capable of colouring segments in the net which it has explored. The ROV will be able to use this to map the surface of a net such that an operator might see its shape. Other uses of the visualization component includes visualizing net deformation from ocean currents, see (Reite et al., 2014) for more examples.

3 Materials and Method

The ROV DP system has a guidance block, controller, thruster allocation and an observer. All of these were initially implemented in FHSim in (Hval, 2012). However, the ROV will be equipped with a DVL (doppler Velocity logs) sensor, and is thus capable of measuring velocity. This was not taken into consideration in (Hval, 2012). A DVL sensor uses beams to track a surface in front of it, then measure the velocity of the moving ROV by integrating the displacements caused by the identified surface. The DP system is in this thesis therefore extended to include handling of velocity measurements *and* position measurements. This includes modifying the nonlinear observer to handle velocity measurements in its wave filter, adding an Extended Kalman filter with wave filtering, adding a current estimator, and connecting them in cascade.

The practical applications of the DP system is also extended with the addition of the visualization component of FHSim. This includes using the ROV to identify explored regions of the fish cage in which it traverses, and using this data to autonomously traverse the fish cage netting.

3.1 Wave Filtering and Linear Approximations to Waves

Before describing the DP system in detail, a review is made of the implemented wave filter for the observers.

In many DP systems the vessel motion caused by waves are filtered out from the total vessel motion to reduce oscillatory inputs to the controller. The proper way to generate waves from the wave spectrum is done using equation 18. However, due to the large computation power required to do this fast, this method is best suited for a simulation program, and not for a control system designed to estimate wave motion. There are different methods for wave filtering in a control system. This section will mainly outline the usage of the second order linear wave filter. A good summary of the different filters are summed up in (Schei, 1996).

The first second order linear wave filter to work with a control system was published in (J.G et al., 1976),(Fossen, 2011). Later a fourth order filter was suggested in (Grimble et al., 1979). As of today these two variations are the most prevalent, and the research of interest is instead focused on self-tuning filters that can adapt to changing weather conditions, see (Hassani et al., 2012; Strand and Fossen, 1999; Torsetnes et al., 2004; J.G et al., 1976; Saelid et al., 1983).

The second order wave filter used today is based on (Saelid et al., 1983). The wave motion is treated as a second order equation, $\ddot{\eta}_w = -\omega_0^2\eta_w - 2\lambda\omega_0\dot{\eta}_w + K_w w$. were λ is a damping coefficient, ω_0 is the dominating wave frequency and w is white noise. Its transfer function:

$$h(s) = \frac{K_w s}{s^2 + 2\lambda\omega_0 s + \omega_0^2} \tag{23}$$

For the linear filter to best fit the modelled wave spectrum the following has to be satisfied: $S(\omega) = |h(jw)|^2$, (Fossen, 2011). For this to be true it is shown in (Fossen, 2011) that $K_w = 2\lambda\omega_0\sigma$, were $\sigma = \sqrt{S(\omega_0)}$. The relationship between dominating frequency ω_0 and average period T_1 for the Pierson-Moskowitz spectrum is (Fossen, 2011):

$$\omega_0 = \sqrt[4]{\frac{4B}{5}} \tag{24}$$

$$B = \frac{16\pi^3}{T_z^4} \tag{25}$$

$$T_z = 0.921T_1 \tag{26}$$

Although this relationship works quite well for the JONSWAP spectrum as well. Further, if $S(w)$ is computed as the JONSWAP spectrum, then the recommended damping coefficient λ is 0.1 (Fossen, 2011).

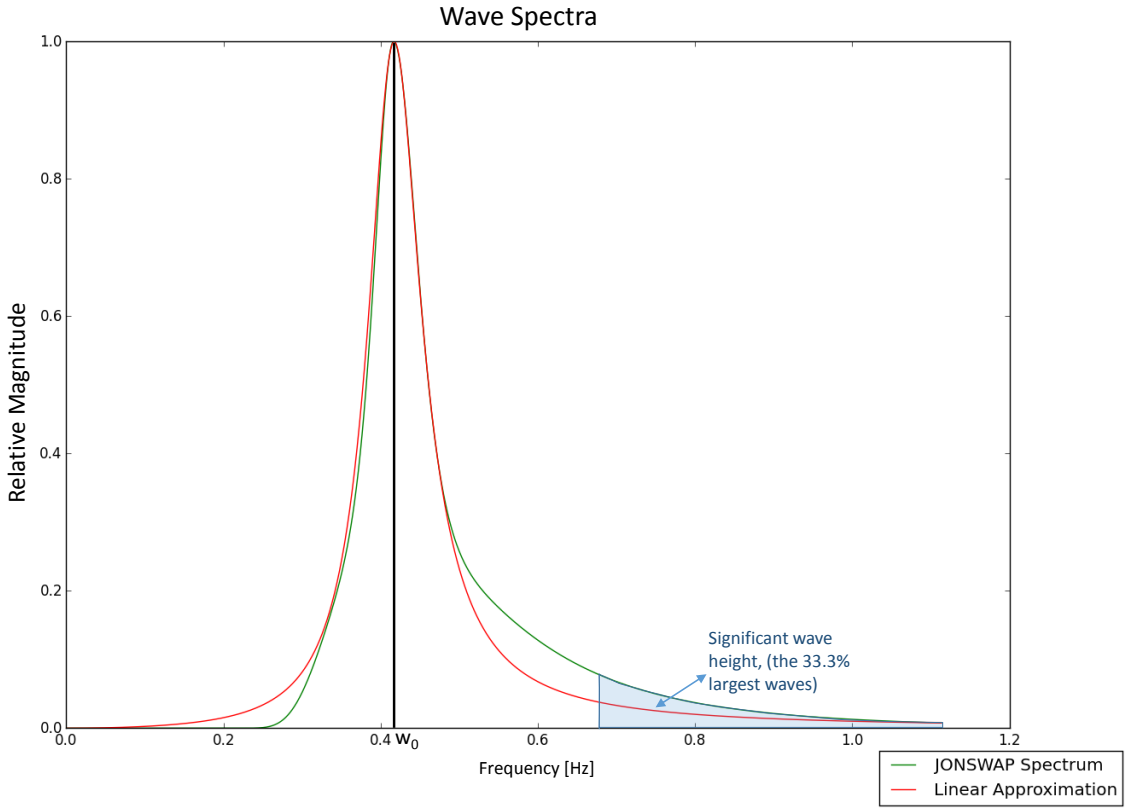

Figure 4: A comparison between the JONSWAP spectrum and the its second order linear approximation.

The second order filter is a fairly simple representation of the wave motions, and its main weakness is its inclusion of lower frequency motions (Grimble et al., 1979; Saelid et al., 1983), especially for the Pierson Moskowitz spectrum. The fourth order wave filter is better in this regard, however, it's also more difficult to determine its coefficients. Second order designs are favoured for their simplicity, and if used with a kalman observer, will result in quicker computation time due to a reduced number of states. Because of this, the second order filter was implemented in the DP system. As can be seen from figure 4, the second order linear approximation to the jonswap spectrum, if tuned optimally, is quite satisfying.

The main difficulties using wave filters lies in the erroneous tuning of the dominant frequency ω_0. It is often difficult to determine its optimal value. This has motivated research of adaptive wave filters that adaptively tune ω_0 to its optimal value. There was made a consideration of implementing an adaptive wave filter in the thesis, however by evaluating two of the most promising filters in (Hassani et al., 2012; Strand and Fossen, 1999) it was decided to not use adaptive wave filtering techniques.
The NPO adaptive wave filter from (Strand and Fossen, 1999) require a set of additional tuning parameters, and is not compatible with the implemented nonlinear observer in section 3.3.3. The adaptive wave filter in (Hassani et al., 2012) require a set of multiple Extended Kalman Filters (EKF), and further tuning of the adaptive filter. This increases the computational demand of the observer considerably. The adaptive filter in (Hassani et al., 2012) also doesn't demonstrate a high level of accuracy of the wave estimation.

3.2 DP ROV Model

The DP system of the ROV includes a LF model and a WF model, similar to what is commonly used in the literature for surface vessels, see for example (Sørensen, 2013; A.J. et al., 1996; Hassani et al., 2012; Fossen and Strand, 1999). It could be argued that a submersible ROV has no need for a WF model since it's mostly operating submerged. However, wave forces have a sufficient impact at small depths beneath the surface. Wave loads decrease exponentially as depth increases, see (Faltinsen, 1993; Hval, 2012). The ROV in this thesis will operate at depths of 2-50 meters. Hence the inclusion of a wave filter for the ROV is essential. Since the ROV will be able to measure its own velocity using a DVL, the WF motion is extended to include velocity measurements. The states in the DP system are expressed in $\boldsymbol{x} = [\boldsymbol{\xi}, \boldsymbol{\eta}, \boldsymbol{\nu}, \boldsymbol{b}], \in \mathbb{R}^{30}$, with $\boldsymbol{\xi} \in \mathbb{R}^{12}$, $\boldsymbol{\nu} \in \mathbb{R}^6$, $\boldsymbol{\eta} \in \mathbb{R}^6$, $\boldsymbol{b} \in \mathbb{R}^6$. For both position and velocity, only four dimensions are considered by the measurements, namely surge, sway, heave and yaw. Pitch and roll are assumed self-stabilizing and approximately equal to zero.

The total ROV motion is equal to:

$$\begin{aligned} \boldsymbol{\eta}_{total} &= \boldsymbol{\eta} + \boldsymbol{J}(\boldsymbol{\Theta})\boldsymbol{\xi}_1 \\ \boldsymbol{\nu}_{total} &= \boldsymbol{\nu} + \boldsymbol{\xi}_2 \end{aligned} \tag{27}$$

A second challenge for the ROV, is that it has to be controllable in the presence of high currents up to $0.5ms^{-1}$. The DP system therefore has an included current estimator as well. The DP system thus has a bias state *and* a current estimator.

3.2.1 LF Model

The LF model of the system is written in equation 28.

$$\begin{aligned} \dot{\boldsymbol{\eta}} &= \boldsymbol{J}(\boldsymbol{\Theta})\boldsymbol{\nu} \\ \boldsymbol{M}\dot{\boldsymbol{\nu}} + \boldsymbol{D}(\boldsymbol{\nu}_r)\boldsymbol{\nu}_r &= \boldsymbol{\tau} + \boldsymbol{J}^T(\boldsymbol{\Theta})\boldsymbol{b} \\ \dot{\boldsymbol{b}} &= -\boldsymbol{T}^{-1}\boldsymbol{b} + \boldsymbol{w} \end{aligned} \tag{28}$$

The LF model includes the main vessel dynamics, excluding coriolis and centripetal effects. Due to the shape and low velocity of the ROV these effects are presumed to have minimal effect on the vessel. The nonlinear damping term will have minimal impact on the vessel, since its max velocity is no more than $0.5ms^{-1}$, hence the damping term can be linearly simplified, $\boldsymbol{D}(\boldsymbol{\nu}_r)\boldsymbol{\nu}_r \approx \boldsymbol{D}_L\boldsymbol{\nu}_r$. Without too much loss of accuracy.

3.2.2 WF Model

The WF model of the DP system is a second order wave filter:

$$\begin{aligned} \dot{\boldsymbol{\xi}}_1 &= \boldsymbol{\xi}_2 \\ \dot{\boldsymbol{\xi}}_2 &= -\boldsymbol{\omega}^2\boldsymbol{\xi}_1 - 2\boldsymbol{\lambda}\boldsymbol{\omega}\boldsymbol{\xi}_2 + \boldsymbol{K}_w\boldsymbol{w}_w \end{aligned} \tag{29}$$

As previously shown in figure 4, the spectrum of this filter fits very well with the JONSWAP spectrum which is used in FHSim. $\boldsymbol{\omega} \in \mathbb{R}^6$, is a diagonal matrix of the dominating wave frequencies ω_{0i}, and $\boldsymbol{\lambda} \in \mathbb{R}^6$ is the diagonal matrix of damping terms λ_i. Equation 29 is commonly written in its compact form using $\boldsymbol{\xi} = [\boldsymbol{\xi}_1 \quad \boldsymbol{\xi}_2]^T$:

$$\dot{\boldsymbol{\xi}} = \boldsymbol{A}_w\boldsymbol{\xi} + \boldsymbol{E}_w\boldsymbol{w}_w \tag{30}$$

3.3 Observers

Important functions of an observer includes noise and wave filtering, and dead reckoning capabilities. In this section three types of observers will be presented. The relatively standard extended kalman filter, see (Sørensen, 2013), a nonlinear observer based on (Lindegaard and Fossen, 2001) and a current estimator (Refsnes, 2007). These will later be tested both independently and in cooperation with each other.

For the use of vessel observers, there exists essentially two types of observers. The luenberger, and the stochastic kalman filter observer. The NPO filter from (Fossen and Strand, 1999) might be regarded as a special case of the luenberg observer. The main differences between the observers are generally attributed to dead reckoning, computation time, fixed or adaptive gains, and stability. The luenberg observer does not innately have dead reckoning capabilities, but this can be implemented using a corrector-predictor representation of estimates, (Fossen, 2011). The luenberg observer potentially computes a lot faster than a kalman filter. This is important for real-time applications. Hence this puts an extra demand on the available computational power when using a kalman filter in a control system. In cases were such CPU power isn't available, the system is dependent on having a simple yet effective observer (Refsnes et al., 2007). The extended kalman filter is not proven globally asymptotically stable (Sørensen, 2013), although by restricting the Riccati equation matrix $\boldsymbol{P}$ by an upper bound, it can be shown to be incremental global exponential stable for continuous time (Jouffroy and Fossen, 2010). Many different types of luenberg observers are proven globally asymptotically stable, see (Fossen, 1994; Lindegaard, 2003; Lindegaard and Fossen, 2001; Refsnes, 2007) for some proofs. The kalman filter changes it gain matrix adaptively for optimal performance, while the luenberg observer has a fixed gain matrix.

3.3.1 Current Observers

The main role of current observers are to estimate the ocean current and direction. The most early form of a current observer is proposed in (J.G et al., 1976), in which it is included as separate current velocity states in a kalman filter. Later a more convenient and commonly used current estimator was proposed in (Fossen, 1994), were the current is modelled as a markow process bias force. This force mimics the current force that would push the vessel, but also includes unmodelled forces. The current model from (Fossen, 1994) was initially meant for larger ships or marine vessels weighing many tonnes. By using a bias force to model current, it is not possible to use relative velocities in the CPM model of the vessel, since then $\nu_c = 0$. An ROV weights considerably less than a marine vessels in which the current model in (Fossen, 1994) was originally developed for. The ROV speed will also be limited to about $0.5ms^{-1}$, the same dimensions of current speed. The difference between a small sized ROV vessel and larger ships is considerate, and because of that it was decided to add a current observer in this thesis and test the effects it would have on the performance of the DP system. (Refsnes, 2007) has documented different variations of model based current observers designed for a slender body autonomous underwater vehicle (AUV). (Aguiar and A.M., 2002) has also implemented a simple current observer independent of the ROV model. The observers designed in this thesis will be based on (Refsnes, 2007) due to the comprehensive study that are available in (Refsnes, 2007).

Independent Current Observer

The current can either be estimated as a state in the main observer, see for example (J.G et al., 1976). Or it can be estimated by a second independent observer. The independent current

observers are used as standalone units cooperating with a main observer. One such observer from (Refsnes, 2007) labelled **CIVM Ib** is defined:

$$\begin{aligned} \dot{\hat{\boldsymbol{\eta}}}_2 &= \boldsymbol{R}(\boldsymbol{\Theta})\hat{\boldsymbol{\nu}}_2 + \boldsymbol{K}_1\tilde{\boldsymbol{\eta}}_2 \\ \boldsymbol{M}_2\dot{\hat{\boldsymbol{\nu}}}_2 + \boldsymbol{D}_2(\hat{\boldsymbol{\nu}}_{2r})\hat{\boldsymbol{\nu}}_{2r} &= \boldsymbol{\tau}_2 + \boldsymbol{R}(\boldsymbol{\Theta})^T\boldsymbol{K}_2\tilde{\boldsymbol{\eta}}_2 \\ \dot{\hat{\boldsymbol{\nu}}}_{2c} &= -\boldsymbol{T}^{-1}\hat{\boldsymbol{\nu}}_{2c} + \boldsymbol{K}_3\tilde{\boldsymbol{\eta}}_2 \end{aligned} \tag{31}$$

The subscript 2 represents that the matrix is a subsection of the model matrix with dimensions surge, sway and heave, (thus excluding the angle parameters). Recommended values for the gain matrices are given in (Refsnes, 2007). The observer has shown to have robust qualities in (Refsnes, 2007). It should also be noted from (Refsnes, 2007), that this particular observer is dependent on that the surge damping coefficient in $\boldsymbol{D}_2$ is correct for accurate current estimations.

The current observer **CIVM Ib** can be extended if the system has velocity measurements. For notation simplicity $\boldsymbol{R}(\boldsymbol{\Theta}) = \boldsymbol{R}$. This is not explored in (Refsnes, 2007), but instead added in this thesis since velocity measurements are available. Note that $\boldsymbol{\nu}_c$ is defined in the NED frame.

$$\begin{aligned} \dot{\hat{\boldsymbol{\eta}}}_2 &= \boldsymbol{R}\hat{\boldsymbol{\nu}}_2 + \boldsymbol{K}_{1p}\tilde{\boldsymbol{\eta}}_2 + \boldsymbol{R}\boldsymbol{K}_{1\nu}\tilde{\boldsymbol{\nu}}_2 \\ \boldsymbol{M}_2\dot{\hat{\boldsymbol{\nu}}}_2 + \boldsymbol{D}_2(\hat{\boldsymbol{\nu}}_{2r})\hat{\boldsymbol{\nu}}_{2r} &= \boldsymbol{\tau}_2 + \boldsymbol{R}^T\boldsymbol{K}_{2p}\tilde{\boldsymbol{\eta}}_2 + \boldsymbol{K}_{2\nu}\tilde{\boldsymbol{\nu}}_2 \\ \dot{\hat{\boldsymbol{\nu}}}_{2c} &= -\boldsymbol{T}^{-1}\hat{\boldsymbol{\nu}}_{2c} + \boldsymbol{K}_{3p}\tilde{\boldsymbol{\eta}}_2 + \boldsymbol{R}\boldsymbol{K}_{3\nu}\tilde{\boldsymbol{\nu}}_2 \end{aligned} \tag{32}$$

Defining the errors as $\tilde{\boldsymbol{x}}_2 = \boldsymbol{x}_2 - \hat{\boldsymbol{x}}_2$, and using property 4 in appendix, the error dynamics of the observer can be written as:

$$\begin{bmatrix} \dot{\tilde{\boldsymbol{\eta}}}_2 \\ \boldsymbol{M}_2\dot{\tilde{\boldsymbol{\nu}}}_{2r} \\ \dot{\tilde{\boldsymbol{\nu}}}_{2c} \end{bmatrix} = \begin{bmatrix} -\boldsymbol{K}_{1p} + \boldsymbol{\epsilon} & \boldsymbol{R}(\boldsymbol{I} - \boldsymbol{K}_{1\nu}) & \boldsymbol{I} - \boldsymbol{K}_{1\nu} \\ -\boldsymbol{R}^T\boldsymbol{K}_{2p} & -\boldsymbol{K}_{2\nu} & \boldsymbol{R}^T(\boldsymbol{M}_2 - \boldsymbol{K}_{2\nu}) \\ -\boldsymbol{K}_{3p} & -\boldsymbol{R}\boldsymbol{K}_{3\nu} & -\boldsymbol{T}^{-1} - \boldsymbol{K}_{3\nu} + \boldsymbol{\epsilon} \end{bmatrix} \begin{bmatrix} \tilde{\boldsymbol{\eta}}_2 \\ \tilde{\boldsymbol{\nu}}_{2r} \\ \tilde{\boldsymbol{\nu}}_{2c} \end{bmatrix} - \begin{bmatrix} \boldsymbol{\epsilon}\tilde{\boldsymbol{\eta}}_2 \\ \delta(e_{\tilde{\boldsymbol{\nu}}_{2r}})\tilde{\boldsymbol{\nu}}_{2r} \\ \boldsymbol{\epsilon}\tilde{\boldsymbol{\nu}}_{2c} \end{bmatrix} \tag{33}$$

were, similarly to (Refsnes, 2007), $0 < \boldsymbol{\epsilon} < 1$ is an arbitrarily small constant added to help with the stability derivation. This error dynamic is proven UGES in (Refsnes, 2007) *if* velocity measurements are not used. However, no stability proof of the system with velocity measurements will be given in this text. Based on the simulation results the system is demonstrated to be at least asymptotically stable.

3.3.2 Discrete Extended Kalman Filter

In this thesis it was decided to add a discrete extended kalman filter, and see how it would compete with the nonlinear observer. The discrete Extended Kalman Filter (EKF) is a discrete stochastic observer in which the diagonal matrices $\boldsymbol{Q}$ and $\boldsymbol{R}$ are used to tune the observer. The EKF used in this thesis is a 30 state observer with a total of 24 potential tuning parameters; $\boldsymbol{R} \in \mathbb{R}^{12}$, $\boldsymbol{Q} \in \mathbb{R}^{12}$. However, the measurement covariance matrix $\boldsymbol{R}$ is set equal to the known covariance measurement noise errors, and since no measurements are performed in ϕ and θ ($\phi, \theta \approx 0$), there are only 8 tuning parameters in $\boldsymbol{Q}$. The total tuning parameters of the EKF are such reduced from 24 to 8. Using the nonlinear DP system model:

$$\begin{aligned} \dot{\boldsymbol{x}} &= \boldsymbol{f}(\boldsymbol{x}) + \boldsymbol{B}\boldsymbol{u} + \boldsymbol{E}\boldsymbol{w} \\ \boldsymbol{y} &= \boldsymbol{H}\boldsymbol{x} + \boldsymbol{v} \end{aligned} \tag{34}$$

With $\boldsymbol{x} = [\boldsymbol{\xi}, \boldsymbol{\eta}, \boldsymbol{\nu}, \boldsymbol{b}]$, $\boldsymbol{\xi} \in \mathbb{R}^{12}$, $\boldsymbol{\nu} \in \mathbb{R}^{6}$, $\boldsymbol{\eta} \in \mathbb{R}^{6}$, $\boldsymbol{b} \in \mathbb{R}^{6}$, process noise $\boldsymbol{w} = [\boldsymbol{w}_w \quad \boldsymbol{w}_b] \in \mathbb{R}^{12}$, and measurement noise $\boldsymbol{v} = [\boldsymbol{v}_\eta \quad \boldsymbol{v}_\nu] \in \mathbb{R}^{12}$, the Extended Kalman Filter (EKF) model is implemented as such:

$$\begin{aligned} \dot{\hat{\boldsymbol{\xi}}} &= \boldsymbol{A}_w \hat{\boldsymbol{\xi}} + \boldsymbol{E}_w \boldsymbol{w}_w \\ \dot{\hat{\boldsymbol{\eta}}} &= \boldsymbol{J}(\psi)\hat{\boldsymbol{\nu}} \\ \boldsymbol{M}\dot{\hat{\boldsymbol{\nu}}} + \boldsymbol{D}(\hat{\boldsymbol{\nu}}_r)\hat{\boldsymbol{\nu}}_r &= \boldsymbol{\tau}_2 + \boldsymbol{J}^T(\psi)\hat{\boldsymbol{b}} \\ \dot{\hat{\boldsymbol{b}}} &= -\boldsymbol{T}^{-1}\hat{\boldsymbol{b}} + \boldsymbol{w}_b \\ \boldsymbol{\eta}_w &= \boldsymbol{J}(\psi)\hat{\boldsymbol{\xi}}_1 \\ \boldsymbol{\nu}_w &= \hat{\boldsymbol{\xi}}_2 \end{aligned} \tag{35}$$

$$\boldsymbol{y} = \begin{bmatrix} \boldsymbol{\eta} + \boldsymbol{\eta}_w + \boldsymbol{v}_\eta \\ \boldsymbol{\nu} + \boldsymbol{\nu}_w + \boldsymbol{v}_\nu \end{bmatrix}$$

The EKF algorithm in this thesis is based on (Fossen, 2011), with $\boldsymbol{R}$ and $\boldsymbol{Q}$ diagonal and constant, and a bounded $\boldsymbol{P}$. See algorithm 1 in appendix.

$$\boldsymbol{E} = \begin{bmatrix} \boldsymbol{0}_{6x6} & \boldsymbol{0}_{6x6} \\ \boldsymbol{K}_w & \boldsymbol{0}_{6x6} \\ \boldsymbol{0}_{6x6} & \boldsymbol{0}_{6x6} \\ \boldsymbol{0}_{6x6} & \boldsymbol{0}_{6x6} \\ \boldsymbol{0}_{6x6} & \boldsymbol{I}_{6x6} \end{bmatrix}, \boldsymbol{B} = \begin{bmatrix} \boldsymbol{0}_{6x6} \\ \boldsymbol{0}_{6x6} \\ \boldsymbol{0}_{6x6} \\ \boldsymbol{M}^{-1} \\ \boldsymbol{0}_{6x6} \end{bmatrix}, \boldsymbol{f}(\boldsymbol{x}) = \begin{bmatrix} \boldsymbol{A}_w \boldsymbol{\xi} \\ \boldsymbol{J}(\psi)\boldsymbol{\nu} \\ \boldsymbol{M}^{-1}\left(-\boldsymbol{D}(\boldsymbol{\nu}_r)\boldsymbol{\nu}_r + \boldsymbol{J}^T(\psi)\boldsymbol{b}\right) \\ -\boldsymbol{T}^{-1}\boldsymbol{b} \end{bmatrix} \tag{36}$$

Process noise $\boldsymbol{w}$ are given both to the wave model $\boldsymbol{\xi}$ and bias $\boldsymbol{b}$. The structure of $\boldsymbol{E}$ allows for separate tuning possibilities of the wave model and bias terms.

Dead Reckoning for Extended Kalman Filter

The EKF is innately attributed with dead reckoning capabilities. The estimated state update of the EKF is defined as:

$$\dot{\hat{\boldsymbol{x}}}(k) = \bar{\boldsymbol{x}}(k) + \boldsymbol{K}(\boldsymbol{y}(k) - \bar{\boldsymbol{y}}(k)) \tag{37}$$

The future predicted state is defined as:

$$\bar{\boldsymbol{x}}(k+1) = \bar{\boldsymbol{x}}(k) + h(\boldsymbol{f}(\hat{\boldsymbol{x}}(k)) + \boldsymbol{B}\boldsymbol{u}(k)) \tag{38}$$

If a measured signal $y_i(k)$ is lost, or not updated, it is wanted that the observer is only dependent on its predicted value $\bar{x}_i$ (Fossen, 2011). Hence for measurements that are lost, the estimated error for that dimension i, is defined as zero: $y_i(k) - \bar{y}_i(k) = 0$. By suggesting that the estimation error is set equal to zero instead of the gain, it is possible to update the estimates that still have measurements, while estimates without measurements are only predicted. This is an especially attractive feature which allows the observer to distinguish between lost position and lost velocity measurements when performing dead reckoning.

3.3.3 Nonlinear Observer

In (Hval, 2012) it was documented that the previously implemented observer was a Nonlinear Passive Observer (NPO), however since the ROV will have access to velocity measurements, the observer in this thesis has been extended to include velocity measurements with wave filtering. A NPO-like observer extended to include velocity (and acceleration) measurements is thoroughly studied in (Lindegaard, 2003). The main challenge of observers with position, velocity and acceleration measurements lies in studying the added non-linearities caused by the injection terms originating from different reference frames.

The nonlinear observer is defined as following:

$$\begin{aligned}
\dot{\hat{\boldsymbol{\xi}}} &= \boldsymbol{A}_w \hat{\boldsymbol{\xi}} + \boldsymbol{K}_{1\nu} \tilde{\boldsymbol{\nu}} \\
\dot{\hat{\boldsymbol{\eta}}} &= \boldsymbol{J}(\psi) \hat{\boldsymbol{\nu}} + \boldsymbol{K}_{2\eta} \tilde{\boldsymbol{\eta}} + \boldsymbol{J}(\psi) \boldsymbol{K}_{2\nu} \tilde{\boldsymbol{\nu}} \\
\boldsymbol{M} \dot{\hat{\boldsymbol{\nu}}} + \boldsymbol{D} \hat{\boldsymbol{\nu}}_r &= \boldsymbol{\tau}_2 + \boldsymbol{J}^T(\psi) \hat{\boldsymbol{b}} + \boldsymbol{J}^T(\psi) \boldsymbol{K}_{3\eta} \tilde{\boldsymbol{\eta}} + \boldsymbol{K}_{3\nu} \tilde{\boldsymbol{\nu}} \\
\dot{\hat{\boldsymbol{b}}} &= -\boldsymbol{T}_b^{-1} \hat{\boldsymbol{b}} + \boldsymbol{K}_{4\eta} \tilde{\boldsymbol{\eta}} + \boldsymbol{J}(\psi) \boldsymbol{K}_{4\nu} \tilde{\boldsymbol{\nu}} \\
\boldsymbol{\eta}_w &= \boldsymbol{J}(\psi) \hat{\boldsymbol{\xi}}_1 \\
\boldsymbol{\nu}_w &= \hat{\boldsymbol{\xi}}_2
\end{aligned} \tag{39}$$

$$\boldsymbol{y} = \begin{bmatrix} \boldsymbol{\eta} + \boldsymbol{\eta}_w \\ \boldsymbol{\nu} + \boldsymbol{\nu}_w \end{bmatrix}$$

The error dynamics of this system can be written as:

$$\begin{aligned}
\dot{\tilde{\boldsymbol{\xi}}} &= \boldsymbol{A}_w \tilde{\boldsymbol{\xi}} - \boldsymbol{K}_{1\nu} \tilde{\boldsymbol{\nu}} \\
\dot{\tilde{\boldsymbol{\eta}}} &= \boldsymbol{J}(\psi) \tilde{\boldsymbol{\nu}} - \boldsymbol{K}_{2\eta} \tilde{\boldsymbol{\eta}} - \boldsymbol{J}(\psi) \boldsymbol{K}_{2\nu} \tilde{\boldsymbol{\nu}} \\
\boldsymbol{M} \dot{\tilde{\boldsymbol{\nu}}} &= \boldsymbol{J}^T(\psi) \tilde{\boldsymbol{b}} - \boldsymbol{D} \tilde{\boldsymbol{\nu}}_r - \boldsymbol{J}^T(\psi) \boldsymbol{K}_{3\eta} \tilde{\boldsymbol{\eta}} - \boldsymbol{K}_{3\nu} \tilde{\boldsymbol{\nu}} \\
\dot{\tilde{\boldsymbol{b}}} &= -\boldsymbol{T}_b^{-1} \tilde{\boldsymbol{b}} - \boldsymbol{K}_{4\eta} \tilde{\boldsymbol{\eta}} - \boldsymbol{J}(\psi) \boldsymbol{K}_{4\nu} \tilde{\boldsymbol{\nu}}
\end{aligned} \tag{40}$$

And in compact form:

$$\underbrace{\begin{bmatrix} \dot{\tilde{\boldsymbol{\xi}}} \\ \dot{\tilde{\boldsymbol{\eta}}} \\ \boldsymbol{M} \dot{\tilde{\boldsymbol{\nu}}} \\ \dot{\tilde{\boldsymbol{b}}} \end{bmatrix}}_{\dot{\boldsymbol{e}}} = \underbrace{\begin{bmatrix} \boldsymbol{A}_w & \boldsymbol{0} & -\boldsymbol{K}_{1\nu} & \boldsymbol{0} \\ \boldsymbol{0} & -\boldsymbol{K}_{2\eta} & \boldsymbol{J}(\psi)(\boldsymbol{I} - \boldsymbol{K}_{2\nu}) & \boldsymbol{0} \\ \boldsymbol{0} & -\boldsymbol{J}(\psi)^T \boldsymbol{K}_{3\eta} & -\boldsymbol{D} - \boldsymbol{K}_{3\nu} & \boldsymbol{J}(\psi)^T \\ \boldsymbol{0} & -\boldsymbol{K}_{4\eta} & -\boldsymbol{J}(\psi) \boldsymbol{K}_{4\nu} & -\boldsymbol{T}_b^{-1} \end{bmatrix}}_{\boldsymbol{I}(\psi)} \begin{bmatrix} \tilde{\boldsymbol{\xi}} \\ \tilde{\boldsymbol{\eta}} \\ \tilde{\boldsymbol{\nu}} \\ \tilde{\boldsymbol{b}} \end{bmatrix} + \underbrace{\begin{bmatrix} \boldsymbol{0} \\ \boldsymbol{0} \\ \boldsymbol{D} \tilde{\boldsymbol{\nu}}_c \\ \boldsymbol{0} \end{bmatrix}}_{\boldsymbol{II}} \tag{41}$$

Assuming that the current estimator is asymptotically stable, and independent of the nonlinear observer, then system $\boldsymbol{II} \rightarrow \boldsymbol{0}$. (The cascaded system of a current observer with a main observer will not be analysed, but is considered in (Refsnes, 2007) for observers with only position measurements).

By choosing $\boldsymbol{K}_{i\eta}$, $\boldsymbol{K}_{i\nu}$ so they commute with $\boldsymbol{J}(\psi)$ (see property 2 appendix), and property 1 in appendix holds, then system $\dot{\boldsymbol{e}} = \boldsymbol{I}(\psi)\boldsymbol{e}$ can be written $\dot{\boldsymbol{e}} = \boldsymbol{T}(\psi)^T\boldsymbol{I}\boldsymbol{T}(\psi)\boldsymbol{e}$. Which can be written $\dot{\boldsymbol{e}} = \boldsymbol{I}\boldsymbol{e}$, see (Lindegaard, 2003). Then UGES of $\dot{\boldsymbol{e}} = \boldsymbol{I}\boldsymbol{e}$ is guaranteed if $\boldsymbol{I}$ is choosen to be Hurwitz (Lindegaard, 2003).

Remark on system I

The format of $\boldsymbol{I}$ is suitable for cases in which the position and velocity measurements are synchronized. Stability could be fatal if for example the time delays of various sensor components are different (Lindegaard, 2003). This might occur in practice (as opposed to simulation).

A second challenge lies in tuning $\boldsymbol{I}$. While the NPO filter has clear tuning rules, this nonlinear observer does not. The tuning procedure is much more complicated when position and velocity measurement are present. As implemented, system $\boldsymbol{I}$ has more tuning parameters than the EKF. However in order to alleviate some of this, the wave filtering in equation 39 is designed so it can only be tuned using velocity measurements. This makes it possible to use the same wave filter tuning rules as the NPO filter to get the desired wave filter notch effect (Fossen and Strand, 1999). However it is up to the user to decide if he/she wants to use both position and velocity gains to tune the nonlinear observer. A strength of using both position and velocity measurements lies in an increased robustness against dead reckoning, hence this is the preferred structure.

(Lindegaard, 2003) proposes a different structure of $\boldsymbol{I}$ in order to reduce the number of tuning parameters. In this thesis, the observer was tuned such that $\boldsymbol{K}_{2\nu} = \boldsymbol{0}$ and $\boldsymbol{K}_{3\nu} = \boldsymbol{0}$.

Tuning of I

Although the user is free to tune the observer freely, the wave filter gain $\boldsymbol{K}_{1\nu}$ should be tuned according to a nonlinear passive observer (Fossen and Strand, 1999; Lindegaard, 2003). The form of $\boldsymbol{K}_{1\nu} = [\boldsymbol{K}^1_{1\nu} \;\; \boldsymbol{K}^2_{2\nu}]^T$, and $\boldsymbol{K}^i_{1\nu} \in \mathbb{R}^6, i = 1, 2$ are diagonal matrices.

$$\boldsymbol{K}_{1\nu} = \begin{bmatrix} K_1^1 & 0 & 0 & 0 & 0 & 0 \\ 0 & K_2^1 & 0 & 0 & 0 & 0 \\ 0 & 0 & K_3^1 & 0 & 0 & 0 \\ 0 & 0 & 0 & K_4^1 & 0 & 0 \\ 0 & 0 & 0 & 0 & K_5^1 & 0 \\ 0 & 0 & 0 & 0 & 0 & K_6^1 \\ K_1^2 & 0 & 0 & 0 & 0 & 0 \\ 0 & K_2^2 & 0 & 0 & 0 & 0 \\ 0 & 0 & K_3^2 & 0 & 0 & 0 \\ 0 & 0 & 0 & K_4^2 & 0 & 0 \\ 0 & 0 & 0 & 0 & K_5^2 & 0 \\ 0 & 0 & 0 & 0 & 0 & K_6^2 \end{bmatrix} \tag{42}$$

$$K_i^1 = -2(\zeta_{ni} - \lambda_i)\frac{\omega_{ci}}{\omega_{0i}} \tag{43}$$

$$K_i^2 = 2\omega_{0i}(\zeta_{ni} - \lambda_i) \tag{44}$$

For the JONSWAP spectrum, $\lambda_i = 0.1$. ζ_{ni} is typically 1.0 (Fossen, 2011), $\omega_{0i} = \omega_0$ is the wave dominating frequency. $\omega_{ci} > \omega_{0i}$ is the filter cutoff frequency.

Dead Reckoning for the Nonlinear Observer

The nonlinear observer uses the same approach for dead reckoning as the EKF does. That is, if a measurement signal $y_i(t)$ is lost or not updated then the estimation error for that measurement is set to zero, $\tilde{y}_i = 0$. This applies to both velocity and position measurements.

3.3.4 Cascaded System and Dead Reckoning

The main observer, either EKF or nonlinear observer, are used together with the current observer to generate the estimated states.

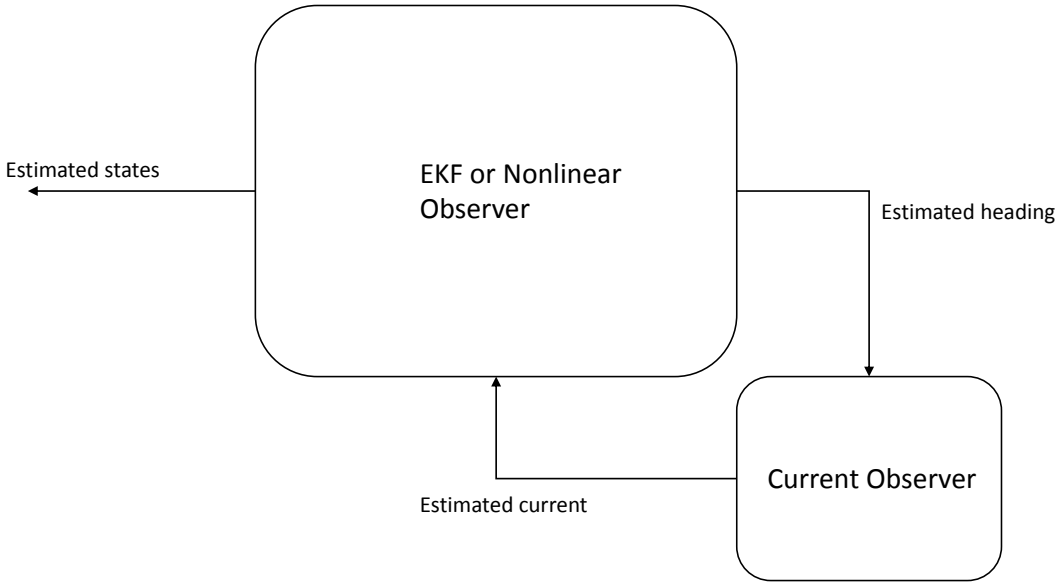

Figure 5: Cascaded System of main observer and a current observer

Dead reckoning on the cascaded system is dependent on that both systems have good dead reckoning capabilities. It was found that the estimated current is unfortunately not accurate if the current observer uses the same dead reckoning strategies as the EKF and nonlinear observer. One difficulty was that the estimated current became increasingly worse, and the transition between normal operation and dead reckoning gave a disruptive spike in the estimated values of the current observer. Hence dead reckoning for the current observer is defined such that if both the position and velocity measurement signals are lost then the current observer stops updating estimated current as such:

$$\dot{\boldsymbol{\nu}}_{2c} = \mathbf{0} \tag{45}$$

Since ocean current is generally slowly varying, this is a fine assumption. The main weakness using this method is based on that current changes direction and magnitude at varying depths. Nonetheless, this is seen as an adequate method to minimize dead reckoning errors based on simulation results.

A second modification during dead reckoning is that the current observer replaces the lost measurements with the estimated states from the EKF or nonlinear observer. It was found that this enabled a smooth transition between the normal operating stages and dead reckoning stages for the current observer.

3.4 Controller

The ROV controller is a nonlinear PID controller based on (Fossen, 2011), (Hval, 2012). Based on simulation results the used controller behaves satisfactory, and no modifications of it were applied in this thesis.

The control law choosen is:

$$\boldsymbol{\tau}_{PID} = -\boldsymbol{J}(\boldsymbol{\Theta})^T[\boldsymbol{K}_p\tilde{\boldsymbol{\eta}} + \boldsymbol{K}_d\boldsymbol{J}(\boldsymbol{\Theta})\tilde{\boldsymbol{\nu}} + \boldsymbol{K}_i\int_0^T \tilde{\boldsymbol{\eta}}\,\mathrm{d}t] \tag{46}$$

where $\boldsymbol{K}_p$, $\boldsymbol{K}_i$, $\boldsymbol{K}_d$ are tuning matrices for proportional, integral and derivative term respectively, see (Hval, 2012). $\tilde{\boldsymbol{\eta}}$ and $\tilde{\boldsymbol{\nu}}$ are the errors between the estimated states and the desired states from the reference model from the guidance block, see section 3.5. $\tilde{\boldsymbol{\eta}} = \hat{\boldsymbol{\eta}} - \boldsymbol{\eta}_d$, $\tilde{\boldsymbol{\nu}} = \hat{\boldsymbol{\nu}} - \boldsymbol{\nu}_d$.

A second reference feedforward term is added:

$$\boldsymbol{\tau}_{FF} = \boldsymbol{M}\boldsymbol{a}_d + \boldsymbol{D}_L\boldsymbol{\nu}_d + \boldsymbol{D}_{NL}(\boldsymbol{\nu}_d) \tag{47}$$

were $\boldsymbol{M} = \boldsymbol{M}_{RB} + \boldsymbol{M}_A$. $\boldsymbol{D}_L$ is the linear damping matrix, and $\boldsymbol{D}_{NL}(\boldsymbol{\nu}_d)$ is the quadratic damping matrix.

The total control force is finally is given as:

$$\boldsymbol{\tau}_{thr} = \boldsymbol{\tau}_{PID} + \boldsymbol{\tau}_{FF} \tag{48}$$

3.4.1 Integral wind-up

Using an integrator in the controller can lead to undesired overshooting effects, or instability when the accumulated error $\left(\int_0^T \tilde{\boldsymbol{\eta}}\,\mathrm{d}t\right)$ gets too large. In such a case the integral term will dominate the $\boldsymbol{\tau}_{PID}$ term causing undesirable effects. Two particular scenarios can cause these effects: First, if there is a continual bias in the error, thus accumulated error is always increased. Secondly, if a very sharp setpoint change occurs, the signal error will drastically increase so much that the signal will overshoot when reaching the reference point, however, by properly tuning the reference model in the guidance block, such effects will be minimized. The main risk factors of using the integrator is associated with bias errors, which ultimately will make the controller unstable. In order to alleviate these issues an integral wind-up algorithm was designed in (Hval, 2012) using saturating terms. The integral term in equation 46 is changed accordingly:

$$\boldsymbol{\tau}_i = \boldsymbol{K}_i\int\tilde{\boldsymbol{\eta}} + \boldsymbol{K}_{anti}[\mathtt{sat}(\boldsymbol{K}_i\int\tilde{\boldsymbol{\eta}}, \boldsymbol{\tau}_{min}, \boldsymbol{\tau}_{min}) - \boldsymbol{K}_i\int\tilde{\boldsymbol{\eta}}] \tag{49}$$

were $\boldsymbol{K}_{anti}$ is the matrix of anti windup tuning constants and $\mathtt{sat}(\boldsymbol{K}_i\int\tilde{\boldsymbol{\eta}}, \boldsymbol{\tau}_{min}, \boldsymbol{\tau}_{min})$ calculates the saturated value of the force (Hval, 2012).

3.5 Guidance System

The guidance system developed for the ROV is designed to take in positional waypoints in the four dimensions, $[x, y, z, \psi]$, as input and generate smooth reference trajectories in both position, velocity and acceleration to the controller. The guidance is designed so that the ROV will move through all the waypoints in a straight-path manner. When the ROV reaches the final waypoint, it will remain stationary.

The guidance system has two distinct components. The first component is responsible for generating reference points to the ROV in $[x, y, z, \psi]$. These references will make the ROV move in a straight line through succeeding waypoints. The module runs a set of logic tests to determine the next references to the ROV. In general these references are determined as follows: If the ROV is within a certain distance to its current next waypoint, then input the next waypoint for the ROV.

The waypoint generator was previously implemented with two operation modes. First the *Predefined* and secondly the *AutoNetCage*. The predefined mode allows the user to specify the waypoints which the ROV must travel through in succeeding order. The AutoNetCage mode is an exotic extension developed in (Hval, 2012) in which it is assumed that the geometry of a net cage is known. The program then generates waypoints for the ROV such that it will traverse the cage in a systematic manner.

The AutoNetCage mode is, however, flawed in that it assumes that the net geometry is known in advance. In most cases this is not true. A third mode was therefore added in this thesis and is extensively described in 3.7.4. In this mode it is assumed that the net geometry is unknown, but can be identified by the ROV as it explores the net. Based on the identified net segments waypoints are continuously generated online such that the ROV will ideally traverse the entire net surface systematically.

The second component of the guidance is a third order desired reference model for the ROV that smooths out the changes in reference points. Its input is positional references, and it outputs the corresponding response in position, velocity, and acceleration which are connected to the controller. The positional reference model used is described in Fossen (2011):

$$\boldsymbol{A_d} = \begin{bmatrix} \boldsymbol{0} & \boldsymbol{I} & \boldsymbol{0} \\ \boldsymbol{0} & \boldsymbol{0} & \boldsymbol{I} \\ -\boldsymbol{\Omega^3} & -(\boldsymbol{2\Delta} + \boldsymbol{I})\boldsymbol{\Omega^2} & -(\boldsymbol{2\Delta} + \boldsymbol{I})\boldsymbol{\Omega} \end{bmatrix} \quad \boldsymbol{B_d} = \begin{bmatrix} \boldsymbol{0} \\ \boldsymbol{0} \\ \boldsymbol{\Omega^3} \end{bmatrix} \tag{50}$$

With $\boldsymbol{x} = [\boldsymbol{\eta_d}\ \dot{\boldsymbol{\eta}}_{\boldsymbol{d}}\ \ddot{\boldsymbol{\eta}}_{\boldsymbol{d}}]^{\boldsymbol{T}} \in \mathbb{R}^{1x12}$, and $\boldsymbol{\eta_d} = [x\ y\ z\ \psi] \in \mathbb{R}^{1x4}$.

This component uses pre defined saturation limits of velocity and acceleration. The reference model is a simple mass-damper-spring system of $\boldsymbol{\Delta}$ and $\boldsymbol{\Omega}$, in which $\boldsymbol{\Delta}$ corresponds to the frequency response and $\boldsymbol{\Delta}$ the damping. These parameters were tuned so that the references could be followed by the ROV. In theory $\boldsymbol{\Delta}$ should equal 1 to avoid reference overshoots, however due to time delays in FHSim 1.2 gave better results.

3.6 Thruster Allocation

The DP system thruster allocation is implemented in the most basic form. That is, a transformation, $\boldsymbol{T}_{3\times6}(\boldsymbol{\alpha})$ between the thruster forces in NED and to the ROV's respective thrusters, see (Sørensen, 2013). The ROV has six thrusters in total.

$$\boldsymbol{u}_d = \boldsymbol{K}^{-1}\boldsymbol{T}^{+}_{3\times r}(\boldsymbol{\alpha})\boldsymbol{\tau}_c \tag{51}$$

were $\boldsymbol{u}_d \in \mathbb{R}^6$ is the commanded thrust for the respective thruster, and $\boldsymbol{K}^{-1}$ is a diagonal matrix of thrust force coefficients (Sørensen, 2013). $\boldsymbol{\tau}_c$ is the thruster forces assigned from the controller. $\boldsymbol{T}^{+}_{3\times r}(\boldsymbol{\alpha})$ is the pseudo inverse thruster transformation matrix.

The ROV has self stabilizing roll and pitch moments, hence there is no need to control these headings.

3.7 ROV Autonomous Net Traversing

This section examines the possibility of making the ROV traverse an entire fish cage autonomously based on DVL (doppler Velocity logs) measurements. The relative displacement between the ROV and the identified surface tracked by the DVL makes it possible to position the relative position of the ROV in a more general reference frame. In such a way it is also possible to position the identified surface in that reference frame, and hence identify the position of the netting. A minor difficulty using the DVL sensor is that drift errors can be caused by prolonged integration. In this text, however, it is assumed that the DVL functions perfectly.

For the general case the ROV should be able to traverse a net of arbitrary shape, however, this section focuses on a fixed known shape using already implemented modules of the ROV's DP system. This section is inspired by (Dukan, 2014) were the ROV can follow the surface of the ocean floor with a fixed distance.

3.7.1 Net Visualization and Shape

FHSim includes a module that visualizes the fish cage in 3D. The cage has the ability to react to environmental forces such as current and waves in simulation-time, however, this will be turned off for this thesis. The module has been modified such that the ROV can identify segments if they are within the ROV line of sight (LOS).

3.7.2 ROV Segment Identification

The net is divided into a number of segments, pre defined by the user. Each segment has four or three nodes corresponding to the edge of that segment. The cage is defined as a cylinder shaped wall and a bottom cone. By defining the centre of the net cage as origo in the cage frame of reference, it is possible to define the position of all segments in polar coordinates. All segments vertically aligned have the same polar angles. Figure 6 below illustrates the segmentation.

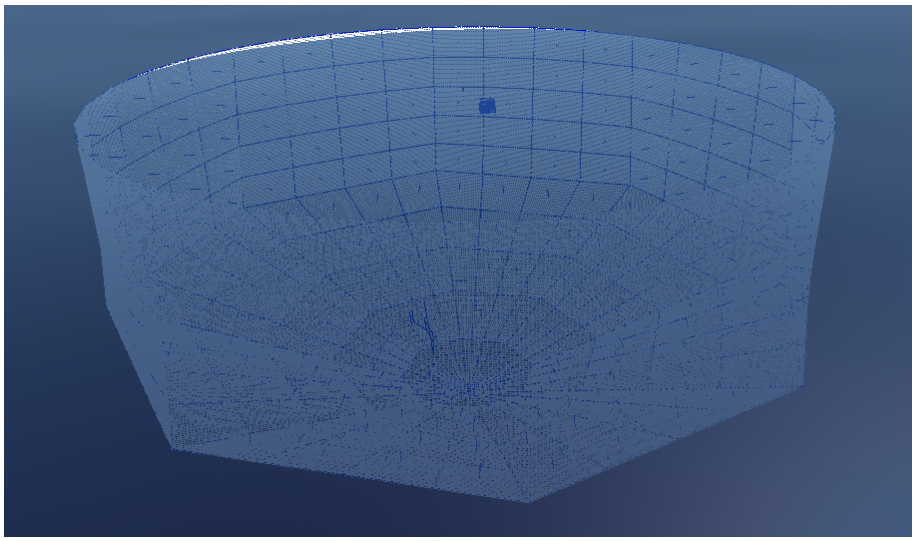

Figure 6: The net cage visualization with each segment defined as the square or triangle segmented using a blue line.

The visualization module is responsible of colouring the segments that have been within the ROV line of sight (LOS) green. The segments will also change position based on how they are perceived by the ROV. This has been pre-implemented for the general case in which the net shape is unknown and has to be identified by the ROV, however in this thesis the shape of the net is assumed to be known and constant. Hence at most, the segments will only change their heading such to face against the ROV. If a set of segments are in the ROV LOS, all of these will orient themselves toward the ROV's heading ψ, θ, and ϕ. The segment movement algorithm of this module is outside the scope of this thesis, however.

3.7.3 ROV Vision Field Simulation

In (Dukan, 2014), a thorough model of a DVL measurement tool is suggested. However, for this thesis the ROV vision field from the DVL is somewhat simplified. While a DVL uses acoustic beams to detect a surface to generate data, the DVL model in this implementation will be based on a horizontal and vertical vision field. The horizontal vision field of the ROV is simply defined as the circular arc of $\frac{\pi}{2}$, or more spesifically $\psi \pm \frac{\pi}{4}$ were ψ is the ROV heading. The vertical vision field is defined somewhat differently with constraints. This is mainly due to the shape of the net cage. Segments that are or have been within the horizontal and vertical vision field are regarded as identified by the ROV.

All the segments are defined in polar coordinates in the cage frame of reference, where the center of this frame is also the center of the cage. The translation between the NED and CAGE frame is a simple translation and rotation:

$$\begin{aligned} \boldsymbol{T}_c^n &= \boldsymbol{x}_o^n - \boldsymbol{x}_c^n = -\boldsymbol{x}_c^n \\ \boldsymbol{x}_{rov}^c &= \boldsymbol{x}_{rov}^n + \boldsymbol{T}_c^n = \boldsymbol{x}_{rov}^n - \boldsymbol{x}_c^n \end{aligned} \tag{52}$$

were $\boldsymbol{x}_o^n$ is NED origo, $\boldsymbol{x}_c^n$ is cage origo in the ned frame, and $\boldsymbol{x}_{rov}^{n/c}$ is the rov position in either ned or cage frame. The rotation between the two frames can be done using the rotation matrix defined in equation 5 page 9.

The position of the horizontal vision field in polar coordinates when the ROV is within the cage

can be found using this relation:

$$\begin{aligned} \theta^c_{\pm} &= \arctan 2(l_t, h_t) \\ l_t &= y^c + \sin\left(\psi^c \pm \frac{\pi}{4}\right) \\ h_t &= x^c + \cos\left(\psi^c \pm \frac{\pi}{4}\right) \end{aligned} \tag{53}$$

were ψ^c is ROV heading in the cage frame, x^c, y^c are the ROV position in the cage frame, and θ^c is the polar coordinate angle in the cage frame. Any segment that are within the polar coordinate angles θ^c_+ and θ^c_- defined by the horizontal vision field are potentially also within the vertical vision field. This is however a simplification and assumes the ROV is close to the net, and points toward it. Figure 7 illustrates the equation.

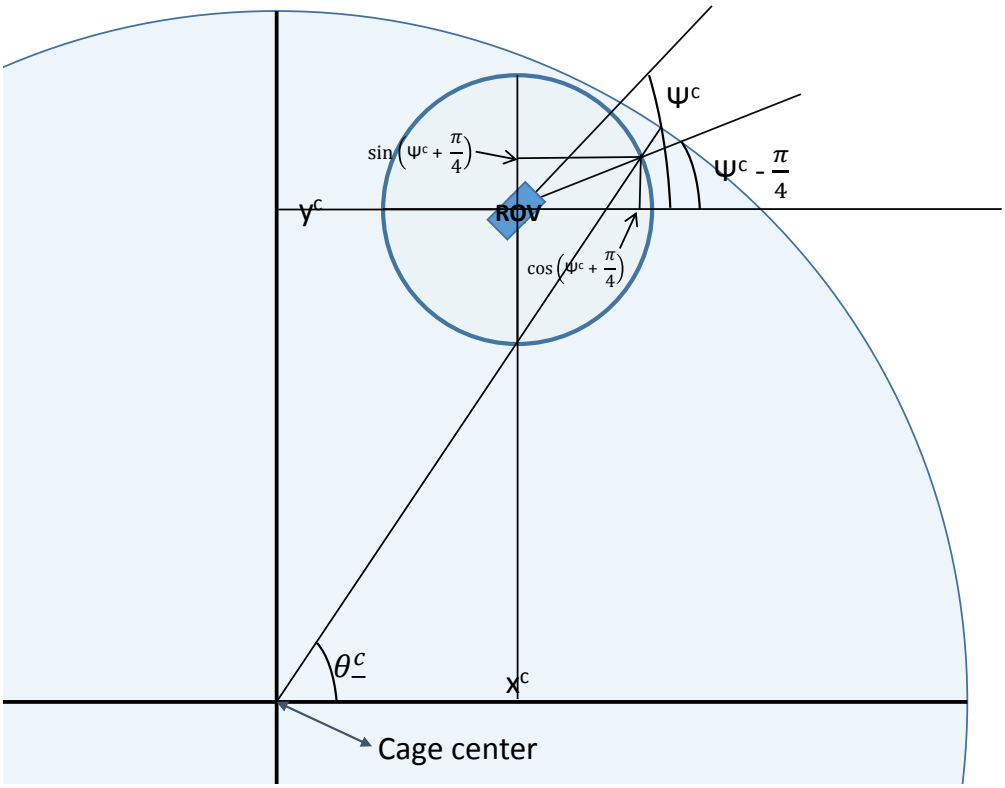

Figure 7: The geometrical position of the horizontal view field on the right side of the ROV. The largest blue circle represents the cage, with the circumference as the net edge.

The vertical vision field is defined using a constraint and a simplification of the ROV position within the cylinder and cone shaped cage. All segments have a defined length based on the total distance *along* the net from the segment origo to the ocean surface. This distance doesn't equal to the segment water depth, but instead its distance along the net vertically upwards. To find the vertical vision field, the ROV position is defined according to this vertical net length distance. This is only a valid position measure if the ROV is in close proximity to the net ($0-2$ meters, dependent on the ROV center of origin). ROV net vertical length $\mathcal{L}$ is approximated as:

$$\mathcal{L} \approx \sqrt{((r_{rov} - r_{net})^2 + z^2)} \tag{54}$$

were $r_{rov} - r_{net}$ is the point-plane distance from the ROV center of origin to a segment center of origin, and z is the ROV depth. All segments that are within $\mathcal{L} \pm 1$ and satisfy $0 < r_{rov} - r_{net} < 3$ are within the vertical line of sight.

When a set of segments are within the ROV vision field, they are given a new position and heading. The segments heading are made equal to the ROV heading in opposite direction $-\psi$, $-\theta$ and $-\phi$. The position is then changed such that the relative position between the segments remain the same, but their point-plane distance to the ROV changes according to the distance between the ROV and the net. Since the net position is assumed to be known beforehand in this thesis, the position of the segments will ideally not change. However since the ROV vision field is not modelled exact, the segment positions will change slightly. The heading might also be altered. The new heading of the segments, and the positional center of the segments (in LOS) are the simulated DVL measurements, and used by the waypoint system to determine the next waypoint. See figure 8 for an overview of how the DP system and visualization module cooperate.

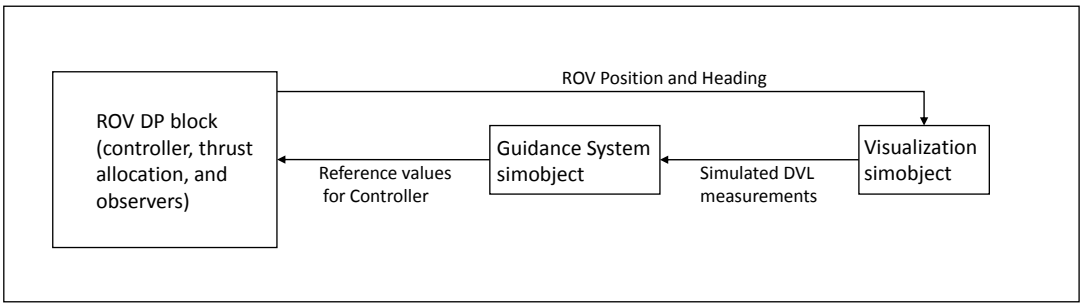

Figure 8: Communication block between the waypoint generating guidance system, DP system and visualization module.

3.7.4 Guidance for Autonomous Net Traversal

The guidance system is responsible for making the ROV traverse the entirety of the net. At first it was considered to design an entirely new guidance law similarly to (Dukan, 2014) for surface tracking. However, due to time constraints it was instead decided to utilize the already implemented waypoint navigation algorithm, and modify it for on-line waypoint generation. In (Hval, 2012), the waypoint system can automatically generate waypoints in a net cage using the known position of the segments. However, this algorithm assumes that the net shape is known in advance. This is generally not the case, hence the new waypoint algorithm is designed assuming an arbitrary net shape. The waypoints will be generated on-line as the ROV explores the cage.

3.7.5 Automatic Waypoint Generation for Net Traversing

For automatic waypoint generation the visualization and the waypoint generating module have to communicate, see figure 8. The traversing is separated into three distinct steps in order to structure the movement.

Step 1: The ROV has depth 2m, and traverses vertically down along the net to the cage bottom.

Step 2: The ROV has reached the cage bottom. Turn heading ψ, and move vertically upwards along the net (step 1 in reverse).

Step 3: The ROV has depth 2m and just finished step 2. The ROV must change heading ψ and its position correspondingly.

The steps are continually repeated from $\cdots 3 \rightarrow 1 \rightarrow 2 \rightarrow 3 \rightarrow 1 \cdots$.

The following notation will be used: ψ_s, θ_s, x_s, y_s and z_s are the heading, pitch and center of origin of the segment set in the ROV LOS. d is the point-plane distance from ROV center of origin to the segment set (desired distance to the net). ζ_d is a tuning parameter deciding how far away the next segment is located. This parameter will be dependent on the segment sizes. ζ_ψ is a tuning parameter deciding the extend the ROV turns heading. It is dependent on the ROV horizontal field of view and segment sizes.

Step 1, wp Generation:
In the first step, the waypoints are generated in such a way that the ROV moves vertically downwards *and* toward the cage center. The next waypoint is continually defined as:

$$\begin{aligned} x_{wp} &= x_s + \cos(\psi_s)d - \cos(\psi_d)\sin(\theta_s)\zeta_d \\ y_{wp} &= y_s + \sin(\psi_s)d - \sin(\psi_d)\sin(\theta_s)\zeta_d \\ z_{wp} &= z_s + \cos(\theta_s)\zeta_d \\ \psi_{wp} &= \psi_d \end{aligned} \tag{55}$$

When the ROV reaches within proximity of the cage bottom, the traversing algorithm switches to step 2 and a new ROV heading is defined: $\psi_d = \psi_d + \zeta_\psi$

Step 2, wp Generation:
The second step is the exact as step 1, but in the opposite direction; The next waypoint is continually defined as:

$$\begin{aligned} x_{wp} &= x_s + \cos(\psi_s)d + \cos(\psi_d)\sin(\theta_s)\zeta_d \\ y_{wp} &= y_s + \sin(\psi_s)d + \sin(\psi_d)\sin(\theta_s)\zeta_d \\ z_{wp} &= z_s - \cos(\theta_s)\zeta_d \\ \psi_{wp} &= \psi_d \end{aligned} \tag{56}$$

When the ROV reaches the cage top, the waypoint algorithm switches to step 3. The new heading defined is $\psi_d = \psi_d + \zeta_\psi$

Step 3, wp Generation:
In step 3, the ROV has to move sideways along the net while retaining a heading towards the cage. The ROV stops when its polar position angle is aligned with its new heading.

$$\begin{aligned} x_{wp} &= \cos(\psi_d)(r_{net} - d) \\ y_{wp} &= \sin(\psi_d)(r_{net} - d) \\ z_{wp} &= z_{wp} \\ \psi_{wp} &= \psi_d \end{aligned} \tag{57}$$

When the desired position has been reached, the algorithm repeats the entire process by returning to step 1.

Using this method the ROV is capable of automatically traversing the inside of the cage using a waypoint based algorithm. Figure 9 illustrates the various steps.

3.7.6 Remark on the Automatic Waypoint Generation Algorithm

It is not directly obvious from the equations, but the next desired ROV waypoint is positioned approximately a distance ζ_d from the ROV. It was found that for the algorithm to properly function, ζ_d has to be so large that the ROV ideally never reaches its desired waypoint before a new waypoint is generated due to that a new segment is identified by the ROV. Hence the waypoint is always out of reach for the ROV, but forces it to move toward the desired direction along the net surface.

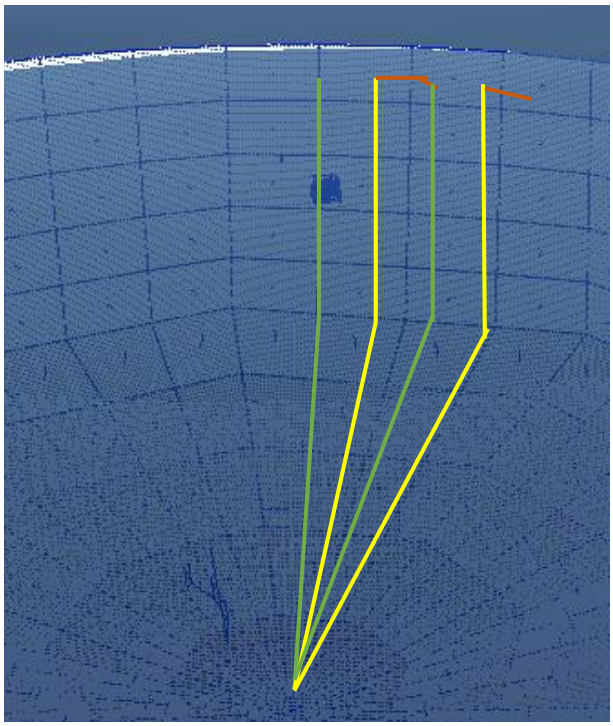

Figure 9: Illustration of ROV movement. Green indicate step 1, the rov moves vertically down, yellow indicates step 2, the rov moves vertically up, and red indicates step 3.

3.8 Overview of Programmed DP System Additions

Most of the programmed DP architecture in FHSim was setup in (Hval, 2012). In this thesis the programmed system was improved by correcting some program faults, and programming two new observers as separate C++ classes. This included a discrete extended kalman filter, and a current observer with wave filtering and injection terms consisting of position and velocity measurements. Modifications were also made to the previously implemented nonlinear observer to tackle velocity measurements in its wave filter, instead of position measurements.

The DP system was also programmed such that it could communicate with the visualization component of FHSim. The ROV was programmed such that when it travels inside a net it can identify sections of the net using its vision field. The DP guidance block was programmed such that when the visualisation component of the ROV identified a net segment, a new waypoint for the ROV was generated, such that the ROV can autonomously traverse the entire cage netting.

3.9 ROV Wave Responce

Wave Responce figures are used to identify the ROV response to wave forces. Some wave frequencies impacting the ROV will be highly damped out and cause no wave motion, while other frequencies will cause larger motions. The ROV was tested by making it float in the ocean freely under varying ocean waves conditions. The table below shows the data collected by simulations using short crested waves. The results of long crested waves are present in the appendix.

Table 2: ROV Wave Responce - ShortCrested Waves

ShortCrested Waves Significant Waveheight 0.5	Period 10	Period 5	Period 2
North Amplitude	0.09 m	0.06 m	0.013 m
East Amplitude	0.045 m	0.04 m	0.007 m
Depth Amplitude	0.04 m	0.028 m	0.09 m
Significant Waveheight 1.5 m	10 m	5	2
North Amplitude	0.26 m	0.18 m	0.04 m
East Amplitude	0.16 m	0.12 m	0.02 m
Depth Amplitude	0.15 m	0.1 m	0.02 m

The data from the table were normalized for each dimension for comparison purposes, see figure 10. As an example, for east dimension, the normalized ROV wave response amplitude was calculated as such:

$$\begin{aligned} n_{10} &= \frac{0.045}{0.045 + 0.04 + 0.007} \\ n_5 &= \frac{0.04}{0.045 + 0.04 + 0.007} \\ n_2 &= \frac{0.007}{0.045 + 0.04 + 0.007} \end{aligned} \tag{58}$$

were n_{10}, n_5 and n_2 are the normalized wave response amplitudes in east dimension for period 10, 5 and 2 respectively.

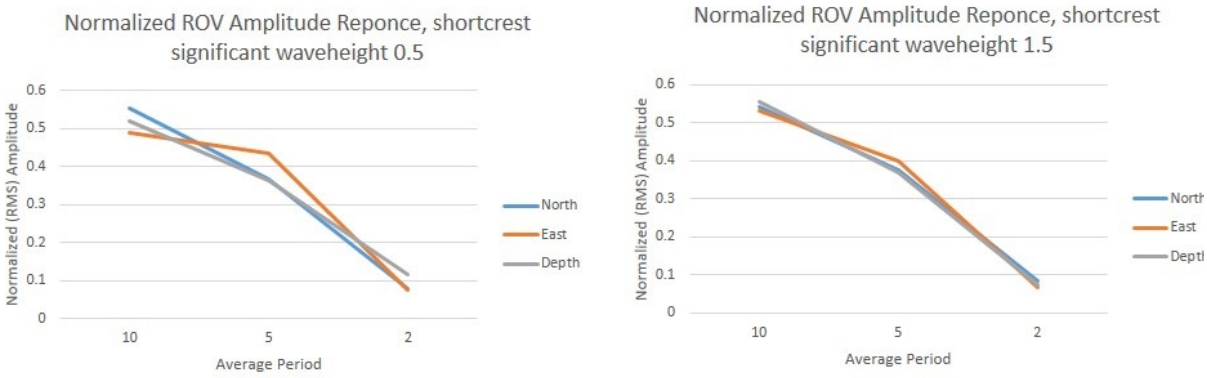

Figure 10: Normalized ROV Wave Responce Amplitude from 2

The ROV responds to wave forces equally in all dimensions relative to the period. The amplitude response is highest for larger ocean wave periods, and decreases for lower periods. The ROV

might have a resonant frequency between the ocean frequencies of 10 and 2, but more data is needed to confirm this. From table 2 it is seen that the ROV amplitude response in dimensions north and east for ocean period 2 has the same dimensions as measurement noise. Nonetheless, it is not excluded that high wave frequencies can induce low frequency motions on the ROV, especially when the ROV is moving. This means that the impact of waves of period 2 on the ROV are not neglected, and taken into consideration for some simulation scenarios.

3.10 DP Simulation Tests

The main objective of the simulations is to assess the DP performance. The controller and thruster allocation modules are assumed to be well functioning from previous implementations. Most focus will be on testing the different observer configurations and the autonomous net traversing algorithm from the guidance system.

When testing the observers, the main objectives are to find the performance differences between the nonlinear and EKF observers, and whether the addition of a current observer improves their performance or not. This means testing the estimation error, and wave filtering capabilities of the observers. A particular focus is set on verifying that the current observer behaves satisfactory. For each simulations the entire DP system is tested once per observer configuration. Hence for example, for a figure showing the performance of the nonlinear observer and EKF, it means that the ROV was simulated twice. Once using a DP system with the nonlinear observer, and a second time using the DP system with the EKF.

The four different observer configurations tested are:

Observer Configuration 1: EKF observer only. Discrete sample time is 0.1 seconds.

Observer Configuration 2: EKF observer with current observer. Discrete sample time is 0.1 seconds.

Observer Configuration 3: Nonlinear observer only.

Observer Configuration 4: Nonlinear observer with current observer.

In test 1, 4, and 5 all the configurations are tested, while in test 3 and 6 configuration 2 and 4 are tested. In test 2, configuration 2 is used. The tests used to asses the DP system are listed below:

Test 1, Observer Configurations Test:

This test is based on that the bias term in both the EKF and nonlinear observers are used to model the effect of current forces. It is therefore interesting to test the extent the tuning of this bias term has on the overall observer performance if a current observer is used in cascade with the main observer, or if the main observer is used alone. The ROV is tested using all four different configurations of the observer. The main goal is to identify whether the addition of a current observer improves the error estimates $\hat{\boldsymbol{\eta}} - \boldsymbol{\eta}$, and positional errors $\hat{\boldsymbol{\eta}} - \boldsymbol{\eta}_{real}$. Were $\boldsymbol{\eta}$ is the measurements, and $\boldsymbol{\eta}_{real}$ is the real ROV position.

The number of simulations amount to two sets of four runs in which the ROV traverses forward in the figure of a square close to the ocean surface under strong ocean currents of $0.5ms^{-1}$ coming from the north direction. The two simulation sets have different ocean conditions. In the first set, calm waves of significant wave height $0.5m$ are simulated. In the second set, moderate waves of significant wave height $1.5m$ are used. In both ocean conditions the ocean current has a speed of $0.5ms^{-1}$. The four runs of each set are simulated with differently tuned bias gains $\boldsymbol{K_{4\eta}}$ and $\boldsymbol{K_{4\nu}}$ for the nonlinear observer, and

$\boldsymbol{Q}$ for the EKF. The bias gains are equal for all three dimensions north, east and depth. The gains are categorized into the levels: *low bias*, *standard bias*, *high bias*, *highest bias*.

All the different observer configurations are given a certain score based on the final value of the L2 norm errors attained during a simulation run. When assessing the error estimates, the comparison is done for each configuration per bias setting. The best performing configuration is given the point 1, and the worst performance is given the point 4. In some cases where there is no difference in performance between two configurations, then the maximal point 4 is reduced to 3 (or 2 in the case if three or a pair of configurations have the same final value). Since two sets of simulations are done, the score given for each configuration is the average of the score from the two simulation cases.

When assessing the positional errors, then all the configurations over the span of all bias setting are compared. The best performing configuration is given the score 1, and the worst the score of 16. If two or more configurations have the same performance then the max score of 16 is reduced in the same way as described above. The scores of the two sets are not averaged for the positional errors, and instead presented as two separate tables.

Based on the accumulated results, the observer configurations with the high bias settings (with slight adjustments) are used for all the other tests.

Test 2, Current Observer Test:
The ROV is tested under two specific scenarios to establish how stable and responsive the current observer estimates the ocean current. The dead reckoning strategy outlined in section 3.3.4 is also tested. The two cases are:

CE1: ROV changes heading 90 degrees, dead reckoning occurs while heading is changed. This scenario is meant to confirm the ability of the ROV to estimate the correct current regardless of its heading, even if signal loss occurs. It was mentioned in section 3.3.4 page 24, that if signal loss occurs in both velocity and position measurements, then the estimated ocean current stops updating. The current has a speed of $0.5ms^{-1}$ coming from the direction $\psi = 0.7854rad$, with calm waves of significant wave height $0.1m$.

CE2: ROV changes altitude and the ocean has significant current variations along the ocean depth. This case is meant to illustrate the ability of the current estimator to adapt to changes of the current force. The current speed and direction alters between the depths. No waves are present.

It should be noted that the estimated current is also dependent on that the surge damping parameter in the model damping matrix $\boldsymbol{D}$ is correct. In most realistic circumstances there will be a deviation from the real value, and the estimated current will be slightly offset from the real value. The current observer is tuned to mimic such an offset.

Test 3, Four Simulation Cases
Compare the performance between the nonlinear observer and EKF in cascade with a current observer in a series of four simulation cases. These cases are designed to mimic basic DP requirements, but also operating conditions and scenarios the ROV is expected to encounter when traversing a net cage. The four tests are summed up in the list:

DP1: Simulation case 1 follows a simple standstill operation. The ROV holds a fixed position for an extended period of time. This test will represent a typical DP test that verifies the basic DP *hold position* demand. The ROV will under many circumstances have to keep a fixed position in order to repair or inspect the net of the cage. The ROV is simulated in three different ocean conditions. First case is close to the ocean surface with calm currents of speed $0.1ms^{-1}$ and calm waves of significant wave height

$0.5m$. The second case is also close to the surface but with high currents of speed $0.5ms^{-1}$ and moderate waves of significant wave height $1.5m$. The final case is done when the ROV is deeply submerged such that no wave affect it.

DP2: Simulation case 2 is made to simulate the ascent of the ROV. The ROV begins at a depth of 40 meters, and ascents to a depth of 2. This simulation is made to test how the DP system can tackle the changes in wave conditions as they increase. The ROV is simulated in two different ocean conditions. In both conditions the current is high ($0.5ms^{-1}$). The difference is whether the wave has a calm or moderate strength of significant wave height $0.5m$ and $1.5m$ respectively.

DP3: Simulation case 3 tests the ROV in circular movements with a heading outwards. The ROV will move in a circular arc with a heading tangential to its movement. This will simulate movement along the circumference of a circular fish farming cage, and is a highly relevant movement type if the ROV is to inspect the inside netting of the fish cage. The ROV is simulated in two different ocean conditions. Both are close to the ocean surface. The first case has the ocean conditions of calm current ($0.1ms^{-1}$) and calm waves ($0.5m$). The second case has ocean conditions of high current ($0.5ms^{-1}$) and moderate waves ($1.5m$).

DP4: Simulation case 4 tests the ROV movement in surge and sway. First the ROV moves a distance 10 meters surge, and then 10 meters in sway. The heading is hence kept constant. The ROV is simulated in three different ocean conditions. The first two are close to the ocean surface. The first case has the ocean conditions of high current ($0.5ms^{-1}$) and calm waves ($0.5m$). The second case has ocean conditions of high current and moderate waves ($1.5m$). The final case is simulated deeply submerged with no wave influence and high current.

Test 4, Dead Reckoning

Compare the performance between all different observer configurations in regards to dead reckoning. The main purpose of this test is to first examine how the addition of a current observer impacts dead reckoning, and compare it with regards to the nonlinear observer and the EKF.

The efficiency of dead reckoning is measured using the error between the estimated position in north/east and the *real* simulated position of the ROV. The test will involve that the ROV will move in surge, then sway and then heave three times after one another. During these three repetitive movements the ROV will experience different types of signal losses in the position and velocity sensors responsible for north, east, surge and sway dimensions.

The signal losses will occur in the following order:

Iteration1:

Signal loss in north and east position for 20 seconds
Signal loss in north and east position for 20 seconds
Signal loss in north and east position for 20 seconds
Signal loss in north and east position for 220 seconds

Iteration2:

Signal loss in surge and sway (velocity) for 20 seconds
Signal loss in surge and sway (velocity) for 20 seconds
Signal loss in surge and sway (velocity) for 20 seconds
Signal loss in surge and sway (velocity) for 220 seconds

Iteration3:

Signal loss in north, east, surge and sway for 20 seconds
Signal loss in north, east, surge and sway for 20 seconds
Signal loss in north, east, surge and sway for 20 seconds
Signal loss in north, east, surge and sway for 300 seconds

The first iteration occurs during the first 1200 seconds. The second iteration occurs from 1200 seconds till about 2200 seconds. The final iteration occurs from 2200 till 3200 seconds. The different signal losses occur at different times of simulation for the EKF and nonlinear observer. Different colour markings in the figures will indicate signal losses.

The test is repeated in two simulation runs of different seeds in calm current of $0.1ms^{-1}$ and high waves of significant wave height $1.5m$ of period 10 seconds.

Test 5, Model Errors

Compare the performance between all different observer configurations in regards to model errors in the CPM model (equation 17). The model parameters in the damping and mass matrices $\boldsymbol{D}(\boldsymbol{\nu}_r)$ and $\boldsymbol{M}_A + \boldsymbol{M}_{RB}$ of the DP model are changed by a certain percentage. This percentage hence represents the percentage model error of the DP system. A second error is added to the estimated velocity. It is expected that the measured velocity has a bias error that increases proportional as such:

$$\boldsymbol{\nu}_{measured} = \boldsymbol{\nu}_{real} * \epsilon \tag{59}$$

were ϵ is a gain error constant with a chosen value of 1.1.

The ROV moves with a fixed heading 30 metres surge, then 30 meters sway, then 12 metres heave. This is repeated a second time. The different error types tested are:

E0: No Error
There are no errors in the model parameters. There is a constant gain error in the measured velocity.

E1: +20% Error
All parameters are overestimated by 20%. There is a constant gain error in the measured velocity.

E2: -20% Error
All parameters are underestimated by 20%. There is a constant gain error in the measured velocity.

The ROV is simulated in high current of $0.5ms^{-1}$ and moderate waves of significant wave height $1.5m$ of period 10 seconds.

Test 6, Autonomous Net Traversal

Make the ROV traverse the net to imitate a real operating scenario. This is done using the nonlinear observer and EKF in cascade with a current observer. The autonomous traversal algorithm is used to make the ROV traverse the net, hence this test is also used to asses these algorithms. The ROV is simulated traversing half a cage. The test done in the ocean conditions of high current of $0.5ms^{-1}$ and moderate waves of significant wave height $1.5m$ of period 10 seconds.

For each of these tests the environmental conditions are changed considerably. A lot of simulations were performed with varying environmental settings. However only the most relevant results are presented in this thesis. The different environmental conditions were picked based on the expected operating conditions of the ROV, and for comparison purposes. The ROV is

expected to handle current speeds of up to 0.5 ms^{-1} and waves of significant wave height of up to 2m. As seen from section 4.1 this is consistent with what is measured, except for the current speed. The periods chosen also reflect well the measured wave periods in Rataran, except for period 2 which is rarely present. However for comparison purposes it was decided to include the wave period 2 in the simulations. It was also decided to compare the ROV's response to short and long crested waves. The results between long and short crested waves are, however, quite similar, and to spare the text from generally repetitive results, only simulations of short crested waves are examined. The different ocean states simulated are listed below:

Current Speed
High current, $|\nu_c| \approx 0.5ms^{-1}$
Calm current, $|\nu_c| \approx 0.1ms^{-1}$

Wave Height
Moderate waves, $H_s = 1.5m$
Calm waves, $H_s = 0.5m$
No waves, $H_s = 0m$

Wave State
Short crested waves
Long crested waves*

Wave Period
Period = $10sec$
Period = $5sec$
Period = $2sec$

Wave and Current Direction
From north to south

*The conclusive results were similar for short and long crested waves, it was therefore decided to not include long crested waves in the main text, they are instead found in the appendix.

The following measurement noise amplitudes were used:

Position Sensor
North = 0.5m
East = 0.5m
Depth = 0.5m
Yaw = 0.02m

Velocity Sensor
Surge = $0.01ms^{-1}$
Sway = $0.01ms^{-1}$
Heave = $0.01ms^{-1}$
Yaw Rate = $0.01ms^{-1}$

Two types of graphs are used to analyse the observers:

L2 Norm Error
The L2 Norm Error is the L2 Norm of the estimation error $\tilde{\boldsymbol{\eta}}$, or positional error $\hat{\boldsymbol{\eta}} - \boldsymbol{\eta}_{real}$, of the observer, calculated such (for estimation error): $\epsilon_L = \sum_{k=1}^{N} \tilde{\boldsymbol{\eta}}[k]^2$ The L2 Norm Error will show the accumulated error of the observer during the simulated run.

Frequency Spectrum of Signals This figure shows the relative magnitude of the fast fourier transform (FFT) of the simulated wave forces impacting the ROV, FFT of the observer estimated wave motion $\boldsymbol{\xi}_1$ in NED frame, and the JONSWAP spectrum. Note that the simulated wave forces impacting the ROV are not the same as the simulated ocean waves. Ideally the FFT of the simulated ROV wave forces should equal the JONSWAP spectrum. For a good wave estimator, the FFT of the estimated wave motions should equal the simulated wave forces. It is expected that the estimated wave forces do manage to identify the average wave frequency of the JONSWAP spectrum.

4 ROV Simulation Results and Data Collection

This first part of this section will outline the early data collection made before developing the test simulations for the DP system. The second part will examine the results of a series of simulations done to test the DP system described in section 3.10.

4.1 Ocean data analysis

To further understand the sea environment which might be relevant for the ROV. Data was collected from the aquaculture site Rataran from the period 1.Mai till 1.December and analysed to examine the ocean conditions in which the ROV might be working in. The wave data contain a segment of unrealistically high or obscure values and are therefore is separated into two parts. The first part before the faulty readings, and the second after. The current measurements are not faulty however.

4.1.1 Ocean Current data

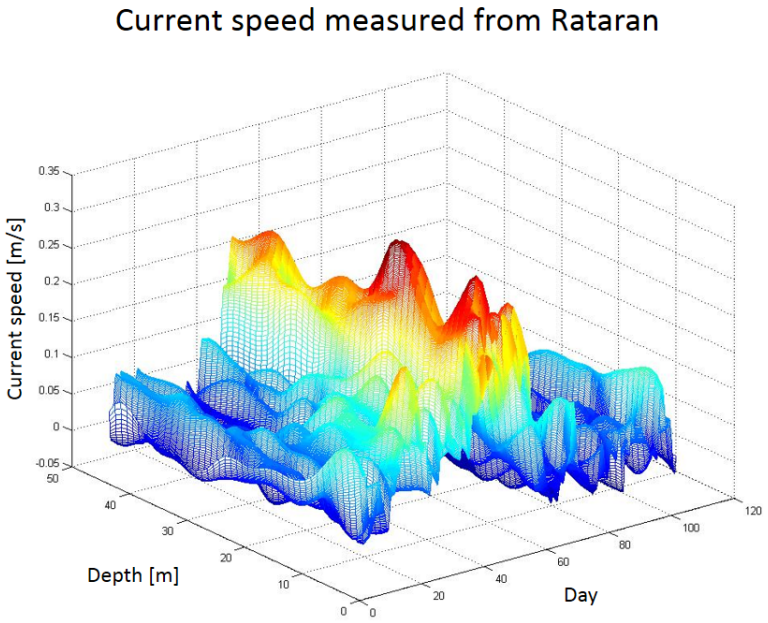

Figure 11: Current speed as measured on aquaculture location Rataran during the period 1.Mai till 1.December.

The current speed on this particular location from figure 11 indicates that the current speed is quite low until it quite abruptly reaches $0.25ms^{-1}$. The overall current speed measured in figure 11 are quite low based on what is the expected ROV operating conditions. Some locations were suggested to have speeds of $0.5ms^{-1}$. Thus the ocean current conditions used in the simulations are based on the expected operating conditions of the ROV rather than the measured current speed in Rataran.

4.1.2 Wave Significant Height Data

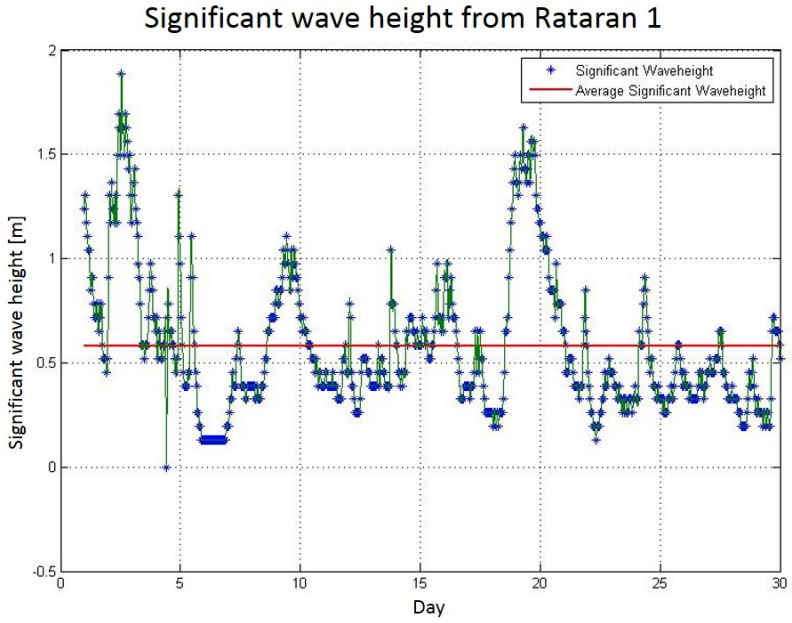

Figure 12: Significant wave height as measured on aquaculture location Rataran during the period 1.Mai till 1.December.

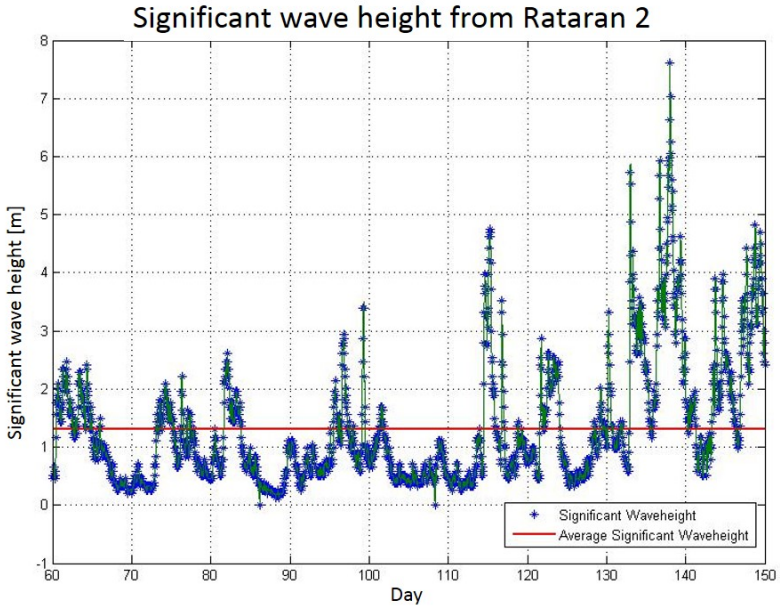

Figure 13: Significant wave height as measured on aquaculture location Rataran during the period 1.Mai till 1.December.

The significant wave height from figure 12 and 13 are not the same. The increased wave height spikes are slightly larger in figure 13. This might be due to statistical reasons rather than seasonal however. An often occurring significant wave height is about $0.5m$ when the waves are at their calmer state. The most common spikes have a max significant wave height of about $1.5 - 2m$. The ROV is expected to handle significant wave height of about 2 meters, which is measured several times. A particular high spike occurring at around day 135-140 is the result of the storm *Hilde* at the measured location, see (Norwegian Meteorological Institute, 2013).

4.1.3 Wave Period Data

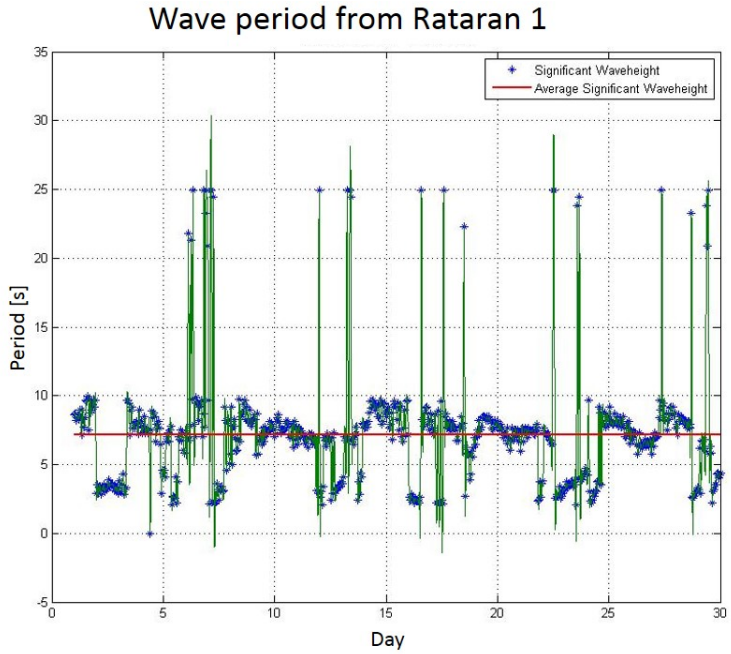

Figure 14: Wave period from the most energetic wave as measured on aquaculture location Rataran during the period 1.Mai till 1.December.

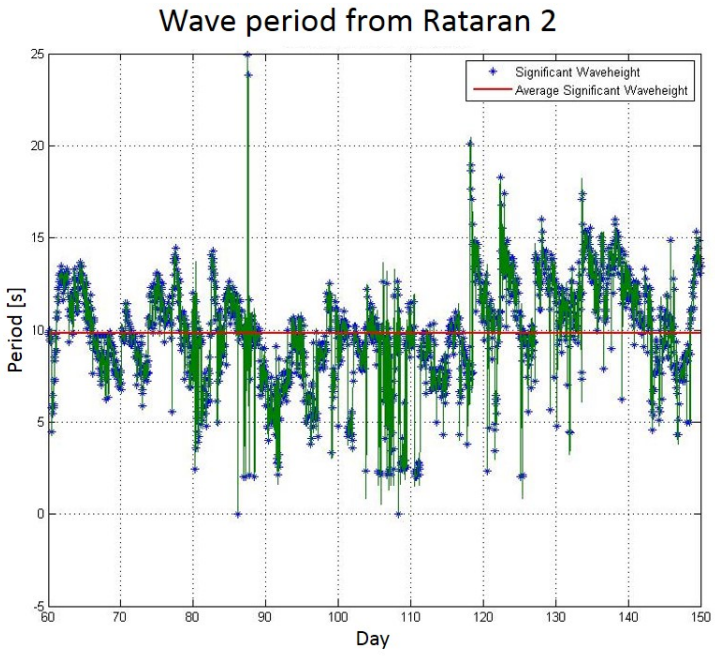

Figure 15: Wave period from the most energetic wave as measured on aquaculture location Rataran during the period 1.Mai till 1.December.

The average wave period is about 10 ± 5 seconds. Just as with the significant wave height, the measurements are different from figure 14 and 15. The average period is larger in figure 15 due to higher periods in the days of 120-140. The high and extraordinarily sharp peaks of the period data are treated as wild-points.

It can be concluded that based on the measurements from this location that the expected operating ocean conditions of the ROV are mainly waves of significant wave height ranging from 0.5 till 2 metres, with a period between 5 and 10 seconds. The ocean current speed ranges from 0.05 ms^{-1} to 0.25 ms^{-1}.

4.2 Test 2, Current Observer Test

CE1:

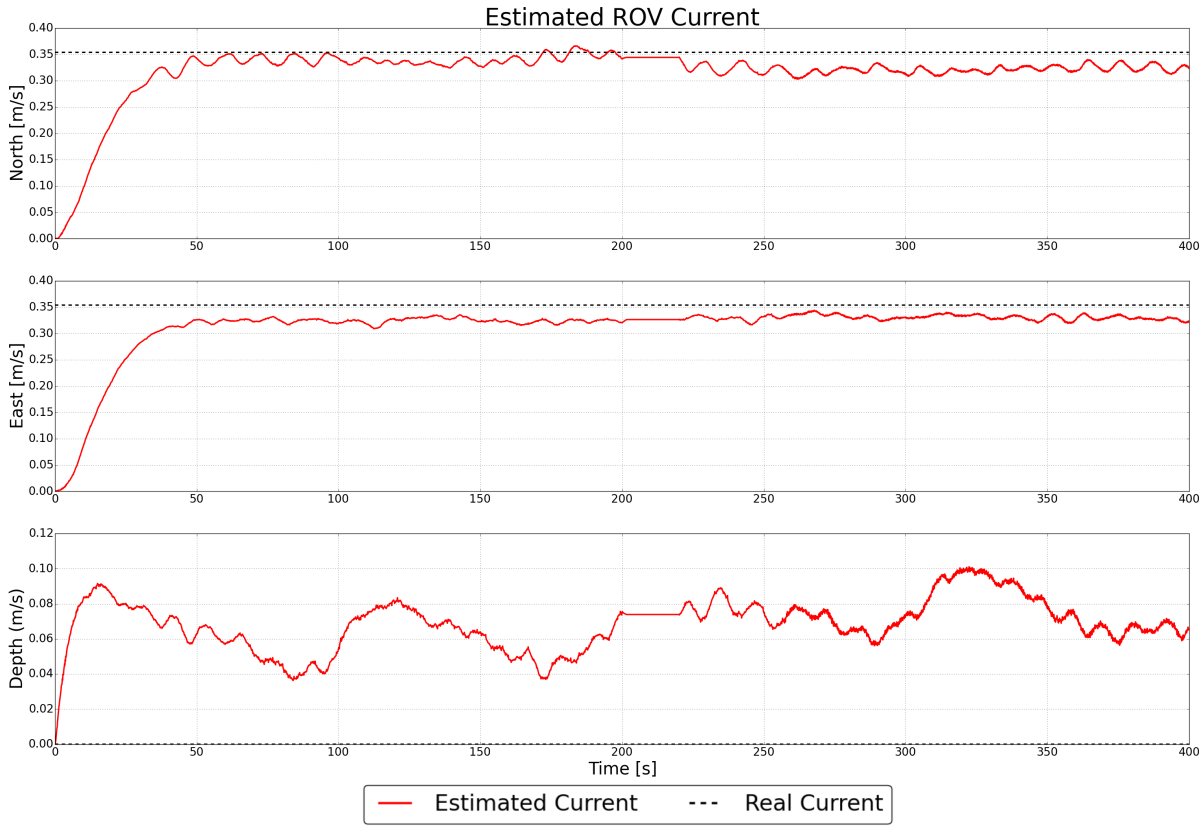

(a) Estimated ocean current. Dead reckoning occurs between the timespan about 200 - 220 seconds.

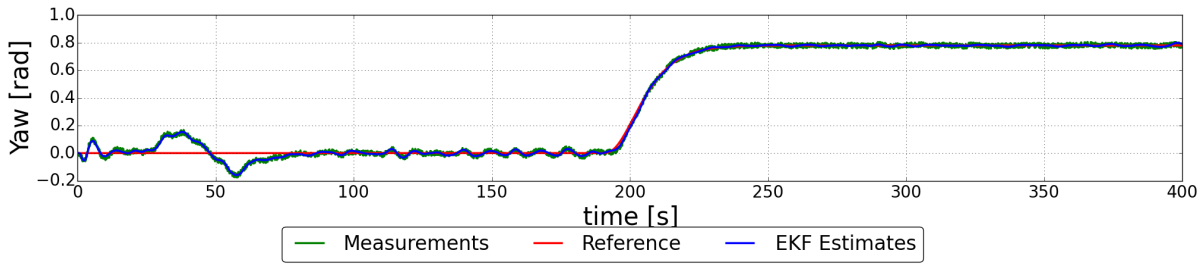

(b) Estimated heading from the EKF in cascade with the current observer.

Figure 16: ROV estimates during Case 1. Calm waves.

The observer settling time is about 190 seconds, just after that the ROV changes heading, and some seconds later it losses all its signals in surge, sway, north and east. Signals are lost between the timespan of about 200-220 seconds. The ROV successfully manages to keep a constant current estimate even if the ROV has changed its heading 90 degrees during the incident. There are no disrupting spikes that occur after the signals are regained in the current observer. The

estimated current is, however, slightly decreased in the north dimension after the signal loss.

CE2:

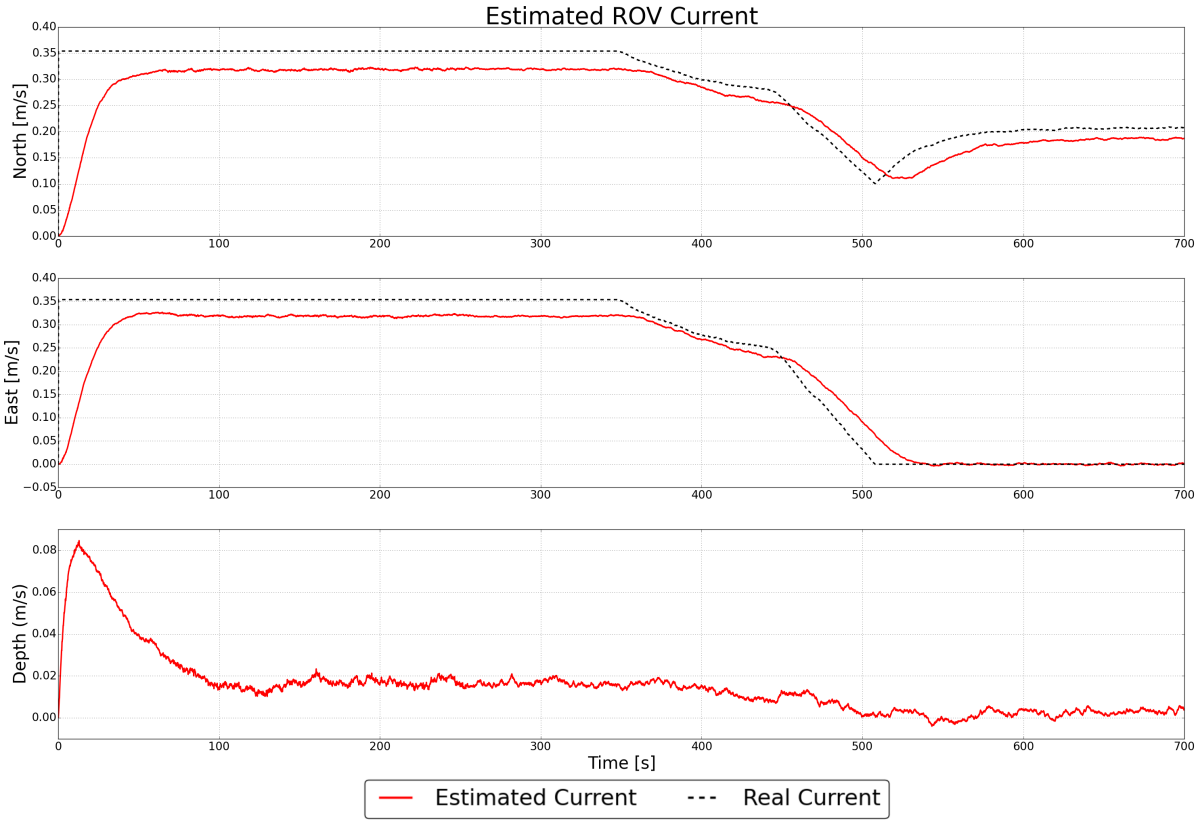

(a) Estimated ocean current.

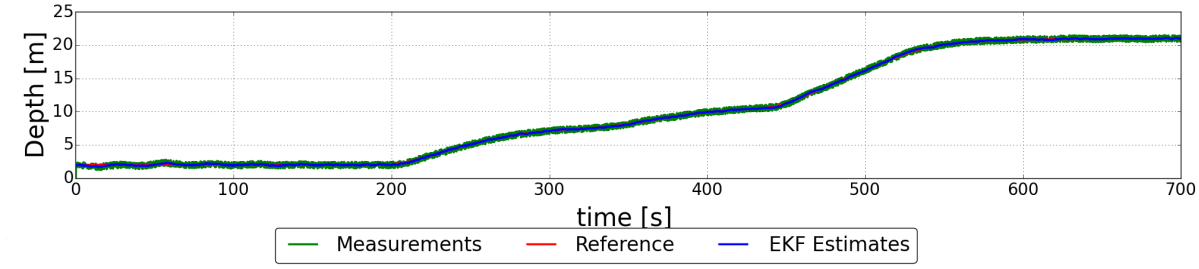

(b) Estimated depth from the EKF in cascade with the current observer.

Figure 17: ROV estimates during Case 2. No waves.

This particular case shows that the estimated ocean current is changing in accordance with the varying current speed and direction along the ocean depth. It is stable throughout the simulation.

4.3 Observer Performance and Estimation Errors Results

This section outlines the performance of different observer configurations based on their estimation errors and positional errors. The observers are assessed based on the accumulated error using the L2 norm error.

4.3.1 Test 1, Observer Configurations Test

Table 3: Results of the Observer Configuration Test For Estimated Error $\hat{\boldsymbol{\eta}} - \boldsymbol{\eta}$. Comparisons are done between each observer configurations for each bias setting separately (highest, high, standard, low). Best score is 1, worst attainable is 4. (Score is averaged from the results of two simulations, see section 3.10)

Highest Bias Score	Depth L2 Error Score	East L2 Error Score	North L2 Error Score	Total L2 Error Score
EKF w/ Current Observer	1	1	1.5	3.5
EKF	1.5	1	1	3.5
Nonlinear w/ Current Observer	1	2	2.5	5.5
Nonliner	1.5	1	3.5	6
High Bias Score				
EKF w/ Current Observer	1	1	1	3
EKF	1.5	1	1	3.5
Nonlinear w/ Current Observer	1	2	1.5	4.5
Nonliner	2	1	2	5
Standard Bias Score				
EKF w/ Current Observer	1	1	1	3
EKF	2.5	1	2	5.5
Nonlinear w/ Current Observer	1.5	3	1	5.5
Nonliner	3	2	2.5	7.5
Low Bias Score				
EKF w/ Current Observer	1	1	1.5	3.5
EKF	1.5	1	2.5	5
Nonlinear w/ Current Observer	1.5	3	1	5.5
Nonliner	1.5	2	3.5	7

As seen in the above table, for all different bias levels (highest, high, standard and low), it is the DP system with a current estimator that score best. The best configuration is the EKF with current observer, and the worst is the nonlinear without current observer. The EKF configurations continually score better than the nonlinear observers. The EKF observer without a current observer score better than the nonlinear observer *with* current observer.

It should be noted that the best (minimal) L2 Norm error in all simulations was never surpassed by any particular observer configuration. In many cases several observers shared the same best L2 Norm error, and not one of the observers was capable of attaining a lower L2 Norm error than what other observers could.

Table 4: Results of the Observer Configuration Test For ROV Position Error $\hat{\boldsymbol{\eta}} - \boldsymbol{\eta}_{real}$ under moderate waves of significant wave height $1.5m$. Comparisons are done between each observer configurations between all bias settings. Best score is 1, worst attainable is 16.

Highest Bias Score	Depth L2 Error Score	East L2 Error Score	North L2 Error Score	Total L2 Error Score
EKF w/ Current Observer	4	5	8	17
EKF	4	8	11	23
Nonlinear w/ Current Observer	4	5	2	11
Nonliner	4	2	1	7
High Bias Score				
EKF w/ Current Observer	3	9	7	19
EKF	5	6	9	20
Nonlinear w/ Current Observer	1	4	4	9
Nonliner	5	1	3	9
Standard Bias Score				
EKF w/ Current Observer	2	10	7	19
EKF	5	7	10	22
Nonlinear w/ Current Observer	1	4	6	11
Nonliner	5	3	8	16
Low Bias Score				
EKF w/ Current Observer	1	14	5	20
EKF	6	13	13	32
Nonlinear w/ Current Observer	1	3	8	12
Nonliner	6	3	12	21

In the simulation cases of moderate waves, it appears that the nonlinaer observers have considerable better performance than the EKF variants. This is especially true for the highest, high and standard bias cases.

The addition of a current observer only improves the nonlinear observer under the standard and low bias settings. In the high setting, there's no difference whether the nonlinaer observer has current estimation or not. The best performance of the nonlinear observer comes in the highest bias setting without a current estimate.

The EKF observer always benefits having a current estimate. The best performance of the EKF occurs in the highest bias setting with a current estimate.

The second best performances occur during the high bias setting. It would seem that in this case the addition of a current observer neither particularly improves or worsens the performance of the DP system.

Table 5: Results of the Observer Configuration Test For ROV Position Error $\tilde{\boldsymbol{y}} - \boldsymbol{y}_{real}$ under calm waves of significant wave height $0.5m$. Comparisons are done between each observer configurations between all bias settings.

Highest Bias Score	Depth L2 Error Score	East L2 Error Score	North L2 Error Score	Total L2 Error Score
EKF w/ Current Observer	3	7	7	13
EKF	5	4.5	10	19.5
Nonlinear w/ Current Observer	5	6	1	12
Nonliner	4	2	2	8
High Bias Score				
EKF w/ Current Observer	2	7	6	15
EKF	7	5	8	20
Nonlinear w/ Current Observer	2	4	2	8
Nonliner	5	1	5	11
Standard Bias Score				
EKF w/ Current Observer	1	9	4	14
EKF	5	8	10	23
Nonlinear w/ Current Observer	2	4	3	9
Nonliner	5	3	9	17
Low Bias Score				
EKF w/ Current Observer	2	11	4	17
EKF	5	10	12	27
Nonlinear w/ Current Observer	1	4	4	9
Nonliner	4	3	11	18

In the simulation cases of calm waves it appears that the best score of 8 is achieved by the nonlinaer observer with and without a current estimate at different bias setting. In the highest bias setting, the nonlinear observer performs better without a current observer. In the high bias setting, the addition of a current observer improves the nonlinear observer. Further, the nonlinear observer with a current estimate is quite superior in performance in the standard and low bias settings.

For the EKF, just as with moderate waves, the addition of a current observer improves the performance in all bias cases. The best performance occurs in the highest bias setting.

Based on both tables 5 and 4, it suggests that the DP system generally has best performance when its observers are tuned to the higher bias settings for calm and moderate waves when the ROV is moving in a square. However, the tests were only done for a particular ROV scenario. The addition of a current observer makes the DP system more robust when tuning the bias, as can be seen, its score varies a lot less at the different bias setting.

It can be seen that the scores of the high bias setting are almost as good as for the highest setting, but in general, more tests need to be done to test the difference of using the high or highest bias settings. The high bias gains of the observers were tuned slightly more after this test, and then used as the gains for the observers of all the other tests performed.

4.3.2 Test 6, Autonomous Net Traversal

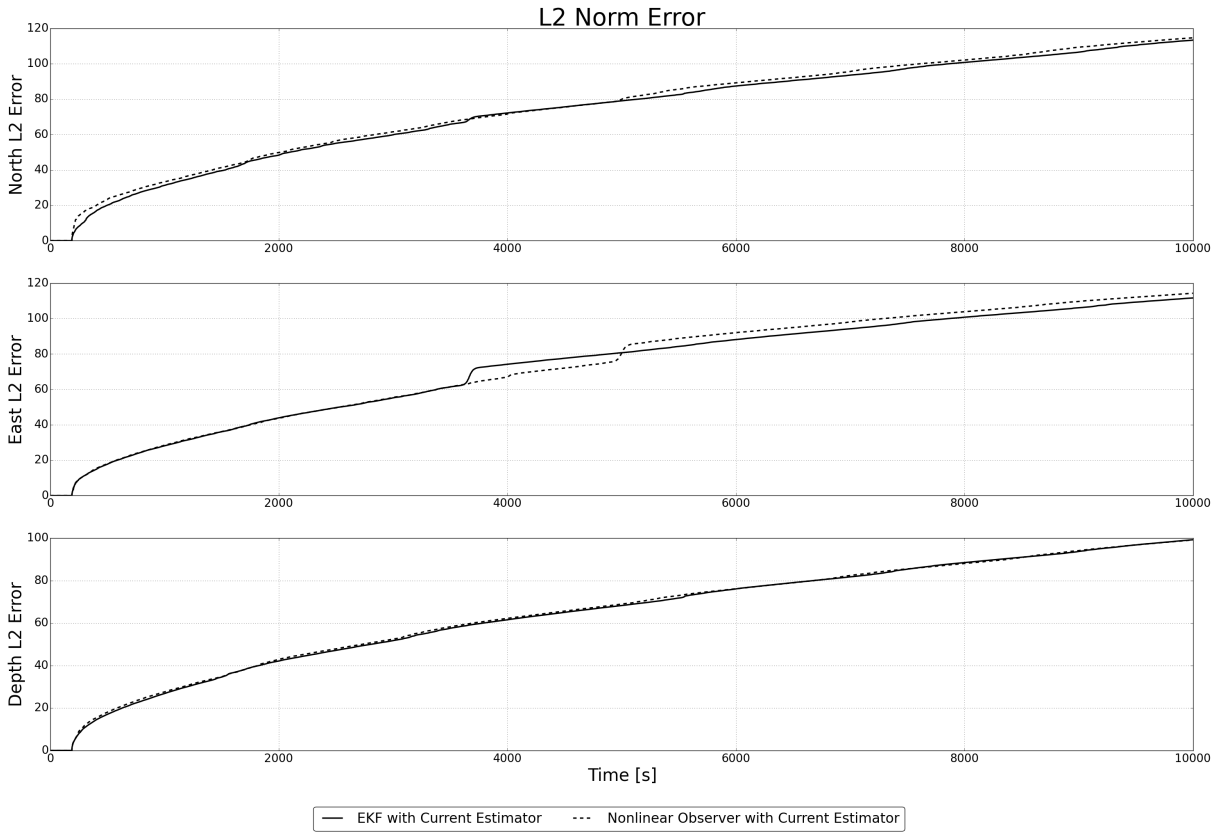

Figure 18: ROV L2 norm error when traversing the net.

It is seen from figure 18 that the total accumulated norm error is the same. It is also seen that both DP systems have a jump in the L2 norm error, occurring at about the 3800 second mark for the EKF observer, and 5000 mark for the nonlinaer observer.

4.3.3 Test 3, Four Simulation Cases

DP1:

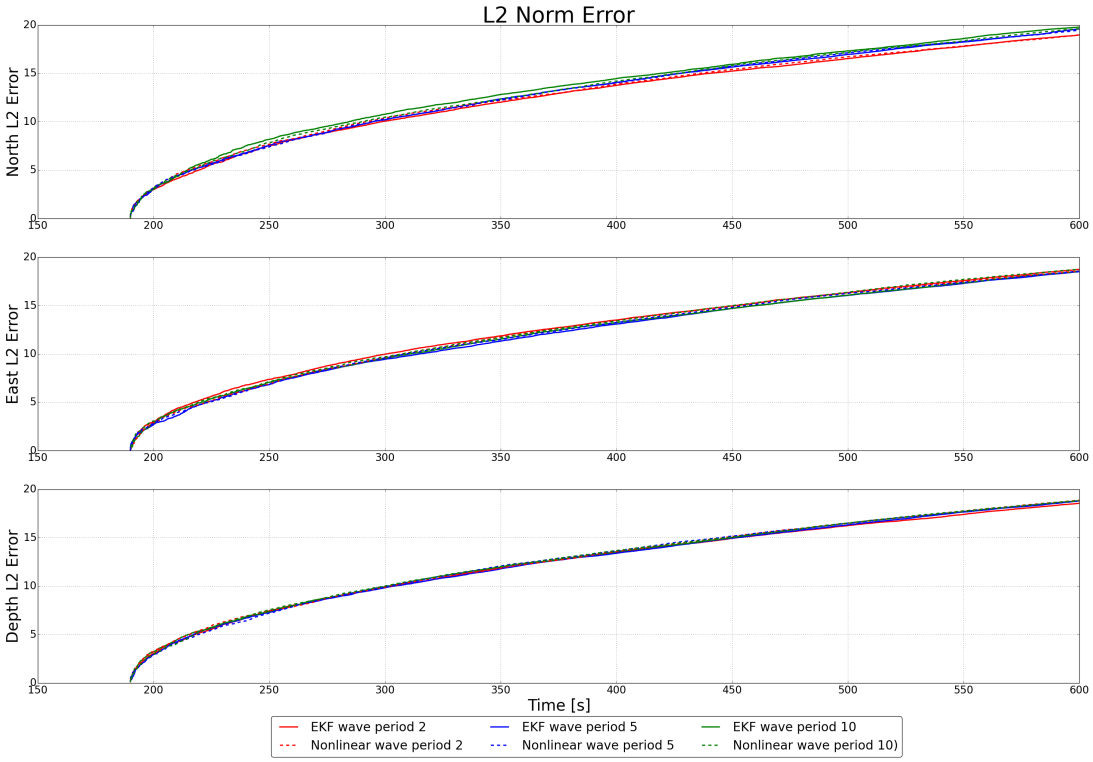

(a) Simulated at depth 2 meters, calm current and calm short crested waves.

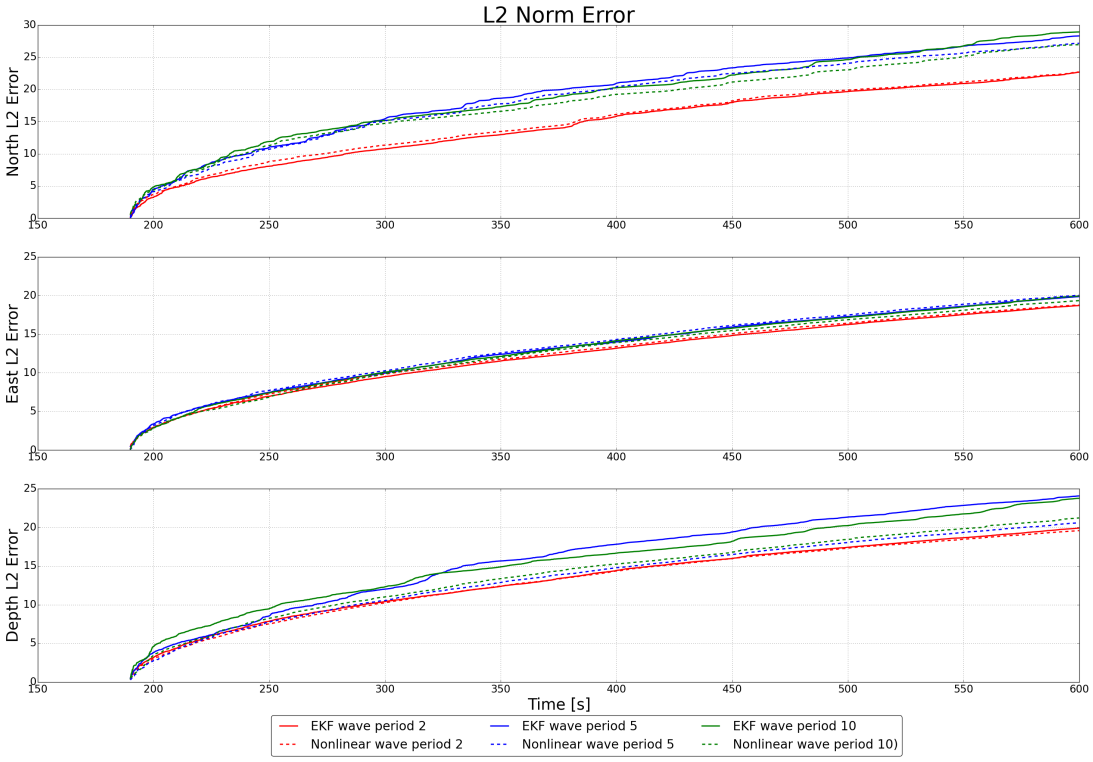

(b) Simulated depth 2 meters, high current and moderate short crested waves.

Figure 19: L2 norm error for the ROV when holding a fixed position.

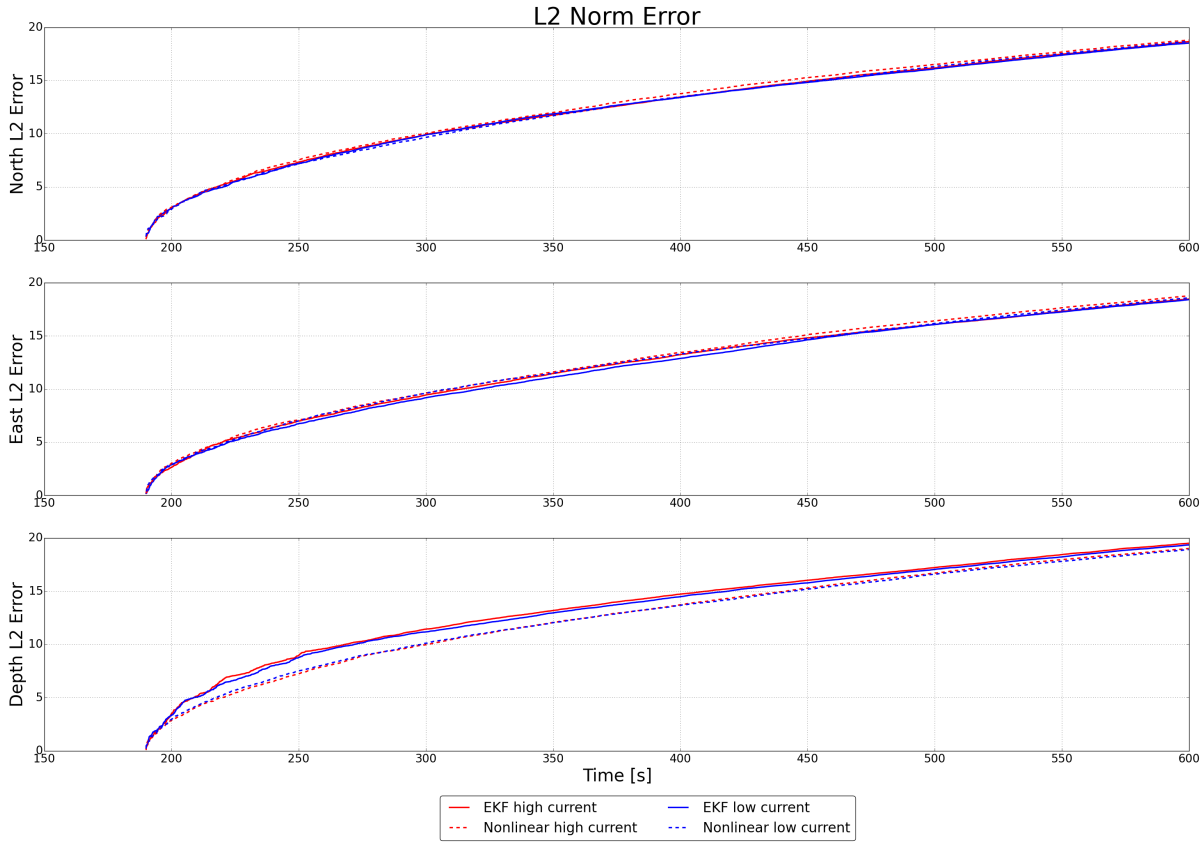

Figure 20: L2 norm error for the ROV when holding a fixed position when simulated at depth 40 meters, and no waves.

DP2:

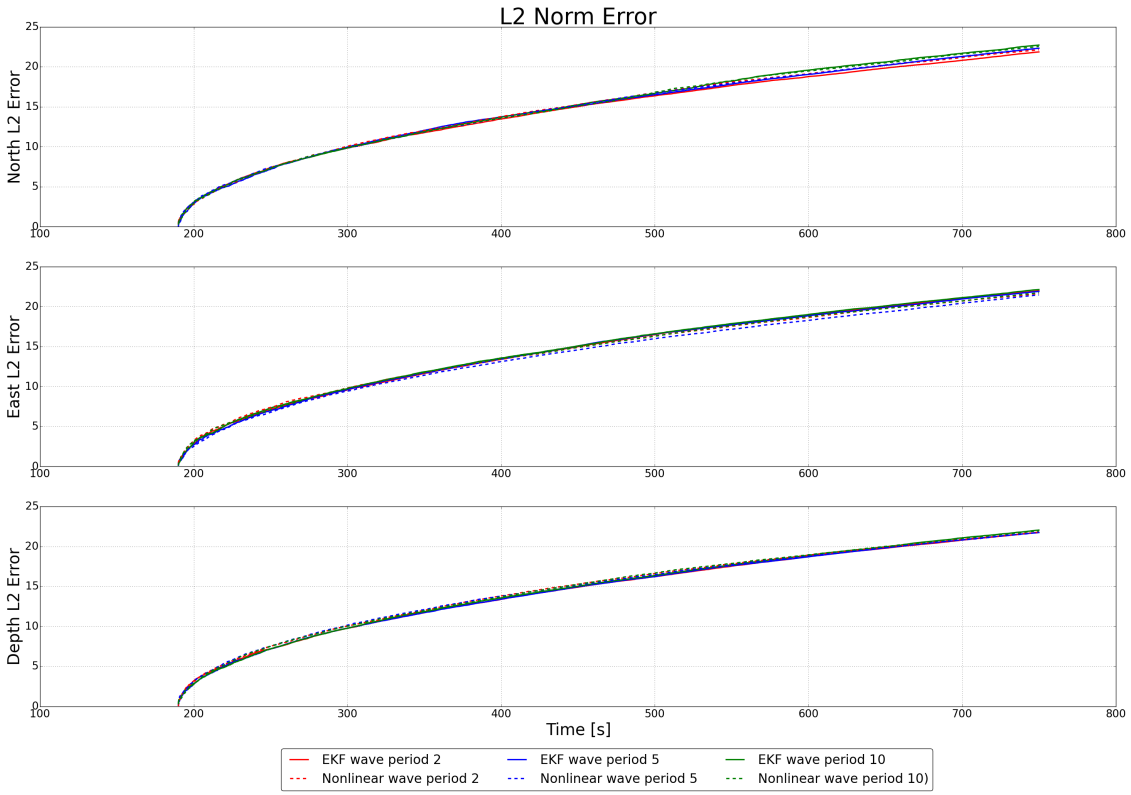

(a) Simulated at depth 2-40 meters, high current and calm short crested waves.

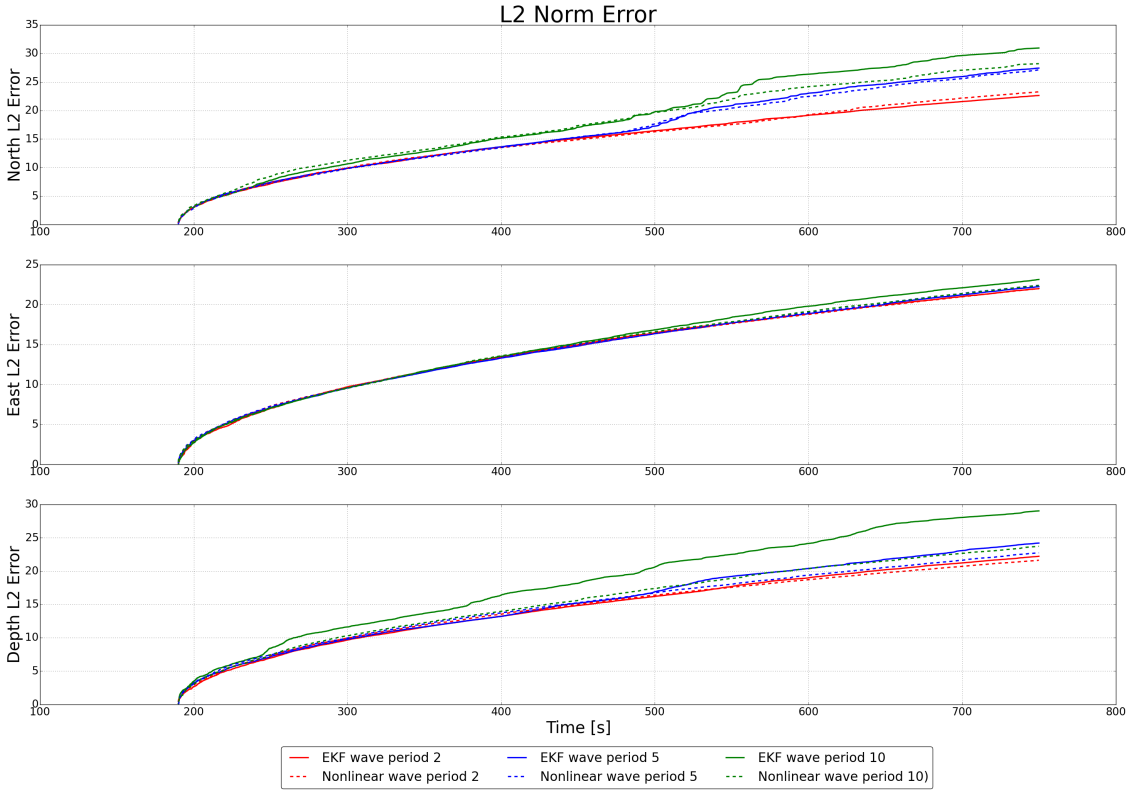

(b) Simulated at depth 2-40 meters, high current and moderate short crested waves.

Figure 21: L2 norm error for the ROV when ascending from 40 to 2 meters.

DP3:

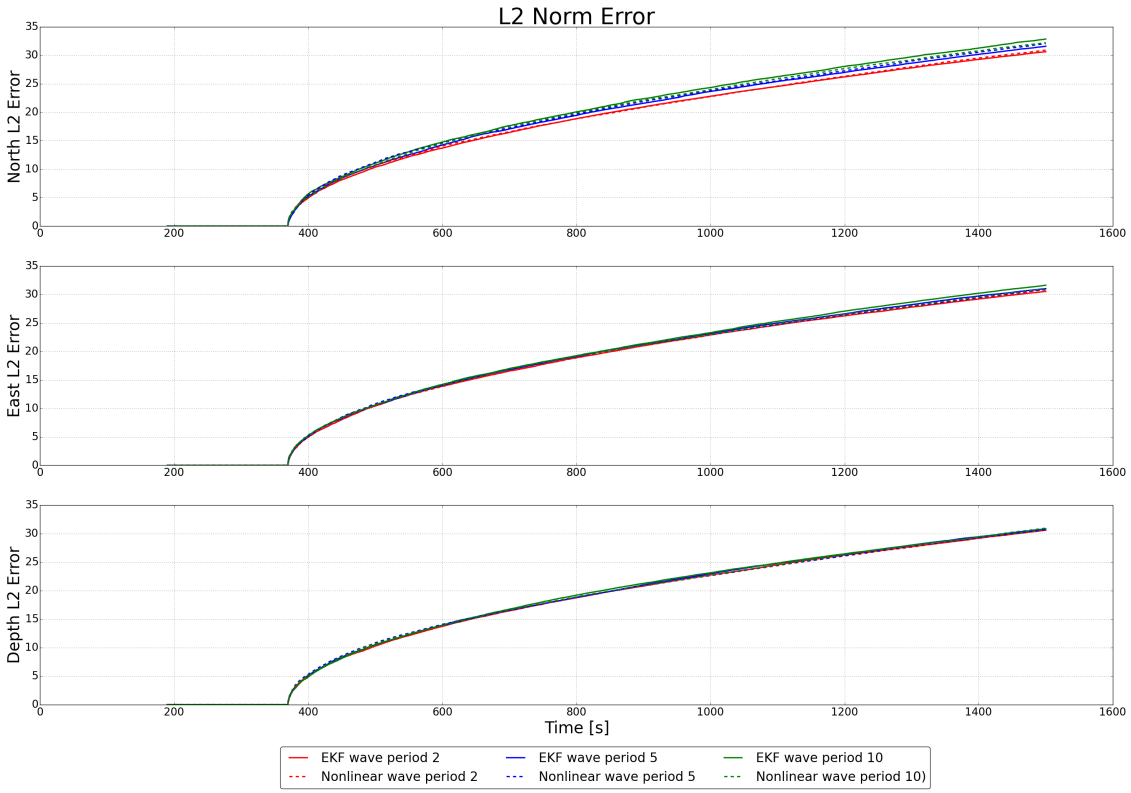

(a) Simulated at depth 2 meters, calm current and calm short crested waves.

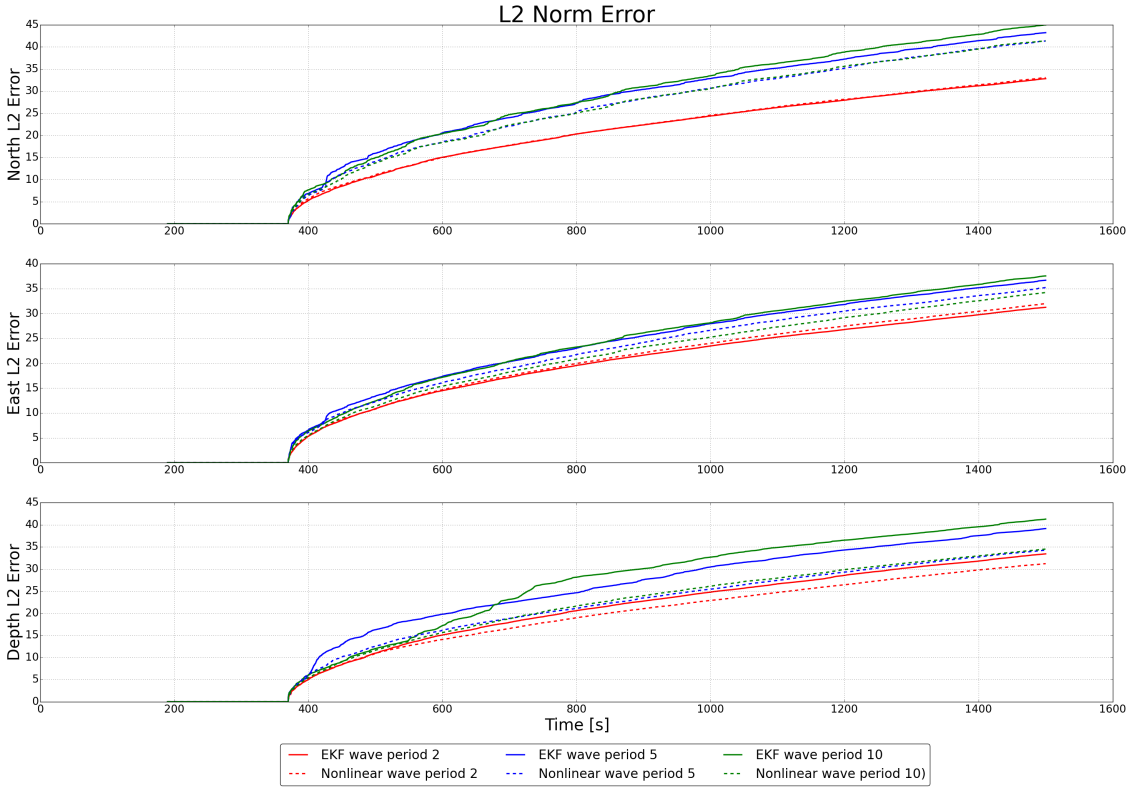

(b) Simulated at depth 2 meters, high current and moderate short crested waves.

Figure 22: L2 norm error for the ROV when moving in a circular path.

DP4:

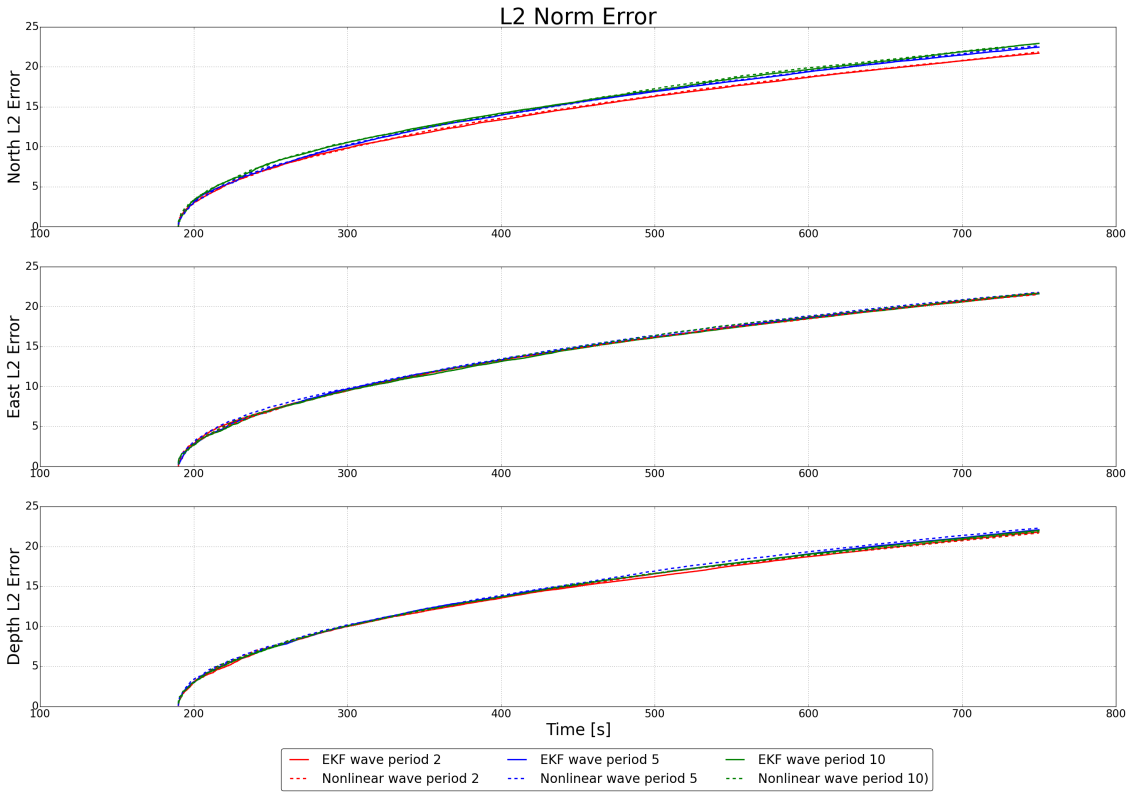

(a) Simulated at depth 2, high current and calm short crested waves.

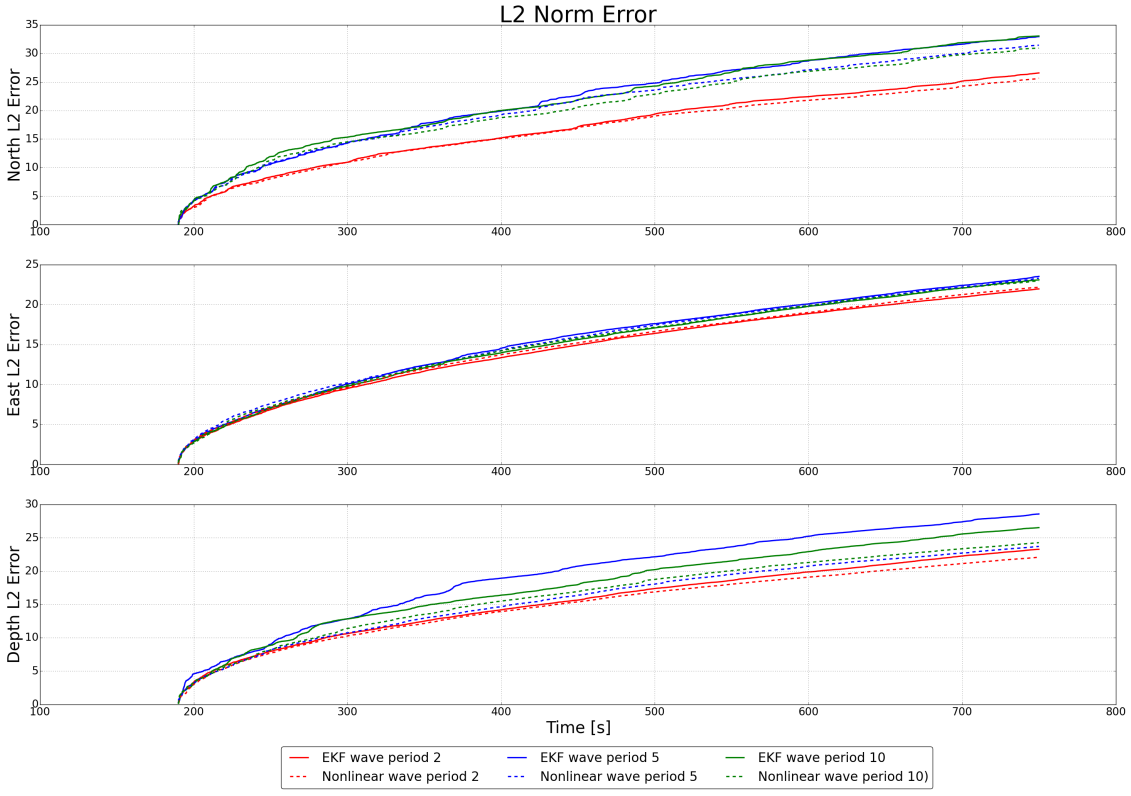

(b) Simulated at depth 2 meters, high current and moderate short crested waves.

Figure 23: L2 norm error for the ROV when moving in surge and sway.

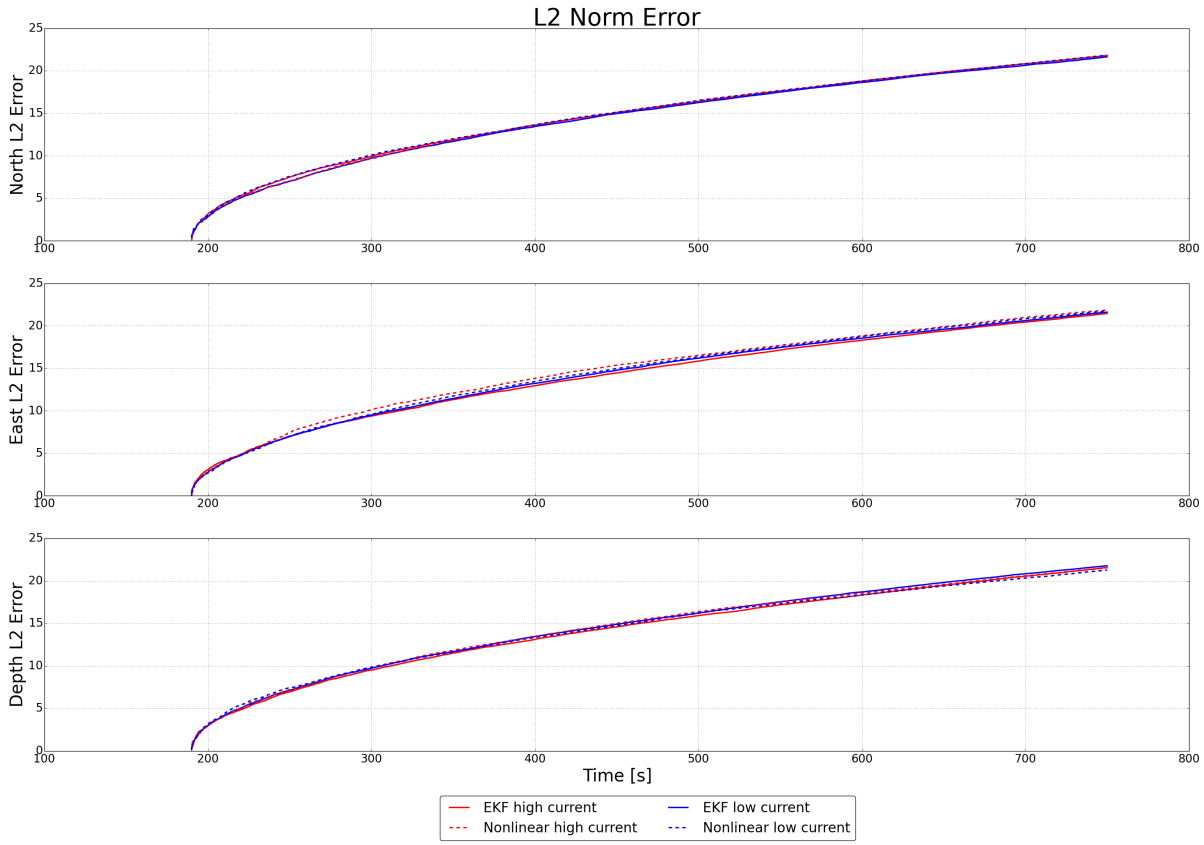

Figure 24: L2 norm error figures when moving in surge and sway. Simulated at depth 40 meters, high and low current and no waves.

4.3.4 Test 3 Summary

Based on the results of all cases it can be seen that the L2 error norm is mainly dependent on two conditions. The wave conditions, and how the ROV moves.

In cases where the ROV is not influenced by waves, see figures 24, 20 it appears that all the observers have a similar performance. There are sometimes small differences but these are minute.

In the cases were the ROV is influenced by calm waves, see figures 23a, 22a, 21a and 19a, the ROV observers also give quite similar performances, with the exception of the north dimension in which the performance worsens slightly for higher wave periods.

In cases where the waves are of moderate size, see figures 23b, 22b, 21b and 19b then the ROV observers perform very similar for waves of period 2, but change substantially for moderate waves of periods 5 and 10, see figures 23b,22b,21b and 19b. In particularly figure 21b, the wave forces gradually increase as the ROV ascents, and so does the estimated error rate. In cases of moderate ocean waves, it is the nonlinear observer that comes out better than the EKF.

The L2 error norms are slightly increased when the ROV is moving in circular paths with a heading tangential to its movement as in simulation case DP3.

For all figures the errors in each dimension are also different. The errors in the east dimension is the least affected by different wave periods, while the north dimension is most. The nonlinear observers perform considerably better than the EKF in the depth dimension.

4.3.5 Test 5, Model Error

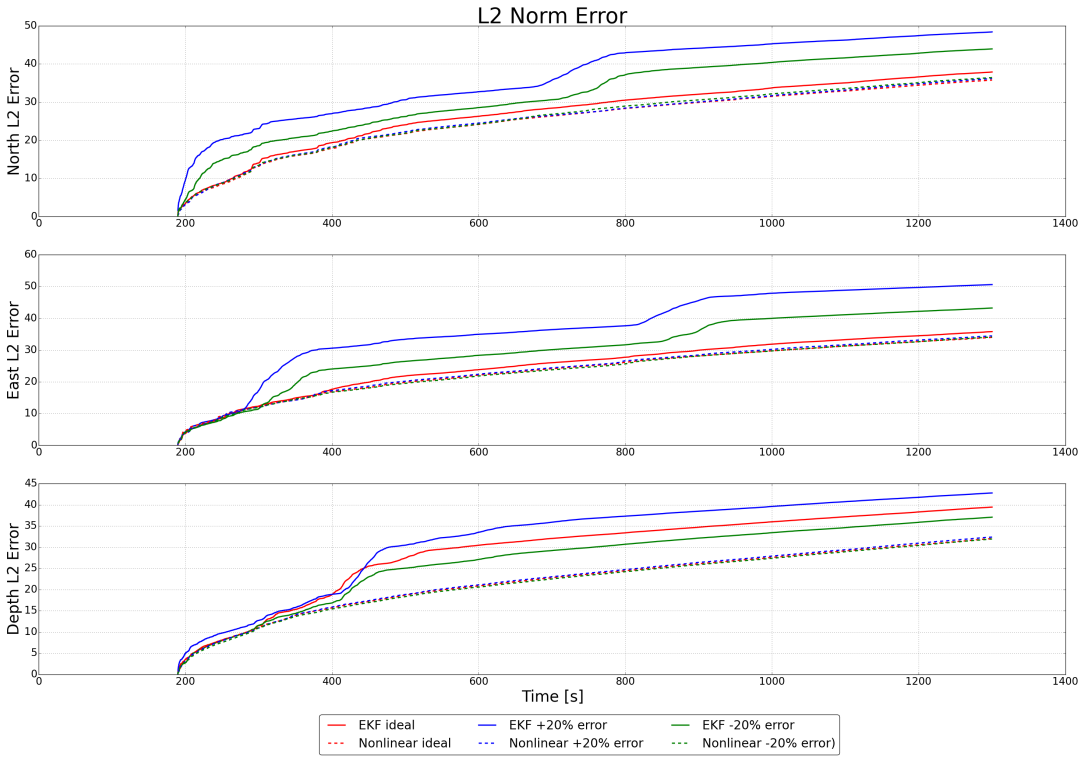

(a) DP system with current observer.

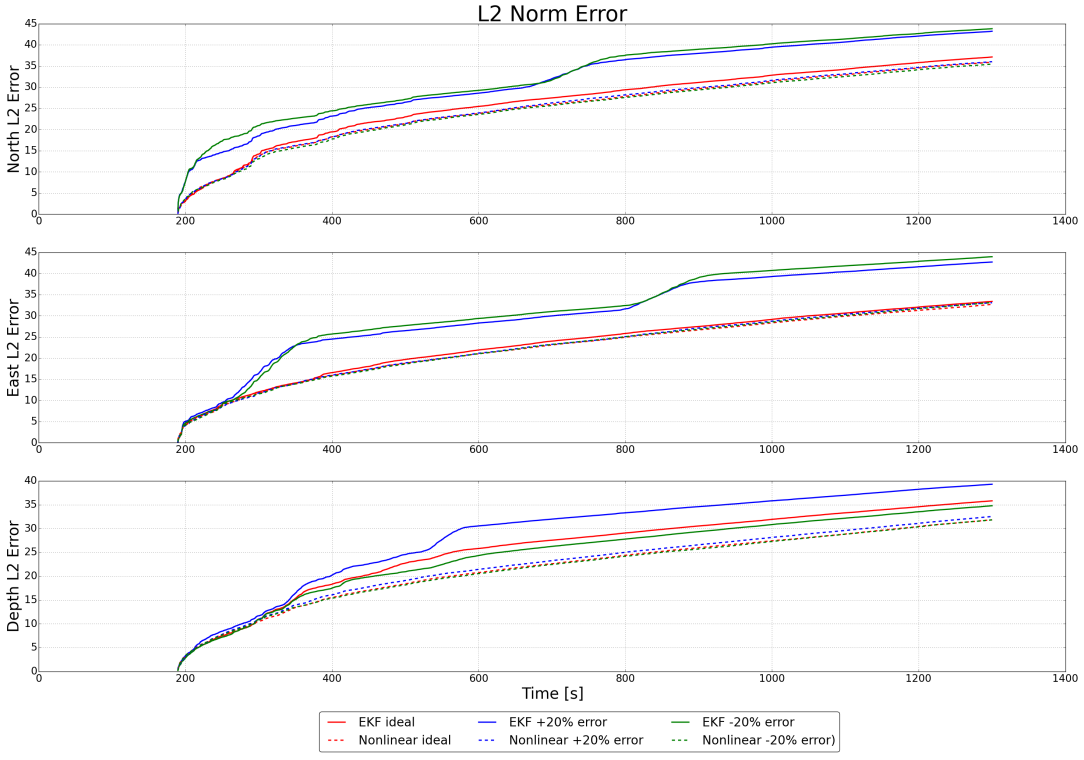

(b) DP system without current observer.

Figure 25: L2 norm error for the model error test of the ROV when moving in surge, sway and heave two times in a row.

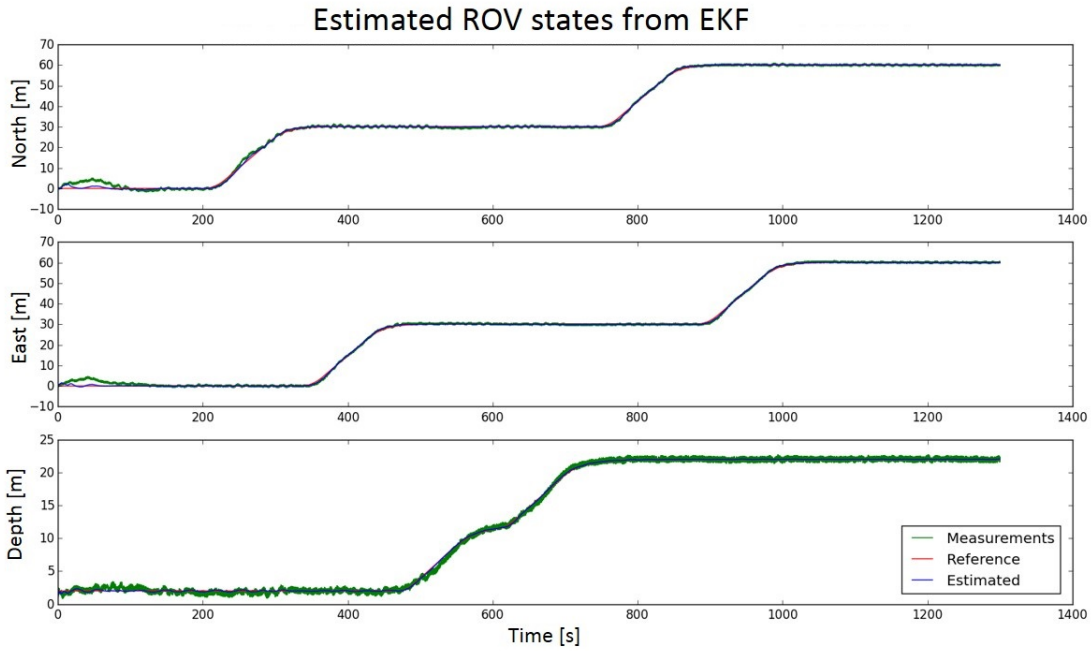

Figure 26: Position profile of test 5 for all observer configurations.

It appears from both figures 25b and 25a that the nonlinear observer is highly resilient to model errors. The L2 error norms are quite similar for the nonlinear observer, regardless if a current observer is used or not. The EKF observer, however, reacts quite significantly to model errors. A sudden increase rate occurs at around points in which the ROV velocity is non-zero. The EKF errors are larger for the case in which a current observer is present, however this is not a lot. The +20% error has the worst EKF performance overall, while the -20% error is somewhat lower in certain dimensions. If only velocity bias error is present, then the EKF performance is unchanged in the east and north dimension, but increased for the depth dimension.

4.4 Observer Wave Estimation Results

This section will review the differences of how the nonlinear observer and EKF estimates wave forces. In all cases a current observer was used in cascade. Due to the complexity of the data presented, and that many of the results share similar characteristics, this section will only present the most interesting and prominent figures that came from simulations.

4.4.1 Test 6, Autonomous Net Traversal

The first set of data will come from test 6. This is shown because it illustrates the main differences between how the nonlinear and EKF observers estimate waves.

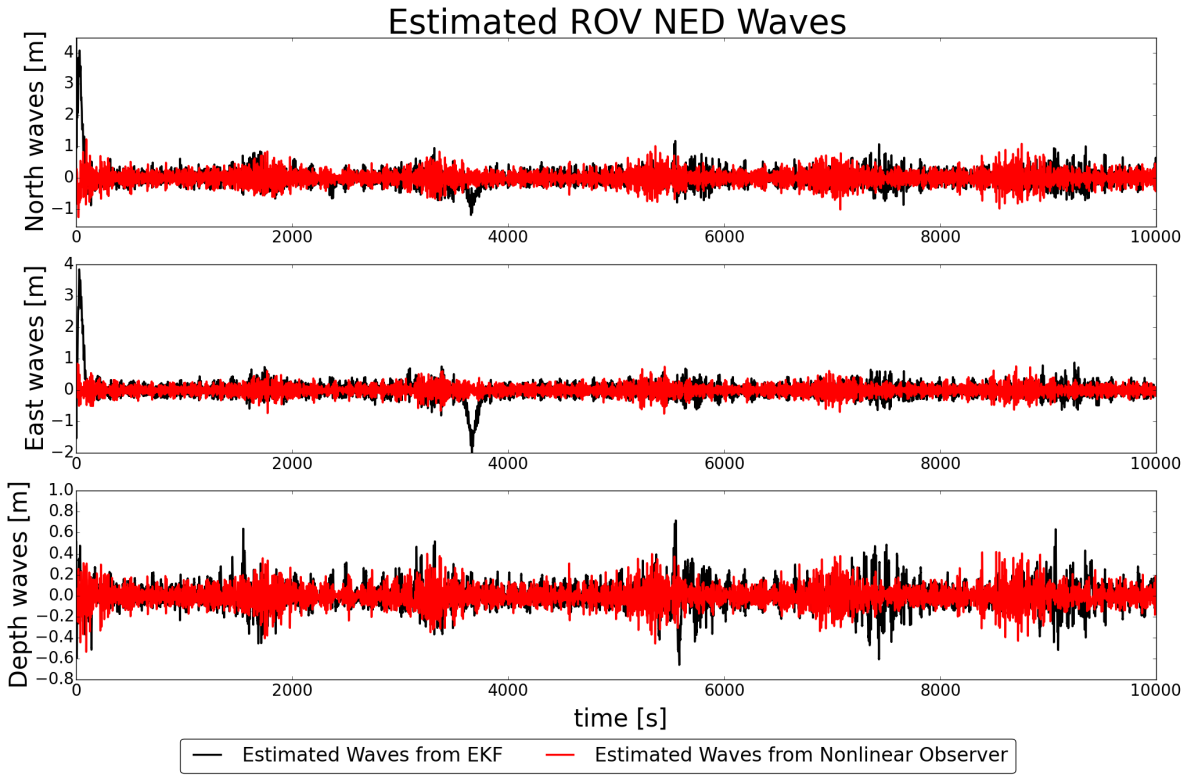

Figure 27: Estimated waves in all dimensions from the EKF and nonlinear observer with a current observer during autonomous net traversal

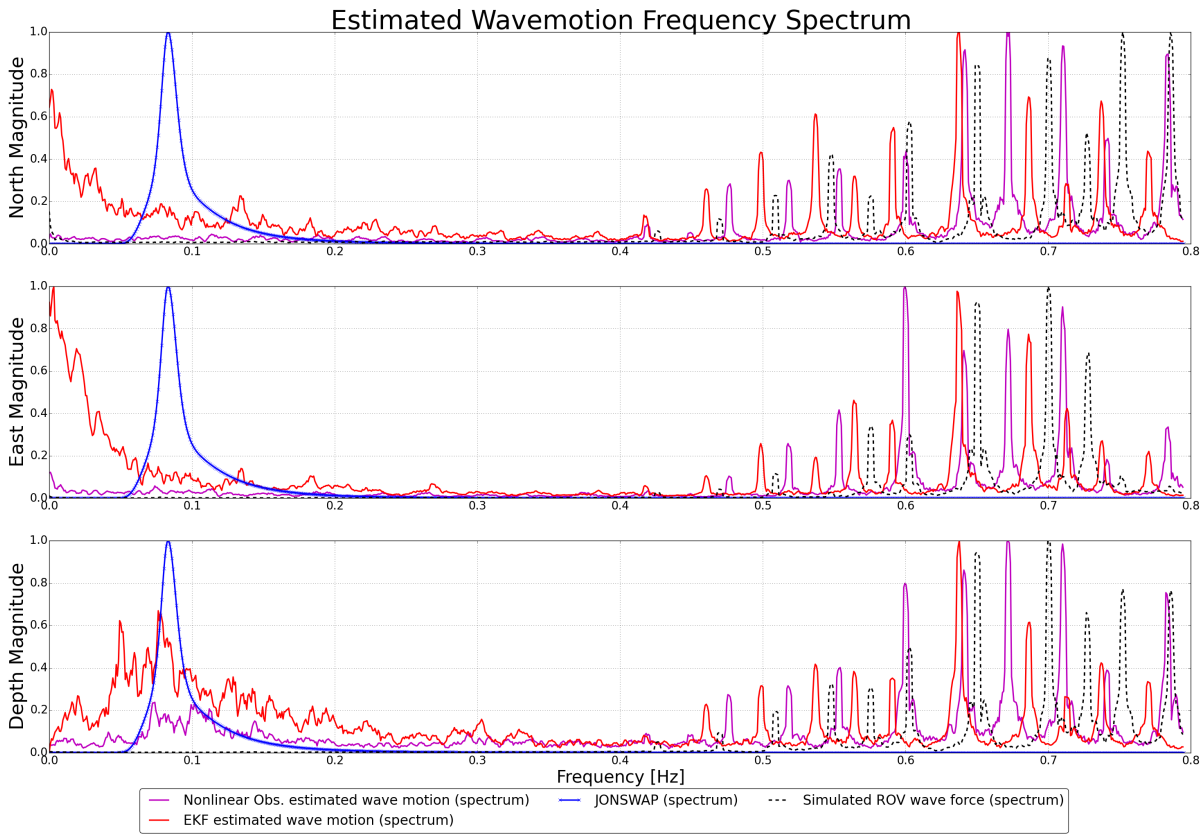

Figure 28: Spectrum of estimated waves from the EKF with a current observer during autonomous net traversal. The JONSWAP spectrum shows the frequencies of the simulated ocean waves.

The nonlinear observer has excellent wave filtering properties compared to the EKF in this simulation. It is seen in figure 27 that the EKF contains more low frequency terms in its estimated waves. A particular incident occuring just before the 4000 second mark has the EKF estimate a non oscillatory motion.

The results of comparing the wave spectrum of the estimated waves in figure 28 clearly illustrate the differences between the EKF and nonlinear observer. The EKF has a large set of estimated waves containing LF components, while the nonlinear observer has most of its estimated waves at the same location as the simulated waves forces.

A peculiarity arises in that for both the EKF and nonlinear observers, the wave spectrum of the simulated waves and the estimated waves is slightly shifted to the side.

It is also interesting to see that the simulated waves force doesn't have the same frequency as the ocean wave, since the JONSWAP spectrum in figure 28 is not located at the same frequency range.

4.4.2 Test 3, Four Simulation Cases

DP1:

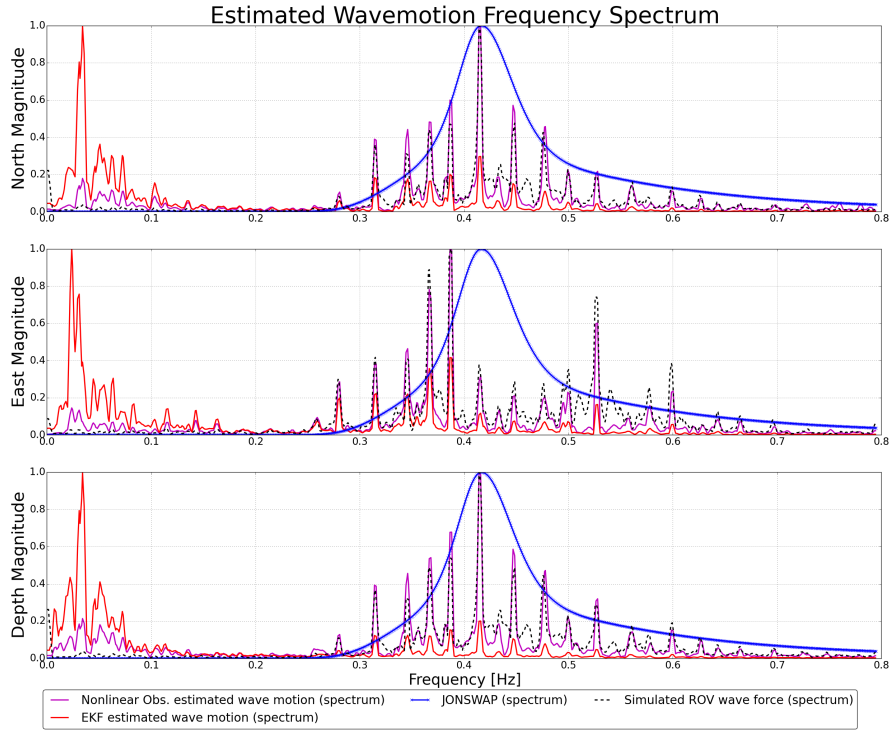

(a) Simulated in depth 2, high current and moderate short crested waves of period 2 s.

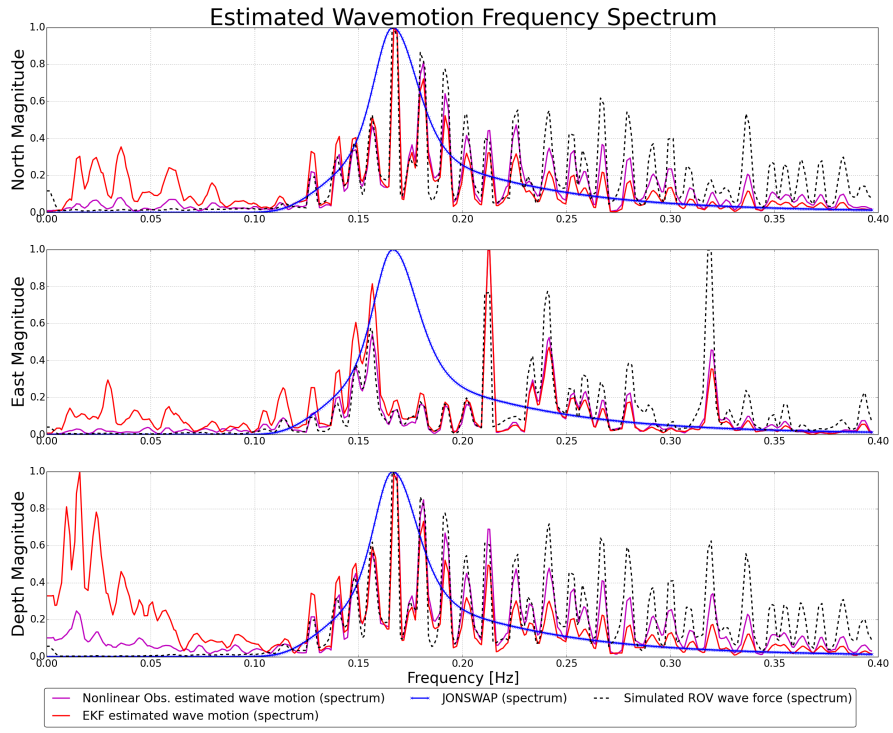

(b) Simulated in depth 2, calm current and calm short crested waves of period 5 s.

Figure 29: Frequency spectrum plot of the estimated wave motion of the observers, simulated ocean waves and simulated ROV wave forces in NED.

DP2:

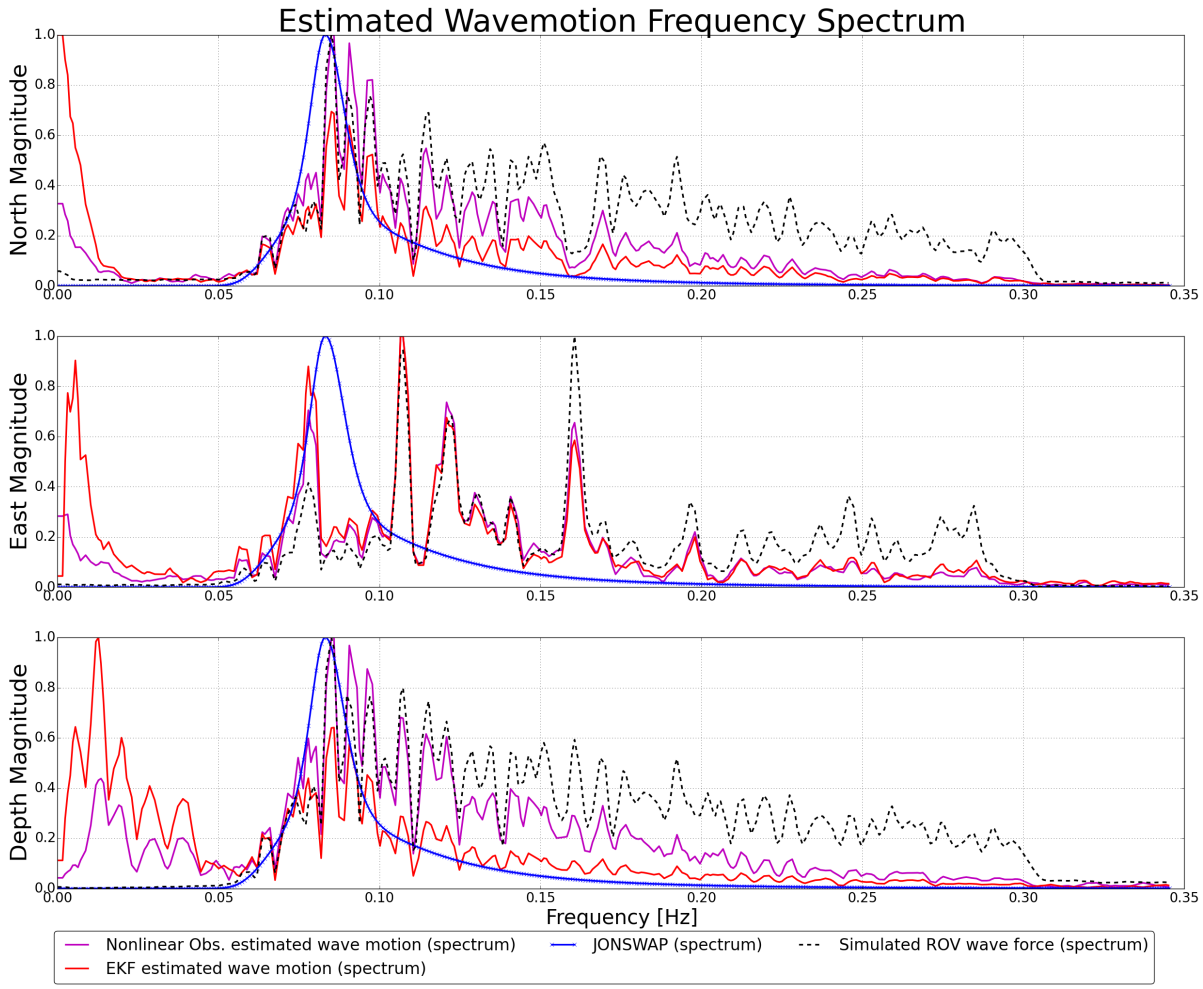

Figure 30: Simulated at depth 2, high current and calm short crested waves of period 10. Frequency spectrum plot of the estimated wave motion of the observers, simulated ocean waves and simulated ROV wave forces in NED.

DP3:

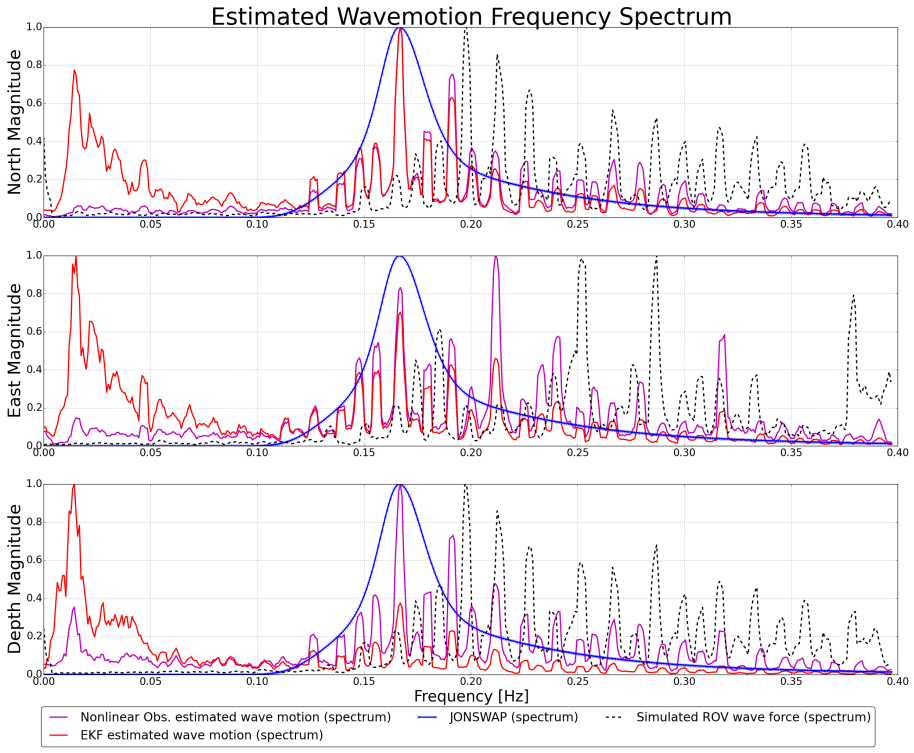

(a) Simulated at depth 2, high current and moderate short crested waves of period 5.

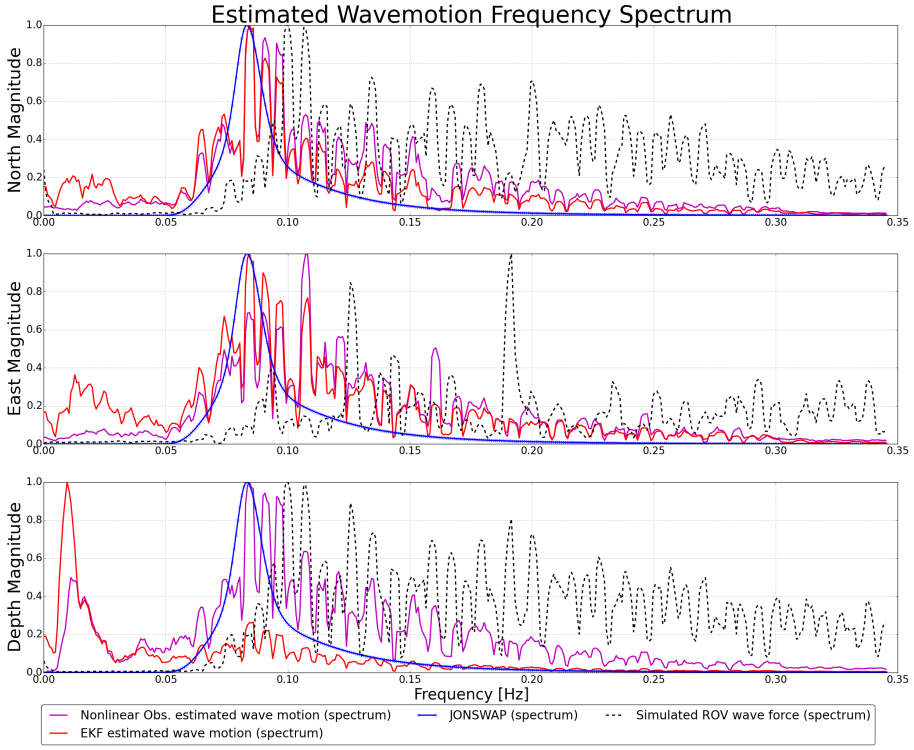

(b) Simulated at depth 2, high current and moderate short crested waves of period 10.

Figure 31: Frequency spectrum plot of the estimated wave motion of the observers, simulated ocean waves and simulated ROV wave forces in NED.

DP4:

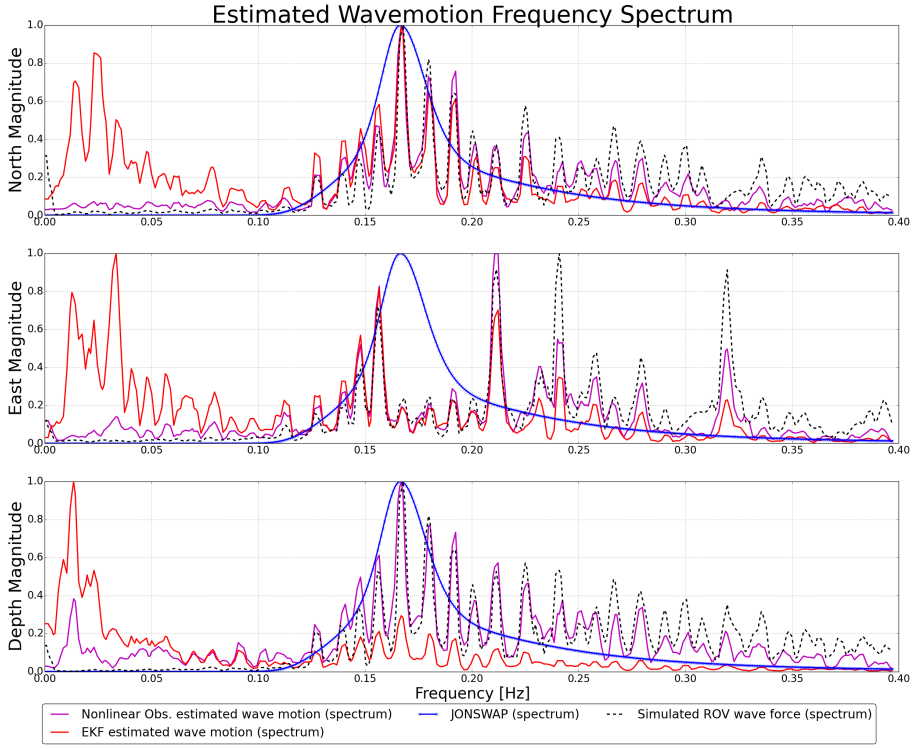

(a) Simulated at depth 2, high current and moderate short crested waves of period 5.

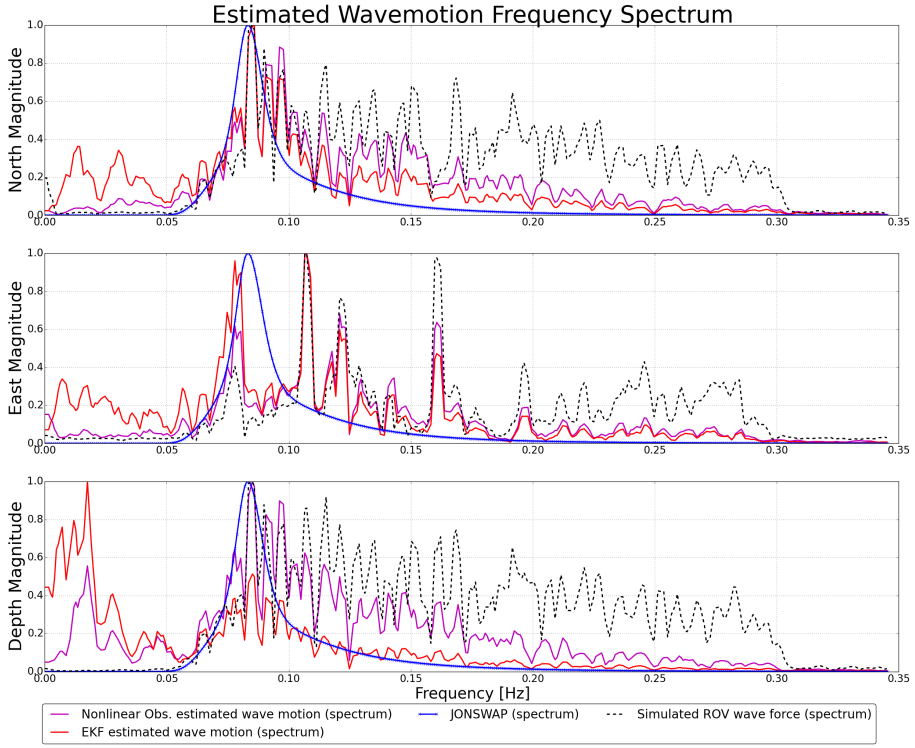

(b) Simulated at depth 2, high current and moderate short crested waves of period 10.

Figure 32: Frequency spectrum plot of the estimated wave motion of the observers, simulated ocean waves and simulated ROV wave forces in NED.

4.4.3 Test 3 Summary

The results of the spectrum of the estimated wave motions are highly varied. The main considerations taken are the extend of low frequency waves the observer estimates, and also whether the simulated wave forces are equal to the simulated ocean waves.

The EKF has a significantly higher amount of lower frequencies in its estimated waves than the nonlinear observer. In cases where the ROV is always influenced by waves , (DP 1, 2, and 4) it is evident that the EKF has less low frequency components in its estimation, the higher the wave period is. Hence it performs better at higher wave periods.

The EKF has considerably bad performance in cases where almost no wave forces are present, which is the case in figure 29a and simulation case DP2. It appears that when calm waves, or no waves are present the wave filter estimates low frequency ROV motion.

The nonlinear observer displays the same phenomena, but to a much less extend. For example, in simulation cases DP 1, 2 and 4 the north and east wave estimates have almost no low frequency components regardless of the wave period.

The simulated ROV wave forces are well tuned to the simulated ocean waves. There is, however, a unique incident in simulation case DP 3 where the simulated wave forces are shifter to higher frequencies. A second incident is that for high frequencies, the simulated wave forces have a significantly higher magnitude than the JONSWAP spectrum of the simulated ocean waves.

4.5 Test 5, Dead Reckoning Tests

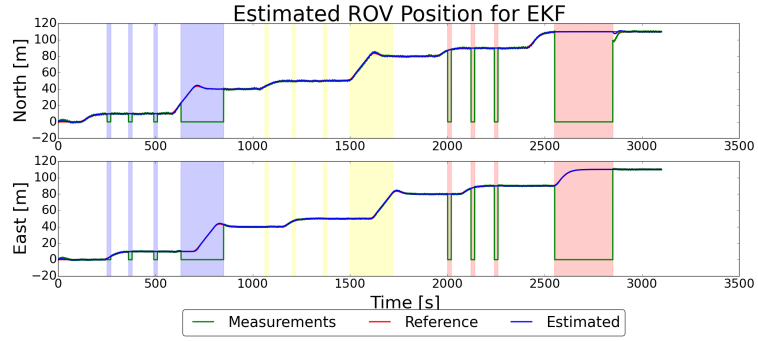

(a) Seed 1, EKF with current observer.

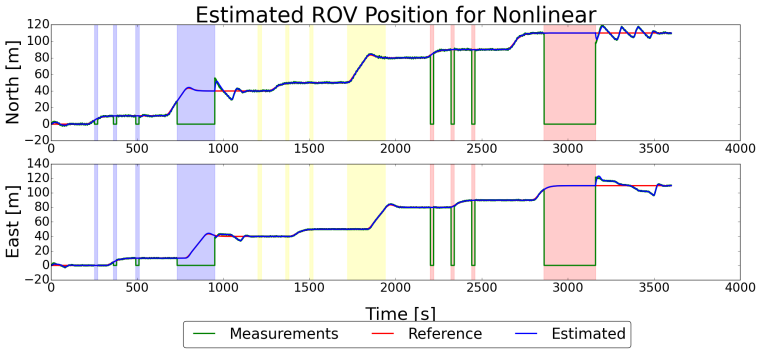

(b) Seed 1, nonlinear observer with current observer.

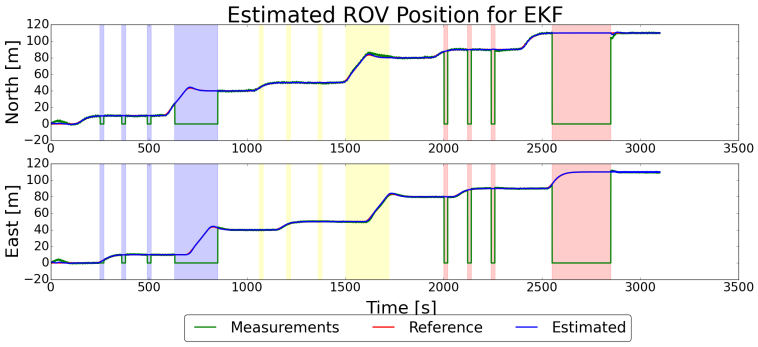

(c) Seed 1, EKF without current observer.

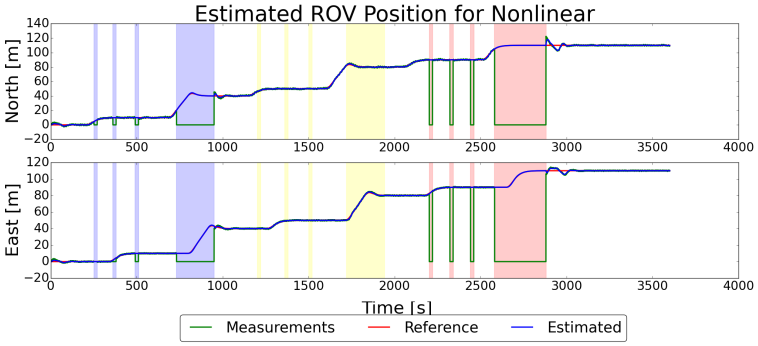

(d) Seed 1, nonlinear observer without current observer.

Figure 33: The estimated positional states from the EKF with current observer during dead reckoning test. Blue segments indicate signal losses in position, yellow segments indicate signal losses in velocity. Red segment indicate signal losses in both.

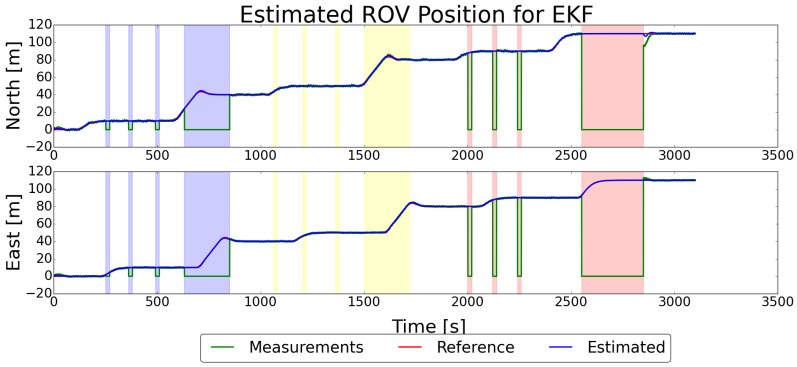

(a) Seed 2, EKF with current observer.

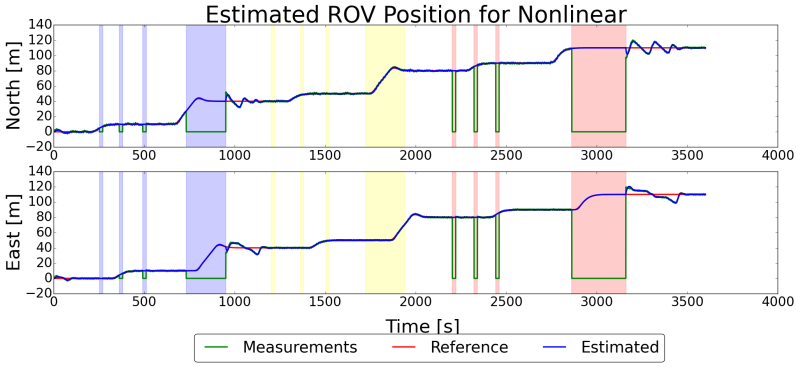

(b) Seed 2, nonlinear observer with current observer.

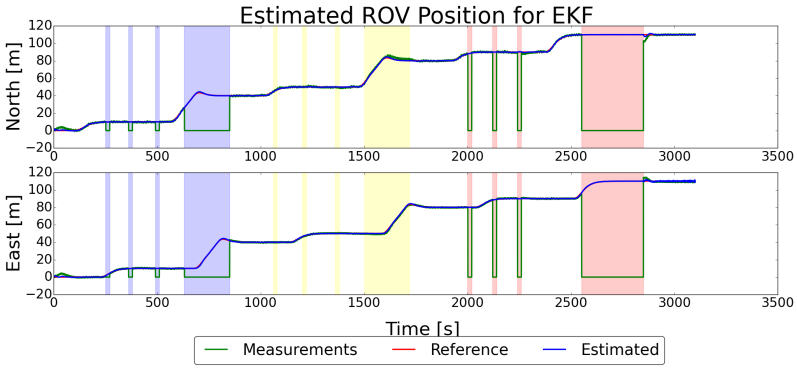

(c) Seed 2, EKF without current observer.

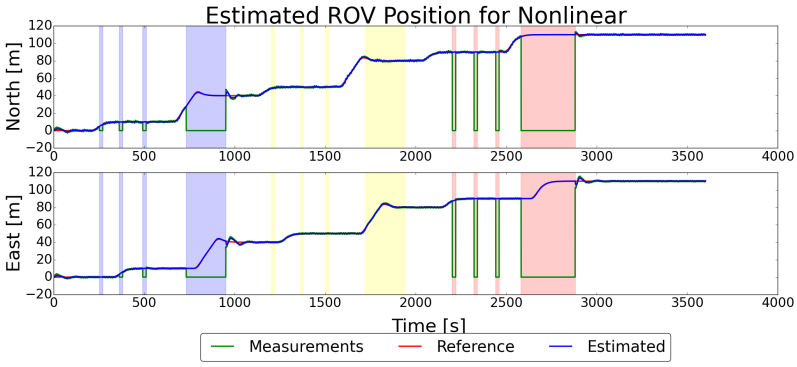

(d) Seed 2, nonlinear observer without current observer.

Figure 34: The estimated positional states from the EKF with current observer during dead reckoning test. Blue segments indicate signal losses in position, yellow segments indicate signal losses in velocity. Red segment indicate signal losses in both.

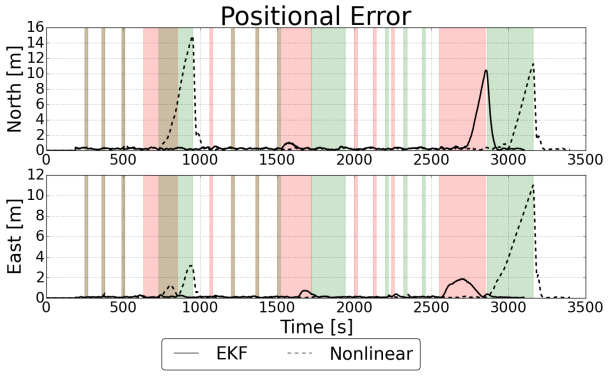

(a) Seed 1, DP with current observer.

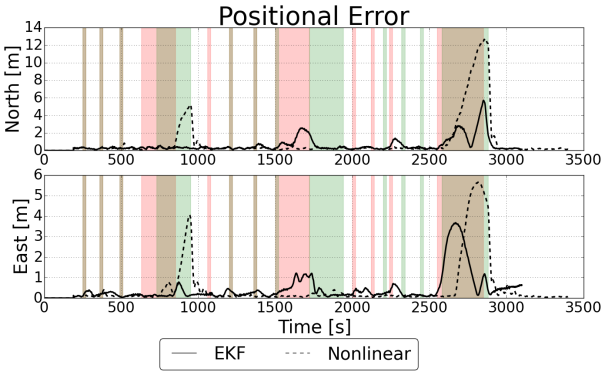

(b) Seed 1, DP without current observer.

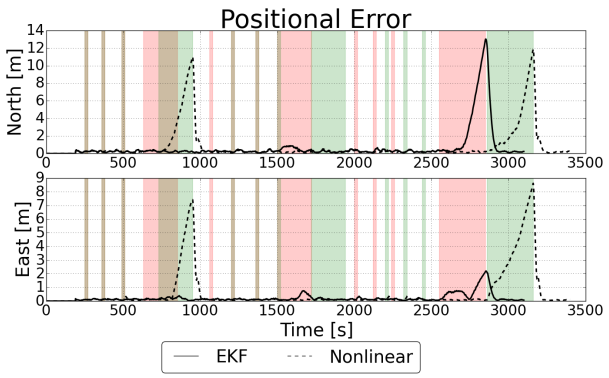

(c) Seed 2, DP with current observer.

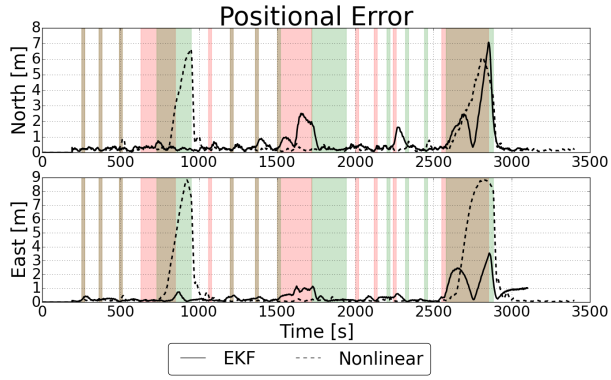

(d) Seed 2, DP without current observer.

Figure 35: The figure shows the error between estimated position and (real) simulated ROV position $\hat{\boldsymbol{\eta}} - \boldsymbol{\eta}_{real}$. Brown markings indicate that both the DP system with nonlinear and EKF observer had a signal loss. Green marks indicate a signal loss for the DP system with a nonlinear observer. Red marks indicate a signal loss for the the DP system with an EKF observer. The first four signal losses are for position measurements only, the four next are for velocity measurements only. The final four are for both position and velocity measurements.

The dead reckoning tests show stark differences between the observer configurations. Unfortunately the concurrent signal loss for position and velocity measurements occurs at different locations for the nonlinear and EKF observers. See figure 33a in which the EKF loses position just when it accelerates in east at time mark 2600 seconds. In figure 33b, the nonlinear observer losses its positional and velocity measurement signals in east after it has accelerated, at time mark 2800. Before the time mark 2000, however, the signal losses occur for all observers when the ROV has an identical movement. Hence the signal losses in iteration 1 and 2 are mostly comparable.

The significant errors occurring during signal losses of the timespan 20 seconds vary from 0 till 2 meters for the EKF observer. For the nonlinear observer these errors are almost non-present.

The EKF has the best dead reckoning qualities overall. It seems resistant to signal losses in only the position measurements for all cases. Without a current observer the EKF has error spikes for when signal losses occur for only the velocity measurements. These errors are small in magnitude however, but are not present if a current observer is used together with the EKF. For signal losses in both velocity and position measurements the EKF performance varies. Errors at the east dimension ranges from maximal 2-4 meters. It is assumed that the differences in errors

at east dimension is dependent on when the signal loss occurred. Errors in the north dimension are larger than the errors in east. It seems that the usage of a current observer amplifies the errors.

The nonlinear observer is greatly affected when signal losses occur in only position measurements, and the magnitude varies. It also seems that the usage of a current observer amplifies the magnitude of these errors for the north dimension. The nonlinear observer is, however, more resistant than the EKF to signal losses in only the velocity measurements. It is relatively unaffected by the signal loss. In seed 1 the nonlinear observer performs a lot worse than the EKF when signal is lost in both position and velocity. The error in east is also increased with the presence of a current observer. In seed 2 the north errors about the same magnitude as for the EKF, but are larger for the east dimension.

4.6 Autonomous Net Traversing Simulation Results

The system is tested in FHSim with the same DP system documented in this thesis. The DP system uses an EKF or a nonlinear observer in cascade with a current observer. The ROV has to traverse the entire cage with as few mistakes as possible using the waypoint algorithm described in section 3.7.6. The ROV travels under high currents of up to $0.5ms^{-1}$, and waves with $H_s = 1.5$. It is assumed that the net shape is constant and not influenced by external forces during simulations.

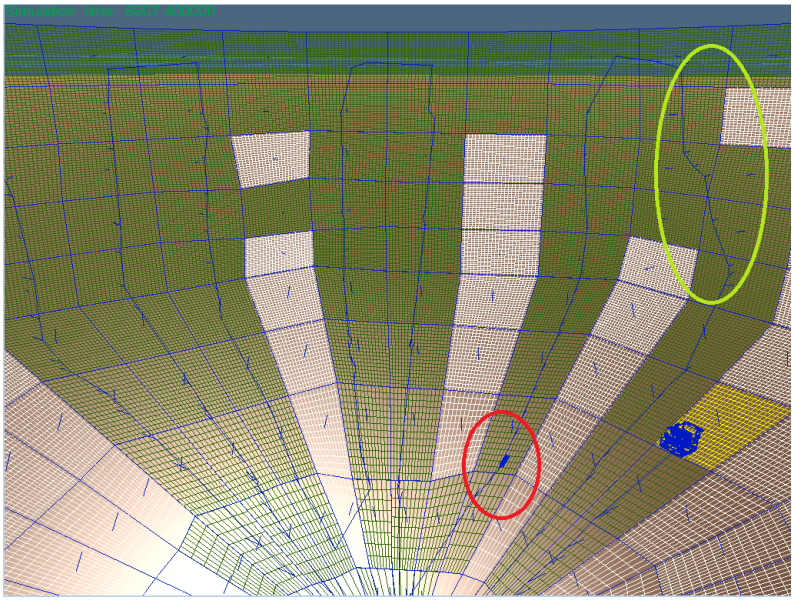

(a) Simulated using an EKF with current observer.

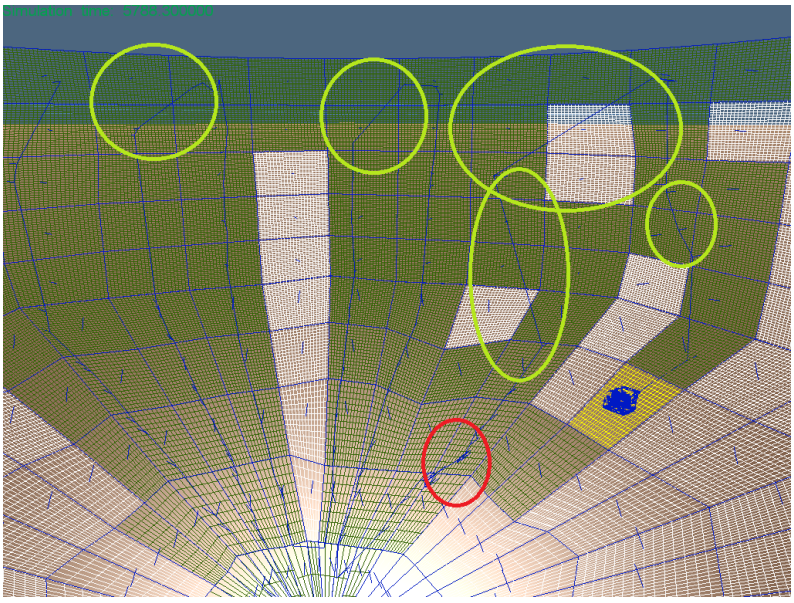

(b) Simulated using a nonlinear observer with current observer.

Figure 36: Visualization of the net traversal algorithm. Blue lines is the ROV trajectory. Green segments indicate segments that have been identified by the ROV. White segments are not identified. Circles mark points of a fault. Red circle show a period in which the ROV has halted, and green circles show diagonal ROV movement.

Based on figure 36a and 36b the ROV is capable of traversing the net. The travelling appears to be smooth overall and the ROV travels vertically during step 1 and 2 most of the time. At certain occasions however, market as green circles the ROV moves sideways instead of vertical. In a more serious occurrence the ROV halts movement, market as a red circles. The ROV also misses whole vertical segments when traversing the net, indicating that the waypoints occasionally have a too large horizontal spread.

It should be noted that the ROV performance varies considerably from run to run. At worst cases the halting occurrences sometimes completely jam the ROV in one spot for the entire simulation. The diagonal movements sometimes sway the ROV completely off course causing it to move outside of the net, or in chaotic paths.

fig:cos1

5 Discussion

5.1 FHSim Integration Method

FHSim is briefly described in section 2.6. It can simulate in fixed discrete or continuous variable time steps n, however for practical and stability purposes the continuous method was chosen. This in effect generated some inconsistencies in how the implemented discrete EKF observer interacted with the time-continuous based modules of FHSim. The implemented EKF is based on that the time of integration occurs at fixed time steps n_{ekf}. However the FHSim integrator used variable time steps of max size n_{max} such that $n_{max} = n_{ekf}$.

This unfortunately means that in comparing the nonlinear observer and the EKF, the nonlinear observer is superior in its integration abilities. The nonlinear observer integrates in accordance with the time-continuous FHSim integrator. The problem is alleviated by the fact that measurements are updated at the same rate as the EKF integrates. Hence the nonlinear observer doesn't get more measurement information than the EKF. It is therefore believed that the integration differences has not played a significant impact on the different behaviours of the two observers during simulation.

5.2 Current Observer and DP Performance

The current observer used is an expansion of the **CIVM Ib** from (Refsnes, 2007). It is extended to include velocity measurements. The current observer was tested in two tests to show its ability to perform under dead reckoning and changing current conditions. The current observer is overall well performing. It does contain a bias error, but this was not eliminated in order to imitate a model error in the surge damping.

There is a second variation of the current observer in (Refsnes, 2007) called **CIVM Ia** which estimates the effects of currents by using a bias term (in the same way the EKF and the nonlinear observers have a bias term). Hence the **CIVM Ia** doesn't directly measure current speed, but is instead the preferred choice in (Refsnes et al., 2007) and experimental tests in (Refsnes, 2007). In a comparison between a set of four observers in (Refsnes, 2007), the **CIVM Ia** and **CIVM Ib** score best, with **CIVM Ib** being somewhat better. As stated in (Refsnes, 2007), the number of tests done to compare these observers were not enough to form a complete comparison between the observers, and it might be that in certain scenarios **CIVM Ia** outperforms **CIVM Ib**, and is a better alternative.

An issue of the designed observer (see equation 32), is that it isn't proven globally asymptotic stable. Even though the simulations performed in this thesis did confirm that it certainly is stable, and in figure 16a and 17a it is shown to be asymptotically stable.

When comparing the estimation errors of the four observer configurations, it is concluded in tables 3, that all observers gain an improvement when using the current observer. It would mean that the bias term of the observers benefits from only having to estimate unmodelled dynamics, while the current observer only estimates current velocity. The direct cause of this improvement, however might come from the improved CPM model which is gained by having the ability to use relative velocities in the DP system.

The results are slightly different when comparing positional errors, however. From tables 4 and 5 it can be concluded that in all cases of tuned bias gains, the addition of a current observer

improves the position errors of the EKF. While only in some cases does it improve the nonlinear observer. By increasing the bias gains in the nonlinear observer, one automatically increases the bias' reactivity to errors in estimated values. This increases its activity to unmodelled dynamics, which can explain why the nonlinear performance increase at higher bias settings. Tuning it to the highest bias setting makes the usage of a current observer obsolete for the nonlinear observer. The bias gains of the EKF are, however, adaptively tuned based on the EKF algorithm. The tuning of $\boldsymbol{Q}$ also doesn't have a proper physical interpretation. Instead one tunes the amount of *process noise* which the EKF can potentially posses in the bias estimates. The different scores of the two filters per bias setting is a good representation of their different estimation qualities.

It should, however, be noticed that only two simulations were performed to gather the data for tables 3, 4 and 5. Each of the simulations had different wave heights. The smallest score differences ranged from 1 till 2 might as well be insignificant. More tests must be done to pinpoint exactly the causes of performance variations.

The main assessment that has to be made, is whether the total observer complexity that arises from using a current observer is worth the slight improvement observed of the estimation errors, and positional errors for the EKF, and for lower bias gains, the nonlinear observer. The addition of a current observer also means that there exists an additional observer that need of tuning.

5.3 Wave Filtering Comparisons

The overall DP performance as assessed in tables 4 and 5, show that the DP performance increase if the bias gains are tuned higher. The EKF always benefits from a current observer, but the nonlinear observer can function equally as good with or without a current observer for higher bias settings. The nonlinear observer outperforms the EKF observer for any bias settings.

Firstly, it is assumed that the main cause of the superior nonlinear observer comes from its better wave estimates. The best test that illustrate this comes from test 3 and 6. The error spike for the EKF occurring in test 6, figure 18, matches quite fine with its faulty wave estimate in figure 27, in time mark of about 3800 seconds. When compared to the error spike of the nonlinear wave filter in the same figure 18, its estimated waves in figure 27 contain no faults. The cause of the error spikes were discovered to have originated from an unknown fault occurring in the simulation in which the current observer operates faulty for a period, until it suddenly works. The time in which the current observer works matches the same time in which the error spikes occur. See figure 37 below for the EKF case.

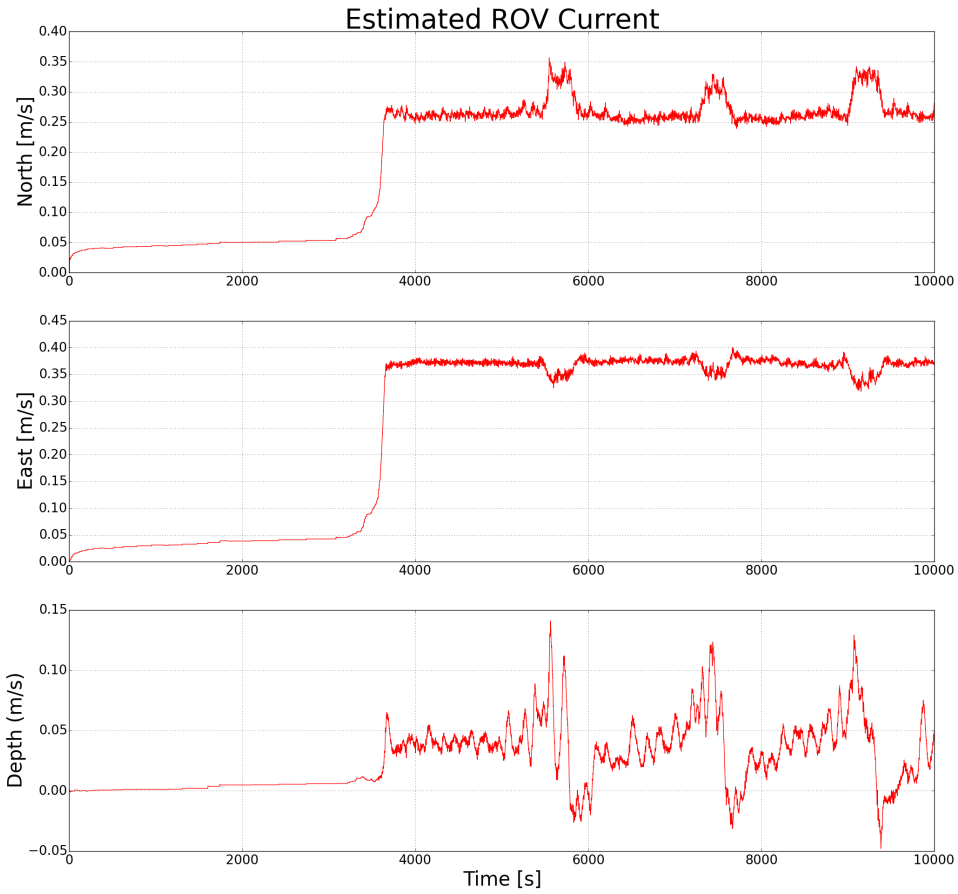

Figure 37: Estimated current for test 6 for the EKF.

The interesting case between these two faults, is that the EKF included low frequency motion in its wave filter estimations at the time of the fault. The nonlinear observer did not.

In test 1 and 3, the estimation errors of the nonlinear observer are much less affected by increasing wave height and period than the EKF. The estimated wave spectrum of the EKF also contains large spikes in the low frequency domain, while the nonlinear filter has no or much smaller spikes. The EKF has thus a greater tendency to include low frequency motion in its wave estimates than the nonlinear observer, which is suspected to cause faulty estimations in the position, and leads to worse positional errors of the ROV.

Both the EKF and nonlinear observer use the same wave estimation filter, and that would indicate that the weaker wave estimates arise from the general design of the EKF rather than its wave filter. Adding a fourth order filter as suggested by (Grimble et al., 1979) could improve the results, but would increase the EKF complexity. A more drastic approach is suggested in (Saelid et al., 1983), in which the wave filter model is defined as:

$$\begin{aligned} \dot{\boldsymbol{\xi}}_1 &= \boldsymbol{\xi}_2 + \boldsymbol{K}_3 \boldsymbol{w}_{w1} \\ \dot{\boldsymbol{\xi}}_2 &= -\boldsymbol{\omega}^2 \boldsymbol{\xi}_1 - 2\boldsymbol{\lambda}\boldsymbol{\omega}\boldsymbol{\xi}_2 + \boldsymbol{K}_4 \boldsymbol{w}_{w2} \end{aligned} \tag{60}$$

and predefined such that $\boldsymbol{K}_4 = -0.2\boldsymbol{K}_3$, in order to further optimize the second order filter. However, by using such a required constant relationships, one would interfere with the EKF kalman gain adaptive algorithm, and secondly, the second order filter used in this thesis doesn't contain the gain constant $\boldsymbol{K}_3$. In (Aguiar et al., 2012) it is suggested that a wave filter is improved by formulating it in the hydrodynamic frame, however, this is anyway implemented in both the EKF and nonlinear observers since velocity measurements are employed in state

estimation.

The fundamental differences between the kalman filter and the nonlinear observer lies in their estimation method. The nonlinear observer has its wave filter tuned as such to represent a notch filter designed to filter out wave motions of known frequency. The kalman filter wave estimation can't be expressed as a notch filter. It is instead a filter tuned to filter out the expected process noise represented as waves. There's no actual physical formulation that can be done to connect the tuning of the wave filter gains in $\boldsymbol{Q}$, to that of the actual wave frequencies in the ocean. Hence one is left to tune the EKF by trial and error. A study in (Tannuri et al., 2003) compares the usage of a kalman filter and a notch filter for wave estimation for DP systems, and concludes wave estimators work equally well for both designs if they are tuned properly. This might suggest that more time should have been spent tuning the EKF.

A second component that might be causing the nonlinear observer to have better wave filtering capabilities might lie in that it integrates continuously, while the EKF has discrete integration. In any case, the true differences between the two observers can only truly be justified by real on-site experimentations, in which both will be discrete.

A final important note is that even if test 3 outlines the weakness of the EKF wave filtering, it is seen in test 6, figure 18, that in overall terms, when the ROV traverses the net, both observer types have the same final accumulated estimation errors, regardless of wave filtering differences.

5.4 Model Errors

The model error test shows that the EKF performs more worse when model errors are induced to the model parameters. A (delayed) review of the code has unfortunately shown that these errors most definitely result in an error in the code in which the jacobian used in the EKF, $\frac{\partial \boldsymbol{f}(\boldsymbol{x}(k),\boldsymbol{u}(k))}{\partial \boldsymbol{x}(k)}\Big|_{\boldsymbol{x}(k)=\hat{\boldsymbol{x}}(k)}$, see Alorithm 1 in appendix, is not affected by error changes added to the model parameters $\boldsymbol{f}(\boldsymbol{x})$. Since $\frac{\partial \boldsymbol{f}(\boldsymbol{x}(k),\boldsymbol{u}(k))}{\partial \boldsymbol{x}(k)}\Big|_{\boldsymbol{x}(k)=\hat{\boldsymbol{x}}(k)}$ is defined as the jacobian of $\boldsymbol{f}(\boldsymbol{x})$, a change in one should affect the other. This means that the discrete integration is erroneous, when changes are made to the model parameters in the code.

The EKF can, however, be compared to the nonlinear observer in the case only a velocity bias gain error is added. When compared to the nonlinear observer, the error of the EKF diverges at specific locations, from the 300 - 500 second time mark. At these points the ROV is close to the surface, having a depth 2 m. At step 300 seconds the ROV is decelerating in surge, and in time mark 400 seconds the ROV is decelerating in sway. When the same movements are repeated in depth 22 m, the EKF has no similar error spikes. This would indicate that the errors from the EKF are amplified when it is affected by wave motion. The same cannot be said for the nonlinear observer.

5.5 Dead Reckoning

The EKF performs very good under dead reckoning tests. The innate ability of the kalman filter to adaptively change its gain matrix $\boldsymbol{K}(k)$ to give the minimum variance estimate makes it behave optimally when signals are lost. As seen the EKF performs quite well without position or velocity measurements. It is especially resistant to losses in position measurements, thus suggesting that the filter primarily uses the velocity measurements as a basis for prediction. When both positional and velocity measurements are lost, however, the performance is often bad for either north and east dimensions. This is because the $\boldsymbol{K}(k)$ is now constant (non adaptive) for these states. Overall, the EKF performance is better than the nonlinear observer.

During signal losses in velocity, the EKF improves performance if it has a current observer. This could be explained by the improved CPM model of the observer, which now includes relative velocities in the calculations. However, when position and velocity measurements are lost, the addition of a current observer seems to amplify the errors.

The dead reckoning of the nonlinear observer is more worse than the EKF. It appears that the observer relies quite heavily on its position measurements. A loss in position signals gives the nonlinear observer errors as large as if it losses position and velocity signals. This is mainly attributed to how it is tuned. Both velocity gains of $\boldsymbol{K}_{2\nu}$ and $\boldsymbol{K}_{3\nu}$ were equal to $\mathbf{0}$. Hence a loss in position signals drastically reduces the injection terms of the observer. Utilizing $\boldsymbol{K}_{2\nu}$ and $\boldsymbol{K}_{3\nu}$ more for the estimation would improve dead reckoning, but could also change the nonlinear observer performance. In case only velocity signals are lost, the nonlinear observer performance show no degradation. As compared to the EKF, the nonlinear observer doesn't have adaptive gains, thus changes in signal losses/availability won't change the gains, as it would in the EKF. This makes the nonlinear observer more vulnerable to signal losses. Based on results, the addition of a current observer appears to worsen the nonlinear observer performance, but more simulations are needed for a proper conclusion.

5.6 Autonomous Traversal Algorithm

The ROV is capable of traversing the cage, but not without faults. Three different error types are identified: *empty LOS*, *wrong identification* and *bad waypoint*. Two of the faults: *wrong identification* and *bad waypoint* are non-critical since they don't cause the ROV to halt its movement. *empty LOS* is however a more critical fault causing the ROV not to know where to move next. The faults are discussed below.

Fault: *empty LOS* The visualization module can't identify *new* segments inside the ROV LOS. This causes the ROV not to update its next waypoint, and thus causes it to halt position. The cause of this fault lies entirely in the visualization module. The fault often occurs in the vicinity between the cone and cylinder, and when the ROV is traevlling between two segments. The red circle in figure 36a show the occurence of such a fault.

Fault: *bad waypoint* This fault is due to bad tuning of ζ parameters, and makes the ROV travel in such a way that not all segments are traversed. The white segments in figure 36a trapped inside green coloured ones, are the result of this error.

Fault: *wrong identification* This fault is also the cause of a bad field of view for the ROV. The ROV identifies segments that are on the edge of its FoV, thus causing it to move sideways instead of upwards. The green circles in figure 36a, illustrate such occurrences. However it doesn't impede the ROV from continuing traversing.

A final weakness with the algorithm is that is assumes the cage is circular. This is not always true, in the exposure of high current speed, the cage will become elliptic. Step 3 in the waypoint algorithm is especially vulnerable to such a deviation.

5.7 Simulation Weaknesses

It is a given that the simulation done here might not represent the true behaviour of the DP system at on-site operations. This would come from model simplifications of the ROV, and ocean waves. Such simplifications are, however, quite common to use and seen as essential in order to make the simulator run fast in real-time.

However, there does exist specific simulation weaknesses that are more tightly linked to the wave estimation results (which seperated the performance of the two main observers). One of these is that the first order wave forces on the ROV, $\boldsymbol{\tau}_{wave1}$, is simplified as noted in section 2.3.8 using Froude Krylov Forces, and the ROV is treated as a rectangle. The wave drift forces $\boldsymbol{\tau}_{wave2}$ equal to $\mathbf{0}$, and are instead expressed in the relative velocity term $\boldsymbol{\nu}_r = \boldsymbol{\nu} - \boldsymbol{\nu}_w - \boldsymbol{\nu}_c$ as $\boldsymbol{\nu}_w$. Hence, the method in which the wave motion of the ROV is modelled is slightly more simplified, than what it needs to. The more standard approaches to simulate wave motion was employed originally, but were also later retracted due to obscure errors caused by their inclusion.
A second, but not as critical simplification, as noted in 2.6, is that the ROV doesn't affect the ocean in which it is present in. However, as noted in (Reite et al., 2014), this is the effect of requiring that FHSim can perform relatively fast computations real-time effectively. This error is not seen as something that would require modification.

6 Future Work

6.1 Dynamic Position System

The errors causing the current observer to not functions in figure 37 has to be addressed, and the EKF has to properly change its jacobian matrix when its model parameters are altered. Further tests could also be done to assess whether the EKF wave filtering is degraded because of it is discrete. A simple way to do this could be by for example comparing the error rate of the EKF with the integrator time steps.

More research has to be done in the area of observers employing velocity sensors, especially in terms of wave filtering. Most wave filters today are based on that only position estimates are present. There exists few studies on the ideal design of a wave filter, especially with regards to the EKF, if position *and* velocity measurements are available. Ultimately an efficient adaptive algorithm could help fine-tune the wave filter of the observer for the ocean conditions.

With regards to the overall DP system, most research are based on large heavy vessels such as ships and tankers. There are areas of improvements for small light sized vessels, such as ROVs, in regards to wave filtering. In (Sørensen et al., 2002) it was suggested that during extreme weather, the wave filter should be turned off for marine vessels. Something similar could perhaps apply for ROVs' in weather conditions that would relatively impact the ROV as much as a strong storm would impact a ship. A hybrid controller could perhaps be used to adjust the wave filtering abilities of an observer dependent on how the vessel reacts to waves. Some wave motions could be filtered away, while other employed by the ROV to ease its motion.

In the end, the conclusions regarding the data gained from these simulations can only be confirmed after experimental on-site tests of the vehicle, which is the most important next step.

6.2 Autonomous Traversal Algorithm

In order to improve upon the identified faults it is suggested the following:

Improvement: ***empty LOS*** If the ROV is unable to identify a new segment set, it should utilize the previous segment set and the position of the neighbours of those segments to generate a new waypoint. The visualization module already has a neighbour set defined for each segment. The line of sight method should also be reviewed.

Improvement: ***bad waypoint*** Bad waypoints were generally made during step 3 of the traversing. That is when the ROV is on the top cage and moves sideways. Step 3 could be

improved by assuming that the top of the cage is always elliptical, and hence by using interpolation, the position of all top can be predicted as more segments are discovered. Using this assumption one can simply choose the next waypoint to be the neighbour of the current segment in LOS. For bad waypoints generated beneath the top segments, one could suggest that waypoints are generated using a smart approach, in which the location of the next segment to be observer was predicted based on the set of previously identified segments. This would allow the ROV to move in a smarter way.

Improvement: ***wrong identification*** A test could be used to determine whether the identified segment is in fact a predicted location. This could be done by testing whether the segment identified is the neighbour the previously identified segment set. By utilizing the ROV desired next position, and the wrongly identified segment, it could be possible for the ROV to decide whether it should ignore the current identification and continue on its previous waypoint, or not. The line of sight method should also be reviewed.

It is suggested that even if these improvements were applied, the best alternative to optimize the ROV trajectory, would be to develop a guidance law for surface net tracking. The waypoint method designed is too simple to work for more complicated shapes. The tuning parameter ζ_d used to define the distance from the ROV to the next waypoint is highly dependent on the surface shape, segment sizes, and ROV line of sight. It is difficult to estimate a good ζ_d value. For example the error type defined as *empty LOS*, is the result of a ζ_d of a too low value. However if the value of ζ_d is increased too much, then the result of badly generated waypoints are amplified, causing the ROV to move diagonal instead of vertically upwards or downwards. A ζ_d tuned to a large value will also cause the ROV to miss the boundary line between where the cage is a cylinder and a cone, making the ROV unrealistically move through the net. Increasing the number of segments for the cage, thus reducing each segment size, might alleviate some of these issues.

The vision field of the ROV is also in need of improvements. Ideally it must replicate DVL measurements as done for example in (Dukan, 2014). An improved vision field with a robust surface tracking guidance law is the suggested option for optimal ROV net traversing.

7 Conclusion

The thesis improves upon the DP system of an ROV tasked to inspect fish farming cage sites exposed to moderate wave conditions of high current speed. This included adding velocity measurements to an EKF and nonlinear observer, and a current observer. In total, four different observer types of the DP system were compared in performance via assessing their wave filtering, estimation and positional errors, and dead reckoning abilities. The DP system was also improved by adding an autonomous net traversal algorithm which generates waypoints based on how the ROV visualizes the net. A set of several simulation tests were designed in order to properly compare the different observer types. It was seen that nonlinear observers outperformed the EKF observers in terms of wave filtering, estimation and position errors for most of the tests. The EKF was superior in dead reckoning. When tested for net traversal, both were equally good in terms of estimation error. The addition of current observers did in some cases improve the main EKF and nonlinear observer. The performance differences is attributed to that the EKF was perhaps not optimally tuned, and that it was a discrete system, as opposed to the continuous nonlinear observer. In any cases, proper conclusions should only be confirmed after experimental ocean trials. The autonomous net traversal algorithm functioned quite well for simple cylindrical cages, but it also contained some faults regarding way point placements, and its vision field. Overall, the algorithm was seen to be too simplistic to function properly for real situations in which the net cage is more irregular. It was shown that the ROV was fully capable of traversing the inside of a cylindrical formed cage autonomously under moderate wave conditions of high current speed. Further improvements suggested included a new autonomous algorithm better adapted to irregular cages, and more research is suggested on how ROV performance is affected in wave conditions, and how to optimally design observers, when they have velocity measurements.

Bibliography

A. Pedro Aguiar and Pascoal A.M. Dynamic positioning and way-point tracking of underactuated AUVs in the presence of ocean currents. In *Conference on Decision and Control*, volume 2, 2002. doi: 10.1109/CDC.2002.1184840.

A Pedro Aguiar, António M Pascoal, A.J. Sorensen, and Vahid Hassani. A linear design model for wave filtering and dynamic positioning. In *CONTROLO'2012*, 2012.

Sørensen A.J., Sagatun S.I., and T.I. Fossen. Design of a dynamic positioning system using model-based control. *Control Engineering Practice*, 4(3):359 – 368, 1996. ISSN 0967-0661. doi: http://dx.doi.org/10.1016/0967-0661(96)00013-5.

J.G. Balchen. Possible roles of remotely operated underwater vehicles (ROV) and robotics in mariculture of the future. *Modeling Identification and Control*, 12:207–217, 1991. doi: 10.4173/mic.1991.4.3.

Fredrik Dukan. *ROV Motion Control Systems*. PhD thesis, Department of Marine Technology, Faculty of Engineering Science and Technology, NTNU, 2014.

A. Edwards and D.J. Edelsten. Marine fish cages—the physical environment. *Proceedings of the Royal Society of Edinburgh. Section B. Natural Environment*, 75:207–221, 1 1976. ISSN 0269-7270. doi: 10.1017/S0308211300002668.

Thomas Falkenberg, René Tavs Gregersen, and Mogens Blanke. *Navigation System Fault Diagnosis for Underwater Vehicle*, volume 19. International Federation of Automatic Control, 2014.

Odd M. Faltinsen. *Sea loads on ships and offshore structures*, volume 1. Cambridge University Press, 1993.

V. Filaretov, A. Zhirabok, and A. Zuev. The development of the adaptive diagnostic system for navigation sensors of autonomous underwater vehicles. In *Mechatronics and Automation (ICMA), 2012 International Conference on*, pages 1704–1709, Aug 2012. doi: 10.1109/ICMA.2012.6284393.

T.I. Fossen. *Guidance and Control of Ocean Vehicles*. John Wiley and Sons Ltd., 1994.

T.I. Fossen. *Marine Control Systems: Guidance, Navigation and Control of Ships, Rigs and Underwater Vehicles*. Marine Cybernetics, 2002.

T.I. Fossen. *Handbook of marine craft hydrodynamics and motion control*. John Wiley & Sons, 2011.

T.I. Fossen and T.A. Johansen. A survey of control allocation methods for ships and underwater vehicles. In *Control and Automation, 2006. MED '06. 14th Mediterranean Conference on*, pages 1–6, June 2006. doi: 10.1109/MED.2006.328749.

T.I. Fossen and J.P. Strand. Passive nonlinear observer design for ships using lyapunov methods: full-scale experiments with a supply vessel. *Automatica*, 35(1):3 – 16, 1999. ISSN 0005-1098. doi: http://dx.doi.org/10.1016/S0005-1098(98)00121-6. URL `http://www.sciencedirect.com/science/article/pii/S0005109898001216`.

A.R. Frost, A.P. McMaster, K.G. Saunders, and S.R. Lee. The development of a remotely operated vehicle (rov) for aquaculture. *Aquacultural Engineering*, 15(6):461 – 483, 1996. ISSN 0144-8609. doi: http://dx.doi.org/10.1016/S0144-8609(96)01004-7. URL `http://www.sciencedirect.com/science/article/pii/S0144860996010047`.

RS Gibson, C Swan, and PS Tromans. Fully nonlinear statistics of wave crest elevation calculated using a spectral response surface method: Applications to unidirectional sea states. *JOURNAL OF PHYSICAL OCEANOGRAPHY*, 37:3–15, 2007. doi: 10.1175/JPO2956.1. URL `http://dx.doi.org/10.1175/JPO2956.1`.

Roberts G.N. and Sutton R. *Further Advances in Unmanned Marine Vehicles*. The Institution of Engineering and Technology, 2012.

M.J. Grimble, R.J. Patton, and D.A. Wise. The design of dynamic ship positioning control systems using extended kalman filtering techniques. In *OCEANS '79*, pages 488–497, Sept 1979. doi: 10.1109/OCEANS.1979.1151295.

Vahid. Hassani, A.J. Sorensen, António M Pascoal, and A Pedro Aguiar. Multiple model adaptive wave filtering for dynamic positioning of marine vessels. In *American Control Conference (ACC), 2012*, pages 6222–6228. IEEE, 2012.

M. N. Hval. *Modelling and control of underwater iinspection vehicle for aquaculture sites*. PhD thesis, Norwegian University of Science and Technology, Department of Marine Technology, 2012.

Dave Jackson, Alan Drumm, Sarah McEvoy, Østen Jensen, Diego Mendiola, Gorka Gabiña, Joseph A. Borg, Nafsika Papageorgiou, Yannis Karakassis, and Kenneth D. Black. A pan-european valuation of the extent, causes and cost of escape events from sea cage fish farming. *Aquaculture*, 436(0):21 – 26, 2015. ISSN 0044-8486. doi: http://dx.doi.org/10.1016/j.aquaculture.2014.10.040. URL `http://www.sciencedirect.com/science/article/pii/S0044848614005481`.

Ø. Jensen, T. Dempster, E. B. Thorstad, I. Uglem, and A. Fredheim. Escapes of fishes from norwegian sea-cage aquaculture: causes, consequences and prevention. *Aquaculture Environment Interactions*, 1:71–83, 2010. doi: 10.3354/aei00008.

Balchen J.G, Jenssen N.A., and Sælid S. Dynamic Positioning Using Kalman Filtering and Optimal Control Theory. *IFAC/IFIP Symposium On Automation in Offshore Oil Field Operation*, pages 183–186, 1976.

David Johansson, Jon-Erik Juell, Frode Oppedal, Jan-Erik Stiansen, and Kari Ruohonen. The influence of the pycnocline and cage resistance on current flow, oxygen flux and swimming behaviour of atlantic salmon (salmo salar l.) in production cages. *Aquaculture*, 265(1–4):271 – 287, 2007. ISSN 0044-8486. doi: http://dx.doi.org/10.1016/j.aquaculture.2006.12.047. URL `http://www.sciencedirect.com/science/article/pii/S0044848606009197`.

J. Jouffroy and T.I. Fossen. A Tutorial on Incremental Stability Analysis using Contraction Theory. *Modeling, Identification and Control*, 31(3):93–106, 2010. doi: 10.4173/mic.2010.3.2.

V. Katsardi and C. Swan. The evolution of large non-breaking waves in intermediate and shallow water. i. numerical calculations of uni-directional seas. *Proceedings of the Royal Society of London A: Mathematical, Physical and Engineering Sciences*, 2010. ISSN 1364-5021. doi: 10.1098/rspa.2010.0280.

V.J. Kurian, C.Y. Ng, and M.S. Liew. Numerical investigation on dynamic responses of classic spar platforms: Long crested waves vs. short crested waves. In *Humanities, Science and Engineering (CHUSER), 2012 IEEE Colloquium on*, pages 724–728, Dec 2012. doi: 10.1109/CHUSER.2012.6504407.

P. Lader, T. Dempster, A. Fredheim, and Ø. Jensen. Current induced net deformations in full-scale sea-cages for atlantic salmon (salmo salar). *Aquacultural Engineering*, 38(1):52 –

65, 2008. ISSN 0144-8609. doi: http://dx.doi.org/10.1016/j.aquaeng.2007.11.001. URL http://www.sciencedirect.com/science/article/pii/S0144860907000957.

K.-P. Lindegaard and T.I. Fossen. A model based wave filter for surface vessels using position, velocity and partial acceleration feedback. In *Decision and Control, 2001. Proceedings of the 40th IEEE Conference on*, volume 1, pages 946–951 vol.1, 2001. doi: 10.1109/.2001.980231.

Karl-Petter Lindegaard. *Acceleration Feedback in Dynamic Positioning*. PhD thesis, Norwegian University of Science and Technology, Department of Engineering Cybernetics, 2003.

John Nicholas Newman. *Marine Hydrodynamics*. MIT Press, 1977.

Norwegian Meteorological Institute. Orkan flere steder langs kysten, 2013. URL http://artikkel.yr.no/orkan-flere-steder-langs-kysten-1.11361839. [Accessed: 2015-01-15].

Fredric Raichlen. *Waves*. The MIT Press essential knowledge. Cambridge, Mass. : MIT Press, 2012.

J. Refsnes, A.J. Sorensen, and K.Y. Pettersen. A 6 dof nonlinear observer for auvs with experimental results. In *Control Automation, 2007. MED '07. Mediterranean Conference on*, pages 1–7, June 2007. doi: 10.1109/MED.2007.4433891.

J.E.G. Refsnes. *Nonlinear Model-Based Control of Slender Body AUV's*. PhD thesis, Department of Engineering Cybernetics, Norwegian University of Science and Technology, 2007.

Karl-Johan Reite, Martin Føre, Karl Gunnar Aarsæther, Jørgen Jensen, Per Rundtop, Lars T. Kyllingstad, Per Christian Endresen, David Kristiansen, Vegar Johansen, and Arne Fredheim. Fhsim — time domain simulation of marine systems. *ASME 2014 33rd International Conference on Ocean, Offshore and Arctic Engineering*, 8A Ocean Engineering, 2014. doi: 10.1115/OMAE2014-23165.

Robert F. Roddy, David E. Hess, and Will Faller. Neural network predictions of the 4-quadrant wageningen propeller series. 2006.

Eivind Ruth. Propulsion Control and Thrust Allocation on Marine Vessels. 2008.

S. Saelid, N.A. Jenssen, and J.G. Balchen. Design and analysis of a dynamic positioning system based on kalman filtering and optimal control. *Automatic Control, IEEE Transactions on*, 28(3):331–339, March 1983. ISSN 0018-9286. doi: 10.1109/TAC.1983.1103225.

J.S. Sargent and P.N. Cowgill. *Design Considerations for Dynamically Positioned Utility Vessels*. Offshore Technology Conferencel, Dallas U.S.A, 1976.

T.S. Schei. Wave disturbance filtering in dynamic positioning systems. *Modeling, Identification and Control*, 17(2):87–96, 1996. doi: 10.4173/mic.1996.2.2.

SNAME. Nomenclature for Treating the Motion of a Submerged Body Through a Fluid. 1950.

A.J. Sørensen, J.P. Strand, and H. Nyberg. Dynamic positioning of ships and floaters in extreme seas. In *OCEANS '02 MTS/IEEE*, volume 3, pages 1849–1854 vol.3, Oct 2002. doi: 10.1109/OCEANS.2002.1191913.

Asgeir J. Sørensen. *Marine Cybernetics Modelling and Control Lecture Notes*. Department of Marine Technology NTNU, 2013.

S Steen. *Marin teknikk 3 - Hydrodynamikk. Motstand og Propulsjon. Propell og foilteori*. Department of marine Technology, NTNU UK-2007-99, 2007.

J. P. Strand. Nonlinear Position Control Systems Design for Marine Vessels. 1999.

Jann Peter Strand and T.I. Fossen. Nonlinear passive observer design for ships with adaptive wave filtering. In H. Nijmeijer and T.I. Fossen, editors, *New Directions in nonlinear observer design*, volume 244 of *Lecture Notes in Control and Information Sciences*, pages 113–134. Springer London, 1999. ISBN 978-1-85233-134-4. doi: 10.1007/BFb0109924. URL `http://dx.doi.org/10.1007/BFb0109924`.

E.A. Tannuri, T.T. Bravin, and C.P Pesce. Dynamic positioning systems: Comparison between wave filtering algorithms and their influence on performance. In *ASME 2003 22nd International Conference on Offshore Mechanics and Arctic Engineering*, pages 109–117. American Society of Mechanical Engineers, 2003.

G. Torsetnes, J. Jouffroy, and T.I. Fossen. Nonlinear dynamic positioning of ships with gain-scheduled wave filtering. In *Decision and Control, 2004. CDC. 43rd IEEE Conference on*, volume 5, pages 5340–5347 Vol.5, Dec 2004. doi: 10.1109/CDC.2004.1429657.

D. J. Wildish, P. D. Keizer, A. J. Wilson, and J. L. Martin. Seasonal changes of dissolved oxygen and plant nutrients in seawater near salmonid net pens in the macrotidal bay of fundy. *Canadian Journal of Fisheries and Aquatic Sciences*, 50(2):303–311, 1993. doi: 10.1139/f93-035. URL `http://dx.doi.org/10.1139/f93-035`.

Appendix A - Properties and Algorithm

This section will present the properties from other studies that were used to perform specific mathematical transformations used for stability proofs. In particular, the EKF algorithm is also presented.

Property 1 (Lindegaard, 2003)

A1. Assume the orientation angle between NED and body-fixed frame is based on the measured heading ψ_y.

$$\begin{aligned} \dot{\boldsymbol{\eta}} &= \boldsymbol{R}(\psi_y)\boldsymbol{\nu} \\ \boldsymbol{M}\dot{\boldsymbol{\nu}} &= \boldsymbol{\tau} - \boldsymbol{D}\boldsymbol{\nu}_r + \boldsymbol{R}(\psi_y)^T\boldsymbol{b} \\ \dot{\boldsymbol{b}} &= -\boldsymbol{T}_b^{-1}\boldsymbol{b} \end{aligned} \tag{61}$$

A2. For $\boldsymbol{D} = \{d_{ij}\} \quad i,j = 1...3$, the elements $d_{11}, d_{22} > 0$

A3. The bias time constants matrix $\boldsymbol{T}_b$ and each 3×3 sub-block of $\boldsymbol{A}_w$ from equation 30 satisfies property 2. (This implies that the north and east direction constants in bias, wave relative damping, and wave motion period are identical).

If assumptions **A1,A2,A3** hold then the total vessel model from equation 30 and 28 can be written as:

$$\dot{\boldsymbol{x}} = \boldsymbol{T}(\psi_y)^T\boldsymbol{A}\boldsymbol{T}(\psi_y)\boldsymbol{x} + \boldsymbol{B}\boldsymbol{\tau} \tag{62}$$

were $\boldsymbol{x} = [\boldsymbol{\xi}, \boldsymbol{\eta}, \boldsymbol{\nu}, \boldsymbol{b}]$.

Property 2 - Commuting Matrices (Lindegaard and Fossen, 2001)

A matrix $\boldsymbol{K}$ is said to commute with the rotation matrix $\boldsymbol{R}_b^n(\boldsymbol{\Theta})$ if

$$\boldsymbol{K}\boldsymbol{R}_b^n(\boldsymbol{\Theta}) = \boldsymbol{R}\boldsymbol{K}_b^n(\boldsymbol{\Theta})$$

This means that a system of the error dynamics, $\dot{\boldsymbol{z}} = \boldsymbol{T}(\boldsymbol{\Theta})^T\boldsymbol{A}(\boldsymbol{\Theta})\boldsymbol{T}(\boldsymbol{\Theta})\boldsymbol{z}$, can be written as $\dot{\boldsymbol{z}} = \boldsymbol{A}\boldsymbol{z}$ were

$$\boldsymbol{A} = \begin{bmatrix} \boldsymbol{K}_{11} & \boldsymbol{K}_{12} \\ \boldsymbol{K}_{21} & \boldsymbol{K}_{22} \\ \boldsymbol{K}_{31} & \boldsymbol{K}_{32} \end{bmatrix} \tag{63}$$

if the matrices $\boldsymbol{K}$ are chosen to commute with $\boldsymbol{R}_b^n(\boldsymbol{\Theta})$. This will occur if the gains of surge and sway are identical. See (Fossen, 2011) page 334 or (Lindegaard and Fossen, 2001).

Property 3 - Frame Transformation (Fossen, 2002)

The LF vessel model written as:

$$\begin{aligned} \dot{\boldsymbol{\eta}} &= \boldsymbol{R}(\boldsymbol{\Theta})\boldsymbol{\nu} \\ \boldsymbol{M}\dot{\boldsymbol{\nu}} &= \boldsymbol{\tau} - \boldsymbol{D}(\boldsymbol{\nu}_r)\boldsymbol{\nu}_r \end{aligned} \tag{64}$$

Can be written completely in NED frame as such:

$$\begin{aligned} \dot{\boldsymbol{\eta}} &= \boldsymbol{\nu}^e \\ \boldsymbol{M}^* \dot{\boldsymbol{\nu}}^e &= \boldsymbol{J}(\boldsymbol{\Theta})^{-T} \boldsymbol{\tau} - \boldsymbol{D}^*(\boldsymbol{\nu}_r) \boldsymbol{\nu}_r^e \end{aligned} \tag{65}$$

were:

$$\begin{aligned} \boldsymbol{\nu}^e &= [\dot{\boldsymbol{x}}, \dot{\boldsymbol{y}}, \dot{\boldsymbol{z}}, \dot{\boldsymbol{\phi}}, \dot{\boldsymbol{\theta}}, \dot{\boldsymbol{\psi}}] \\ \boldsymbol{M}^* &= \boldsymbol{J}(\boldsymbol{\Theta})^{-T} \boldsymbol{M} \boldsymbol{J}(\boldsymbol{\Theta})^{-T} \\ \boldsymbol{D}^*(\boldsymbol{\nu}_r) &= \boldsymbol{J}^{-T} \boldsymbol{D}(\boldsymbol{\nu}_r) \boldsymbol{J}^{-T} \end{aligned} \tag{66}$$

Property 4 - Mean Value Theorem (Refsnes, 2007)

We define a function $d(x) = \boldsymbol{D}(x)x$ for $x \in \mathbb{R}^6$ for simplification, which by employing the mean value theorem:

$\boldsymbol{D}(b)b - \boldsymbol{D}(a)a = \left.\frac{\partial d(e_{b-a})}{\partial e_{b-a}}\right|_{e_{b-a}=e_0} (b-a) \triangleq \delta(e_{b-a})(b-a)$

Property 5 (Lindegaard and Fossen, 2001)

Assuming that the angular rates of the vessel $\boldsymbol{\nu}_2 = [p, q, r]^T$ *are relatively small. Then the stability of the observer error dynamics* $\dot{\boldsymbol{e}} = \boldsymbol{A}(\boldsymbol{\Theta})\boldsymbol{e}$ *is approximately equivalent to the stability of the system* $\dot{\boldsymbol{z}} = \boldsymbol{T}(\boldsymbol{\Theta})^T \boldsymbol{A}(\boldsymbol{\Theta})\boldsymbol{T}(\boldsymbol{\Theta})\boldsymbol{z}$*, were* $\boldsymbol{e} = \boldsymbol{T}(\boldsymbol{\Theta})\boldsymbol{z}$ *, and* $\boldsymbol{T}(\boldsymbol{\Theta}) = diag[\boldsymbol{R}_b^n(\boldsymbol{\Theta}), \boldsymbol{R}_b^n(\boldsymbol{\Theta}), \boldsymbol{I}]$. See (Fossen, 2011) page 334 or (Lindegaard and Fossen, 2001).

Algorithm 1 - Extended Kalman Filter Algorithm (Fossen, 2011)

For the state space system of the form:

$$\begin{aligned} \dot{\boldsymbol{x}} &= \boldsymbol{f}(\boldsymbol{x}) + \boldsymbol{B}\boldsymbol{u} + \boldsymbol{E}\boldsymbol{w} \\ \boldsymbol{y} &= \boldsymbol{H}\boldsymbol{x} + \boldsymbol{v} \end{aligned} \tag{67}$$

can be estimated using the discrete Extended Kalman Filter, see table 6:

Table 6: Discrete-time Extended Kalman Filter (Fossen, 2011)

Design matrices	$\boldsymbol{Q} = \boldsymbol{Q}^T > 0$, $\boldsymbol{R} = \boldsymbol{R}^T > 0$
Initial conditions	$\bar{\boldsymbol{x}}(0) = \boldsymbol{x}_0$, $\bar{\boldsymbol{P}} = \boldsymbol{P}_0$ i.e $\boldsymbol{P}_0 = \boldsymbol{I}$
Kalman gain matrix	$\boldsymbol{K}(k) = \bar{\boldsymbol{P}}(k)\boldsymbol{H}^T(k)[\boldsymbol{H}(k)\bar{\boldsymbol{P}}(k)\boldsymbol{H}^T(k) + \boldsymbol{R}(k)]^{-1}$
State estimate update	$\hat{\boldsymbol{x}}(k) = \bar{\boldsymbol{x}} + \boldsymbol{K}(k)[\boldsymbol{y}(k) - \boldsymbol{H}(k)\bar{\boldsymbol{x}}(k)]$
Error covariance update	$\hat{\boldsymbol{P}}(k) = [\boldsymbol{I} - \boldsymbol{K}(k)\boldsymbol{H}(k)]\bar{\boldsymbol{P}}(k)[\boldsymbol{I} - \boldsymbol{K}(k)\boldsymbol{H}(k)]^T + \boldsymbol{K}(k)\boldsymbol{R}(k)\boldsymbol{K}^T(k)$,
State estimate propagation	$\bar{\boldsymbol{x}}(k+1) = \boldsymbol{F}(\hat{\boldsymbol{x}}(k), \boldsymbol{u}(k))$
Error covariance propagation	$\bar{\boldsymbol{P}}(k+1) = \boldsymbol{\Phi}(k)\hat{\boldsymbol{P}}(k)\boldsymbol{\Phi}(k)^T + \boldsymbol{\Gamma}(k)\boldsymbol{Q}(k)\boldsymbol{\Gamma}^T$

The following quantities have been discretized using forward euler integration, where h is the sampling time of the EKF:

$$\begin{aligned} \boldsymbol{F}(\hat{\boldsymbol{x}}(k), \boldsymbol{u}(k)) &\approx \hat{\boldsymbol{x}}(k) + h[\boldsymbol{f}(\hat{\boldsymbol{x}} + \boldsymbol{B}\boldsymbol{u}(k))] \\ \boldsymbol{\Phi}(k) &\approx \boldsymbol{I} + h \left.\frac{\partial \boldsymbol{f}(\boldsymbol{x}(k), \boldsymbol{u}(k))}{\partial \boldsymbol{x}(k)}\right|_{\boldsymbol{x}(k)=\hat{\boldsymbol{x}}(k)} \\ \boldsymbol{\Gamma}(k) &\approx h\boldsymbol{E} \end{aligned} \tag{68}$$

$\frac{\partial \boldsymbol{f}(\boldsymbol{x}(k),\boldsymbol{u}(k))}{\partial \boldsymbol{x}(k)}\Big|_{\boldsymbol{x}(k)=\hat{\boldsymbol{x}}(k)}$ is treated as the jacobian of $\boldsymbol{f}(\boldsymbol{x})$.

The continuous-time EKF is incremental GES under the assumption that $\boldsymbol{P}$ is uniformly positive definite and upper bounded (Jouffroy and Fossen, 2010).

Appendix B - ROV Data

This section will present data and figures from the ROV tests which were excluded from the main text. Note that most of the figures are stored digitally.

ROV Wave Responce (Long Crested Waves)

Table 7: ROV Wave Responce - LongCrested Waves

ShortCrested Waves	Period	Period	Period
Significant Waveheight 0.5	10	5	2
North Amplitude	0.11	0.7	0.12
East Amplitude	0.03	0.003	0.0005
Depth Amplitude	0.044	0.026	0.004
Significant Waveheight 1.5	10	5	2
North Amplitude	0.32	0.23	0.043
East Amplitude	0.09	0.071	0.001
Depth Amplitude	0.16	0.1	0.02

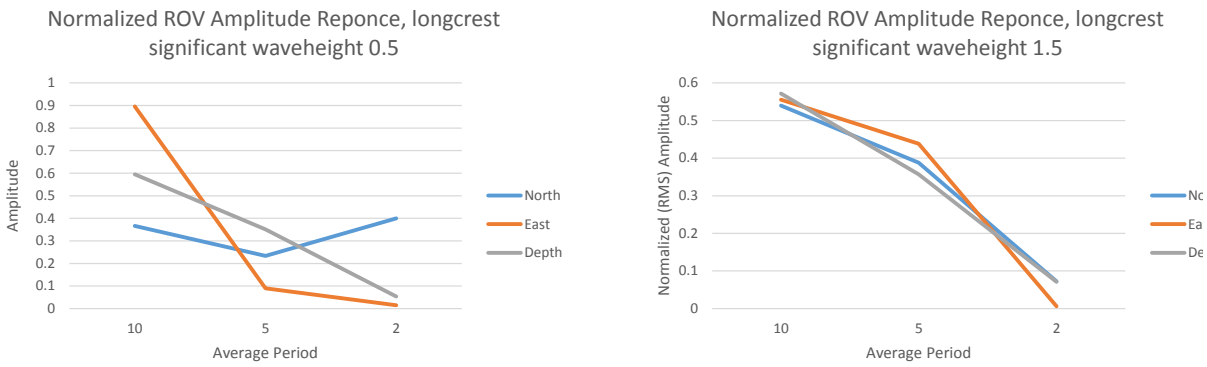

Figure 38: Normalized ROV Amplitude Wave Responce (Long Crested Waves)

ROV Model Coefficients

$$\boldsymbol{M}_{RB} = \begin{bmatrix} 617 & 0 & 0 & 0 & 0 & 0 \\ 0 & 617 & 0 & 0 & 0 & 0 \\ 0 & 0 & 617 & 0 & 0 & 0 \\ 0 & 0 & 0 & 79 & 0 & 0 \\ 0 & 0 & 0 & 0 & 116 & 0 \\ 0 & 0 & 0 & 0 & 0 & 136 \end{bmatrix} \tag{69}$$

$$\boldsymbol{M}_{A} = \begin{bmatrix} 363 & 0 & 0 & 0 & 0 & 0 \\ 0 & 510 & 0 & 0 & 0 & 0 \\ 0 & 0 & 2457 & 0 & 0 & 0 \\ 0 & 0 & 0 & 90 & 0 & 0 \\ 0 & 0 & 0 & 0 & 332 & 0 \\ 0 & 0 & 0 & 0 & 0 & 48 \end{bmatrix} \tag{70}$$

$$\boldsymbol{D}_{L} = \begin{bmatrix} 564 & 0 & 0 & 0 & 0 & 0 \\ 0 & 382 & 0 & 0 & 0 & 0 \\ 0 & 0 & 84 & 0 & 0 & 0 \\ 0 & 0 & 0 & 39 & 0 & 0 \\ 0 & 0 & 0 & 0 & 39 & 0 \\ 0 & 0 & 0 & 0 & 0 & 33 \end{bmatrix} \tag{71}$$

$$\boldsymbol{D}_{NL}(|\boldsymbol{\nu}_r|) = \begin{bmatrix} 705|\boldsymbol{\nu}_r| & 0 & 0 & 0 & 0 & 0 \\ 0 & 764|\boldsymbol{\nu}_r| & 0 & 0 & 0 & 0 \\ 0 & 0 & 830|\boldsymbol{\nu}_r| & 0 & 0 & 0 \\ 0 & 0 & 0 & 203|\boldsymbol{\nu}_r| & 0 & 0 \\ 0 & 0 & 0 & 0 & 193|\boldsymbol{\nu}_r| & 0 \\ 0 & 0 & 0 & 0 & 0 & 131|\boldsymbol{\nu}_r| \end{bmatrix} \tag{72}$$

EKF Process Noise Covariance Gain Matrix

$$\boldsymbol{Q} = diag\begin{bmatrix} 2 & 2 & 2 & 0 & 0 & 0.001 & 10 & 10 & 1 & 0 & 0 & 0.0001 \end{bmatrix} \tag{73}$$

Nonlinear Observer Gains

$$\boldsymbol{K}_{2\eta} = \begin{bmatrix} 0.2 & 0 & 0 & 0 & 0 & 0 \\ 0 & 0.2 & 0 & 0 & 0 & 0 \\ 0 & 0 & 0.5 & 0 & 0 & 0 \\ 0 & 0 & 0 & 0 & 0 & 0 \\ 0 & 0 & 0 & 0 & 0 & 0 \\ 0 & 0 & 0 & 0 & 0 & 0.1 \end{bmatrix}, \boldsymbol{K}_{2\nu} = \mathbf{0}_{6x6} \tag{74}$$

$$\boldsymbol{K}_{3\eta} = \begin{bmatrix} 10 & 0 & 0 & 0 & 0 & 0 \\ 0 & 10 & 0 & 0 & 0 & 0 \\ 0 & 0 & 10 & 0 & 0 & 0 \\ 0 & 0 & 0 & 0 & 0 & 0 \\ 0 & 0 & 0 & 0 & 0 & 0 \\ 0 & 0 & 0 & 0 & 0 & 10 \end{bmatrix}, \boldsymbol{K}_{3\nu} = \mathbf{0}_{6x6} \tag{75}$$

$$\boldsymbol{K}_{4\eta} = \begin{bmatrix} 10 & 0 & 0 & 0 & 0 & 0 \\ 0 & 10 & 0 & 0 & 0 & 0 \\ 0 & 0 & 20 & 0 & 0 & 0 \\ 0 & 0 & 0 & 0 & 0 & 0 \\ 0 & 0 & 0 & 0 & 0 & 0 \\ 0 & 0 & 0 & 0 & 0 & 50 \end{bmatrix}, \boldsymbol{K}_{4\nu} = \begin{bmatrix} 5 & 0 & 0 & 0 & 0 & 0 \\ 0 & 5 & 0 & 0 & 0 & 0 \\ 0 & 0 & 5 & 0 & 0 & 0 \\ 0 & 0 & 0 & 0 & 0 & 0 \\ 0 & 0 & 0 & 0 & 0 & 0 \\ 0 & 0 & 0 & 0 & 0 & 5 \end{bmatrix} \tag{76}$$

Current Observer Gains

$$\boldsymbol{K}_{1p} = \begin{bmatrix} 0.2 & 0 & 0 \\ 0 & 0.2 & 0 \\ 0 & 0 & 0.2 \end{bmatrix}, \boldsymbol{K}_{1\nu} = \begin{bmatrix} 0.01 & 0 & 0 \\ 0 & 0.01 & 0 \\ 0 & 0 & 0.01 \end{bmatrix} \tag{77}$$

$$\boldsymbol{K}_{2p} = \begin{bmatrix} 0 & 0 & 0 \\ 0 & 0 & 0 \\ 0 & 0 & 0 \end{bmatrix}, \boldsymbol{K}_{2\nu} = \begin{bmatrix} 0.05 & 0 & 0 \\ 0 & 0.05 & 0 \\ 0 & 0 & 0.05 \end{bmatrix} \tag{78}$$

$$\boldsymbol{K}_{2p} = \begin{bmatrix} 0.01 & 0 & 0 \\ 0 & 0.01 & 0 \\ 0 & 0 & 0.01 \end{bmatrix}, \boldsymbol{K}_{2\nu} = \begin{bmatrix} 0.01 & 0 & 0 \\ 0 & 0.01 & 0 \\ 0 & 0 & 0.01 \end{bmatrix} \tag{79}$$

Simulation Data

Simulation data is found in the attached CD.